EFFECTS OF MISSION OVERLOADS ON FATIGUE CRACK GROWTH IN Ti-6Al-2Sn-4Zr-2Mo

Thesis

Submitted to

The School of Engineering of the

UNIVERSITY OF DAYTON

In Partial Fulfillment of the Requirements for

The Degree of

Master of Science in Materials Engineering

By

Daniel Maurice Solomon, M.S.

Dayton, Ohio

August 2018

EFFECTS OF MISSION OVERLOADS ON FATIGUE CRACK GROWTH IN Ti-6Al-2Sn-4Zr-2Mo

Name: Solomon, Daniel Maurice

APPROVED BY:

James M. Larsen, Ph.D.
Advisory Committee Chairman
Emeritus Senior Scientist
Wright-Patterson Air Force Base, OH
AFRL/RXCM

Charles E. Browning, Ph.D.
Committee Member
Chairperson, Professor and Torley Chair
in Composite Materials

Andrew H. Rosenberger, Ph.D.
Committee Member
Senior Materials Research Engineer
Wright-Patterson Air Force Base, OH
AFRL/RXCM

Donald A. Klosterman, Ph.D.
Committee Member
Associate Professor
Chemical & Materials Engineering

Robert J. Wilkens, Ph.D., P.E.
Associate Dean for Research and Innovation
Professor
School of Engineering

Eddy M. Rojas, Ph.D., M.A., P.E.
Dean
School of Engineering

ABSTRACT

EFFECTS OF MISSION OVERLOADS ON FATIGUE CRACK GROWTH IN Ti-6Al-2Sn-4Zr-2Mo

Name: Solomon, Daniel Maurice
University of Dayton

Advisor: Dr. James M Larsen

Aircraft turbine engines, especially military engines, experience variable amplitude loading (mission loading) during operation. Predicting the impact of overloads in turbine engines is key in interpreting fatigue damage and assessing the reliable lifetime of components. The objective of this study was to understand the effects of single and repeated overloads during fatigue crack growth in Ti-6Al-2Sn-4Zr-2Mo used in aircraft turbine engine rotor components.

Experiments were conducted using compact tension specimens C(T) in a servo-hydraulic testing machine to measure the fatigue crack growth rates during the application of single overloads under stress intensity factor (ΔK) and load (ΔP) control. Additional experiments were conducted having, variable amplitude loading consisting of a controlled number of constant amplitude baseline cycles between periodic overloads.

Single overload experiments revealed crack growth acceleration and not the classic retardation typically expected. Repeated overloads experiments demonstrated that Miner's rule accurately predicted realistic overload behavior. Overall, the crack growth rates during single overload or repeated overloads resulted in consistent behavior, and significant crack growth retardation was not observed throughout testing in this material. In addition, crack growth rates were similar for overload and underload block fatigue conditions. The understanding of this behavior and the impact on aircraft turbine engine life tracking using Total Accumulated Cycles (TACs) was discussed. It appeared that minor cycles were generally more damaging than currently accounted for in military turbine engine life tracking.

ACKNOWLEDGEMENTS

First and foremost, I would like to thank God Almighty for routinely putting me in blessed situations to succeed. Thank you to my loving parents, Danny and Sheila Solomon, for always being there for me. Also, thank you to my other family members who constantly gave me support. Whether the support was in athletics, academics, or other life choices, I could always count on getting support from my family. Thank you to my teachers and mentors throughout my life. Thank you to Chinedum Ukandu for helping me in ways no one else could. Thank you to Laura Bistrek for keeping me on task and focused throughout the undergraduate years. Thank you to Maceo Cofield for being a rock I could lean on whenever I was faced with any kind of trouble throughout my entire experience at UD. Your hard work and sacrifice allowed me the opportunity to shine brightly in ways I didn't think were possible.

Special thanks to Dr. Charles Browning for the opportunity to be a part of the University of Dayton School Engineering as a graduate student and the Air Force Research Laboratory (AFRL). Special thanks to Dale Osborne and John Porter for the continuous support throughout my time at AFRL. Special thanks to my mentors Dr. James Larsen and Dr. Andrew Rosenberger for the knowledge and support they have given me.

TABLE OF CONTENTS

LIST OF FIGURES

LIST OF TABLES

LIST OF ABBREVIATIONS AND NOTATIONS

a	Crack Length (mm)
a_i	Current Crack Length (mm)
a_{OL}	Crack Length at Overload (mm)
a_P	Crack Length at the end of the Overload Plastic Zone (mm)
BCC	Body Centered Cubic
CBO	Cycles Between Overloads
CIC	Cruise Intermediate Cruise – engine subcycle
C(T)	Compact Tension Specimen
da/dN	Crack Growth Rate (mm/cycle) (m/cycle)
DCA	Damage Curve Approach
DCPD	Direct Current Potential Drop
E	Modulus of Elasticity
FCG	Fatigue Crack Growth
FCGR	Fatigue Crack Growth Rate
FTC	Full Thermal Cycle – engine subcycle
GUI	Graphical User Interface
HCP	Hexagonal Close Packed
Hz	Hertz – unit of frequency
K	Stress Intensity Factor $(\mathrm{MPa}\sqrt{\mathrm{m}})$
K_C	Critical Stress Intensity Factor $(\mathrm{MPa}\sqrt{\mathrm{m}})$
ΔK	Stress Intensity Factor Range = K_{max} - K_{min} $(\mathrm{MPa}\sqrt{\mathrm{m}})$
K_{OL}	Overload Stress Intensity Factor $(\mathrm{MPa}\sqrt{\mathrm{m}})$
K_{MAX}	Max Stress Intensity Factor $(\mathrm{MPa}\sqrt{\mathrm{m}})$
K_{MIN}	Min Stress Intensity Factor $(\mathrm{MPa}\sqrt{\mathrm{m}})$
LCF	Low Cycle Fatigue – engine subcycle
LDR	Linear Damage Rules
N	A Loading Cycle
N1	Rotor Speed for the Low Pressure Spool
N2	Rotor Speed for the High Pressure Spool

OL	Overload
OLR	Overload Ratio
P	Load (N) (KN)
ΔP	Load Range = P_{max} - P_{min}
PICC	Plasticity Induced Crack Closure
PLA	Power Lever Angle
R	Stress Ratio
$r_{P,OL}$	Overload Plastic Zone Size (um)
$r_{P,i}$	Current Plastic Zone Size (um)
SEM	Scanning Electron Microscope
SOL	Single Overload
S-N	Stress versus Number of Cycles
σ_{ys}	Yield Stress (Pa) (MPa)
TAC	Total Accumulated Cycles
TEM	Transmission Electron Microscope
TFR	Terrain Following Radar
UTS	Ultimate Tensile Strength (Pa) (MPa)

CHAPTER I

INTRODUCTION

Problem Description

Initiation and propagation of fatigue cracks in aircraft turbine engine rotor components can lead to catastrophic failure. These components in service are normally subjected to variable amplitude cyclic loading produced by variations in engine speeds. In this regard, an overload may be described as a periodic increase (e.g. takeoff) above the baseline maximum stress cycle on aircraft turbine engine rotor components. Such fatigue sensitive components are traditionally designed to a specific life that allows for a planned service usage interval when these components can be removed and replaced, virtually eliminating the probability of catastrophic failure. In order to improve the design, optimization, and safety of these components, fatigue damage analysis and reliable lifetime prediction are key. Although mission overloads are a regular occurrence in turbine engines it has rarely been investigated.

Objective

The objective of this study was to understand the effects of overloads during fatigue crack growth (FCG) in Ti-6Al-2Sn-4Zr-2Mo (Ti-6242), which is used in aircraft turbine engine rotor components. Experiments were conducted to measure the effects of single overloads and repeated overloads on the fatigue crack growth rates. For repeated overloads, simplified mission block elements were utilized to better understand the suitability of current methods that are used to ensure the durability of titanium turbine engine structures.

CHAPTER II

BACKGROUND AND LITERATURE REVIEW

Important historical observations made during the early 19th century by railway engineers showed that high quality ductile steel could inexplicably break, despite operating at stress levels that were well below the static strength of the steel. These materials would typically exhibit ductile fracture when failed statically and a brittle fracture, when failed under very long term repeated loading of low magnitude [1]. This gave fuel to the theory that cyclic loading could induce metallurgical level damage at ambient temperatures, forcing local brittle failure beginning on crystallographic planes. Wohler subsequently established the concept of the stress vs cycle (S-N) curve that relates fatigue life to the amplitude of cyclic loadings, and his mid-19th century experiments began research into metal fatigue for engineering applications [1]. He established the understanding that fatigue life was affected by both the mean and the amplitude of the stress level of cyclic loading.

More in-depth fatigue damage modeling followed in the 1920s. For example, Palmgren introduced the concept of linear summation of fatigue damage in 1924 [2] [3]. French first reported a significant investigation of the overstress effect on the fatigue endurance limit in 1933 [2] [3], and Langer proposed to separate the fatigue damage process into two stages of crack initiation and crack propagation in 1937 [2] [4]. Kommers suggested using the change in the endurance limit as a damage measure in 1938 [2] [4].

Thus, three early concepts laid the foundation for cumulative fatigue damage models: linear damage summation, change in endurance limit, and the two-stage damage process. In terms of linear damage rules (LDR), the measure of damage was simply described as the cycle ratio (instantaneous cycle count/cycles to failure), with basic assumptions of constant work absorption per cycle, and a characteristic amount of work absorbed at failure. The two-stage linear damage approach improved on the LDR shortcomings, while retaining simplicity in form [2] [3].

It is now understood that over 80% of all service failures of structural components can be traced to mechanical fatigue [5]. Fatigue damage increases with applied cycles in a cumulative manner, which may lead to fracture. Fatigue damage is fundamentally an effect of material structural changes at the microscopic level. Damage theories developed before the 1970s were originally built on the early concepts and attempted to improve the LDR. These damage theories can be categorized into five groups: a damage curve approach (DCA), an endurance limited based approach, an S-N curve modification approach, a two-stage damage approach, and a crack growth based approach [2] [3] [4].

Some notable reasons for fatigue fractures include pure mechanical cycling, rolling contact fatigue caused by movement of contacting surfaces, corrosion and environmentally assisted fatigue in aggressive environments, and creep fatigue at elevated temperatures. The stages of fracture of materials under cyclic stresses or fatigue include initial cyclic damage in the form of cyclic hardening or softening, micro-crack initiation and growth, macro-crack growth and possibly link-up, and finally catastrophic failure. When dealing with prevention of final fracture, two main design philosophies are taken into account. Safe-life design requires replacement of parts once the design lifetime is reached, with no inspection required, regardless of the actual condition of the parts. Fail-safe (damage-tolerant) design requires periodic inspection of cracks that can develop in components, and it establishes that the structure will not fail prior to the time that the cracks are discovered and repaired or the components are replaced [6].

Mission Loading

Figure 1, is a schematic of a flight profile showing the simplified elements of typical flight service missions for a military fighter turbine engine, including takeoff, ferry, training, and terrain following radar (TFR) activity, along with temperature as a function of cycling. The loading spectra, which are produced by variations in engine rotational speed, may contain frequent single or multiple major load excursions along with many less severe cycles [7]. Generally, the major cycles are associated with takeoff and landing, and could be considered overloads in relation to most of the other cycles in a mission. Load interaction effects can produce either crack acceleration or crack retardation depending on the nature of the load sequence. Crack growth retardation tends to occur in fatigue cycles that follow an overload [8] [9] [10].

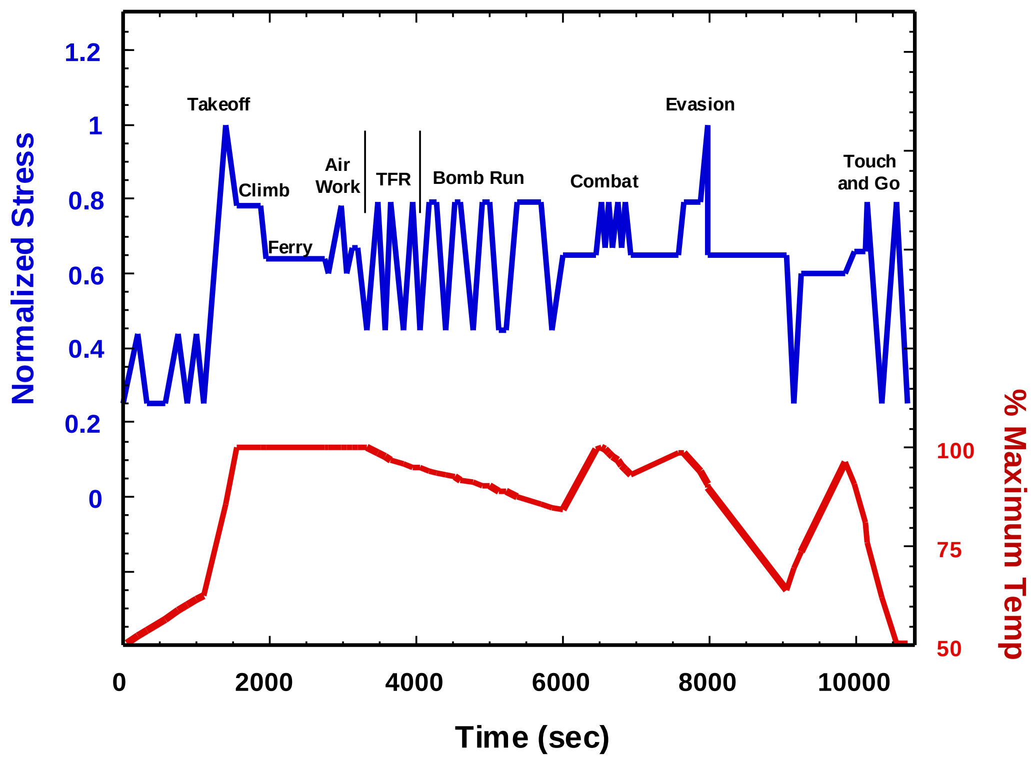

Figure 1: Mission Stress and Temperature Profile [8]

<u>Influence of Mechanisms</u>

Mechanisms of fatigue crack growth under cyclic loads involve the repetitive blunting and re-sharpening of the crack tip, which often results in microscopically visible fatigue striations on the fracture surface. An overload normally results in crack growth retardation during subsequent lower-amplitude fatigue cycles, and may exhibit both intrinsic and extrinsic mechanisms of crack growth retardation. Intrinsic microstructural damage mechanisms operate ahead of the crack tip. Extrinsic, or crack tip shielding mechanisms, act mainly behind the crack tip in retarding crack growth. In metals, extrinsic crack tip shielding mechanisms are primarily a product of the creation of inelastic zones in the crack wake. The result is physical contact between the crack surfaces, which can include sliding, wedging, and bridging or a combination of the three. Extrinsic mechanisms play an important role in the form of crack closure under cyclic loading [5] [11].

Elber [12] introduced the crack closure concept and described the relationship between the effective intensity factor range and the crack growth rate. Several factors can lead to closure, for example, plasticity induced closure, which is due to constraint of surrounding elastic material on the residual stretch in material elements previously strained at the crack tip. Secondly, a crack can be retarded by oxide-induced closure, which is manifested by presence of corrosion debris within the crack wake. Finally, crack surface roughness can induce closure through contact at discrete points between rough fracture surfaces, where significant inelastic local mode II crack tip displacements are present [13] [14]. Long cracks at near-threshold crack growth rates, encompassing several grains, often develop a faceted, microstructural morphology, which is the basis of substantial effects from roughness induced crack closure.

Crack closure is the only mechanism capable of explaining the commonly observed effect of delayed retardation (gradual development of retardation following an overload), and therefore closure is generally considered the primary cause of post-overload retardation [15] [16]. Research has shown that, plasticity induced crack closure can fully account for the delayed retardation of crack growth [17]. Residual crack tip compression results when an overload induces high plastic strains in the area ahead of the crack tip, which leads to retardation due to the compressive residual stress. Crack closure effects in small cracks are usually less pronounced than for long cracks, due to small cracks having limited crack wake. Residual stress effects at the crack tip are immediate, unlike closure, which operates in the wake of the crack, and induce delayed retardation [12]. Compressive residual stresses are generated in a small region ahead of the crack tip after a single overload. The operative mechanism of the residual stress in isolation is complicated by the possible simultaneous action of crack closure; it has also suggested that crack closure is, partly, a consequence of residual stresses [12] [16].

Models and Methods

Models have been developed to account for the effects of retardation. Retardation models can be classified into two main categories, crack tip plasticity models, and crack closure models. Crack tip plasticity models are based on the assumption that crack growth retardation occurs due to the large plastic zone developed during overloading. Crack closure models are based on Elber's experimental observation that a partial closure of the crack faces occurs during part of a fatigue load cycle. This is a result of the tensile plastic deformation left in the wake of a fatigue crack [15].

Before discussing models that reference overload effects, the following models that represent crack growth rate will be summarized. First, the Paris Power law [11] showed that the fatigue crack growth rate (da/dN) correlates with the cyclic stress intensity factor range ΔK.

$$\frac{da}{dN} = C(\Delta K)^n \tag{2.1}$$

ΔK defined as $\Delta K = K_{MAX} - K_{MIN}$, where K_{MAX} and K_{MIN} are the maximum and minimum values of K, stress intensity factor, in a cycle, and C and n are empirical parameters determined from a power-law curve fit to an experimental data.

Second, the Walker model [19] extended the Paris equation to include effects of mean-stress using a load ratio, R ($R = P_{MIN}/P_{MAX}$).

$$\frac{da}{dN} = C\left[\frac{\Delta K}{(1-R)^{1-m}}\right]^n \tag{2.2}$$

C, n and m are empirical parameters determined from a curve fit to a set of fatigue crack experimental data obtained at multiple load ratios.

Third, the Forman equation [20] focused on the Region III behavior, as depicted below, and predicts the sharp upturn in the da/dN vs ΔK curve as fracture toughness is approached. The equation includes the stress ratio effect and can represent Region II's stable intermediate growth.

$$\frac{da}{dN} = \frac{[C(\Delta K)^n]}{[(1-R)K_c - \Delta K]} \tag{2.3}$$

K_c = critical stress intensity factor

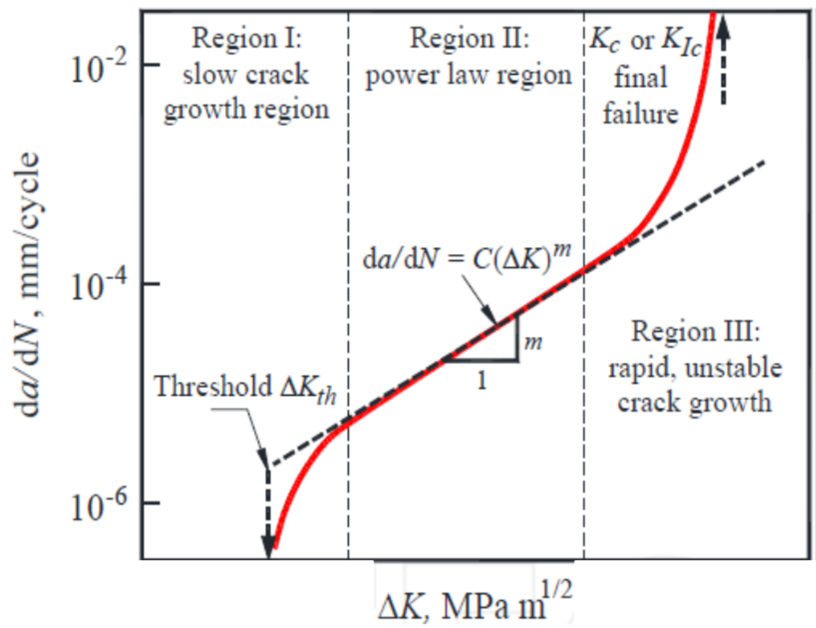

Figure 2: Three Regions of the Fatigue Crack Growth Rate Curve [21]

Fourth, the NASGRO equation [22] developed by Forman and Newman, modified the power law by including the effects of plasticity-induced crack closure. This equation takes into account all three regions of the FCG curve, while also including mean stress and crack closure effects. The NASGRO equation describes crack growth behaviors in the near threshold and critical FCG regimes better than any of the previous equations. It is probably the most accurate crack propagation equation currently available, but it also includes the most fitting parameters.

$$\frac{da}{dN} = \left[C\left(\Delta K_{eff}\right)^n\right]\left[\frac{\left(1-\frac{\Delta K_{th}}{\Delta K}\right)^p}{\left(1-\frac{\Delta K_{max}}{\Delta K_c}\right)^q}\right] \tag{2.4}$$

$$\Delta K_{eff} = U(\Delta K_{th}), \qquad U = \frac{1-f}{1-R}$$

C, n, p, and q are material constants

R = stress ratio

f = Newman's crack opening function

f = $\{\max(R, A_0 + A_1R + A_2R^2 + A_3R^3)\} \qquad R \geq 0$

= $\{A_0 + A_1R\} \qquad -2 \leq R < 0$

$$A_0 = (0.825 - 0.34 \propto +0.05 \propto^2)\left[\cos\left(\frac{\left(\frac{\pi}{2}\right)\sigma_{max}}{\sigma_0}\right)\right]^{\frac{1}{\alpha}}$$

$$A_1 = (0.415 - 0.071 \propto)\left[\frac{\sigma_{max}}{\sigma_0}\right]$$

$$A_2 = 1 - A_0 - A_1 - A_3$$

$$A_3 = 2A_0 + A_1 - 1$$

σ_{max}/σ_0 and α are the fitting parameters

ΔK_{th} = the threshold SIF range

K_c = the critical stress intensity factor

Models referencing overload effects are important in explaining the data observed throughout variable-amplitude fatigue testing. For example, Miner's rule, introduced in the early

20th century [23], suggested that the remaining life under a given variable-amplitude load history undergoes a continuous cycle-by-cycle fractional decrement. Miner's rule, which is a linear cumulative damage model, is given by the equation below.

$$\sum_{i=1}^{k} \frac{n_i}{N_i} = C \tag{2.5}$$

N_i = the average number of cycles to failure at the stress S_i or ith stress

n_i = the number of cycles accumulated at S_i

C = the fraction of life consumed by exposure to the cycles at the different stress levels

However, the Miner's rule damage accumulation equation does not address effects of load sequences, describe interaction between various loads, or include effects of the damage introduced by stresses below the fatigue limit.

Wheeler [15] introduced a model that uses a transient retardation factor as a power function of the ratio of remaining crack extension in the overload plastic zone. This model uses empirically selected constants to approximate experimental observations. Here the crack growth rate is modified by a reduction coefficient Cp.

$$\left(\frac{da}{dN}\right) ret = (Cp)_i[C(\Delta K)^n] \tag{2.6}$$

$$Cp = \left[\frac{rpi}{aol + rpo - ai}\right]^p$$

p = empirically determined shaping parameter

a_{OL} = crack length at overload

r_{PO} = overload plastic zone size

r_{Pi} = current cyclic plastic zone

a_i = current crack length

The Willenborg model [24] assumes that crack growth retardation is caused by compressive residual stresses around the crack tip. A reduced “effective” stress ratio occurs through increased compressive residual stress that leads to retardation.

$$Reff = Keff_{min,i}/Keff_{max,i}$$

$$Keff_{min,i} = K_{min,i} - K_{red}$$

$$Keff_{max,i} = K_{max}, i - K_{red}$$

K_{red} = the modified stress intensity factor, which characterizes the retardation phenomenon

$$K_{red} = (K_{max},)_{OL} * \left(\left(1 - \frac{\Delta a}{Z_{OL}}\right)^{0.5}\right) - K_{max} \tag{2.7}$$

$$Z_{OL} = \alpha \left[\frac{(K_{\max,})OL}{\sigma_{ys}}\right]^2$$

$(K_{MAX})_{OL}$ = the stress intensity factor of the overload cycles

Δa = the amount crack growth length since the overload cycles

Z_{OL} = the plastic zone size created by overload

α = the plastic zone size factor

CHAPTER III

MICROSTRUCTURAL CHARACTERIZATION

Material

Advanced structural titanium alloys, like Ti-6Al-2Sn-4Zr-2Mo (pictured in Fig. 3), are designed for strength at moderate temperatures, yet during service the structural integrity is frequently limited by cyclic loading. Ignoring possible microstructure-texture effects, the strength of titanium alloys is derived from solid solution strengthening and boundary strengthening and therefore depends primarily on alloy composition [25]. Ti-6242 has a nominal chemical composition in weight percent (wt%) that is: 6.20 Al, 1.95 Sn, 3.80 Zr, 2 Mo, 0.08 Si, 0.021 C, 0.008N, 0.06 O, 0.0016H, and balance the Ti. The titanium alloy tested in this project had a bimodal microstructure consisting of alpha (α) and beta (β) phases with crystal structures of hexagonal close packed (HCP), and body centered cubic (BCC), respectively. The β phase has a lower strength and higher ductility in comparison to the α phase, meaning the α phase is the strengthening phase in Ti-6242 [25]. This is due to the larger number of slip planes in the BCC structure of the β phase in comparison to the HCP structure of the α phase.

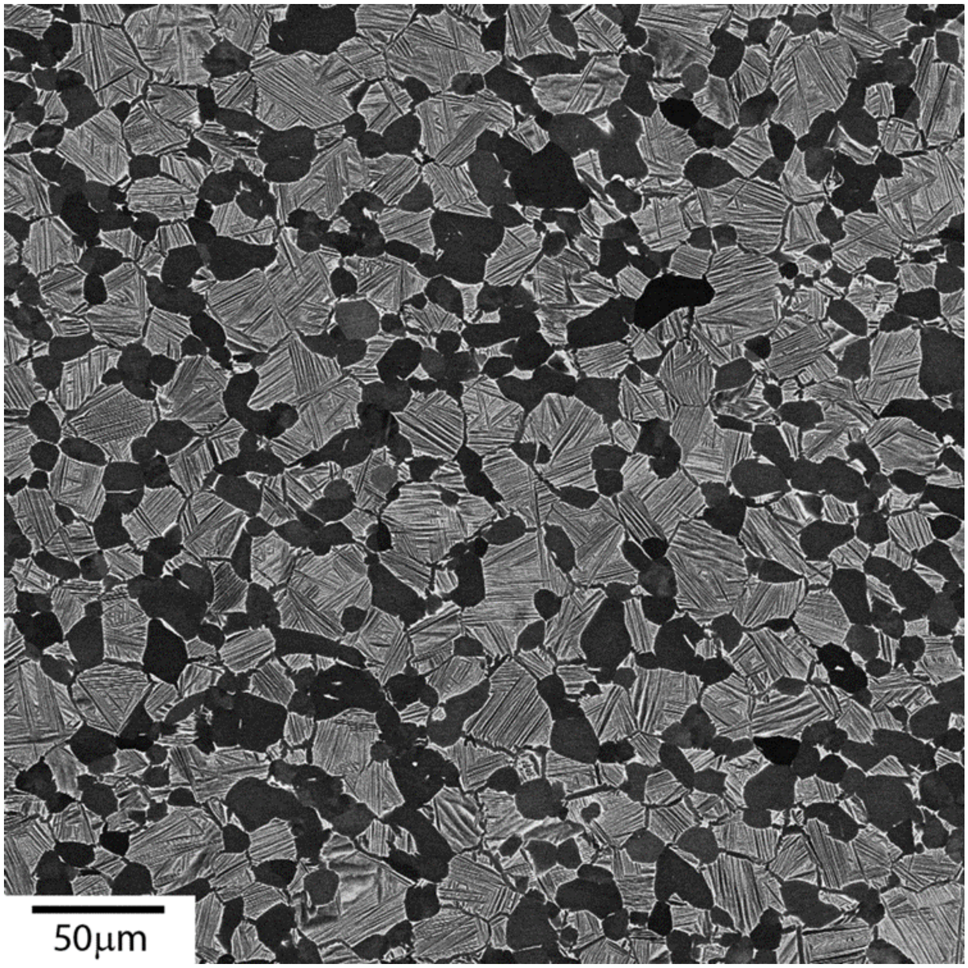

Figure 3: Material Used In This Study

Grain Size Measurement

The quantitative microstructural process used to characterize the primary alpha grain size distributions involved a semi-automated analysis of the 2D representations of Ti-6242 microstructure. First, an image was captured on an SEM, using the back scattered electron detector. Second, Photoshop was used to adjust the image to color for overall clarity. Third, the image was then analyzed in MATLAB, and a Region Growing Graphic User Interface (GUI) was used, to fill the remaining Alpha grains. Fourth, threshold Photoshop image, invert MATLAB image color, then add the two together. Fifth, create three new images in Photoshop with three random straight lines in each that are the same size as the Alpha grain image. Sixth, run general math in

Photoshop's Fovea Pro for each of the three lined images with the Alpha grain image. Finally, calibrate magnification then use measure all features to determine the length of each line, thus providing 2D grain size data, as seen in Table 1 [26].

Some extremely large grains were measured due to errors in the segmentation process. In order to resolve this, the largest grains were individually reviewed to determine if the segmentation was accurate. If any errors occurred, the connecting ligament was erased so that the grains were accurately measured. The smallest measurements were also censored so that measurements were only included if they were at least five pixels long for the lowest magnification. This equates to a length of 2.3 um as the minimum size cutoff for α grains [26].

Table 1: Grain Size Measurements [26]

Primary Alpha Grain Sizes Measurements (um)*	
Average:	12.26
Median:	10.49
Standard Dev:	7.40
Maximum:	73.67
Minimum:	2.31
V_f:	30%

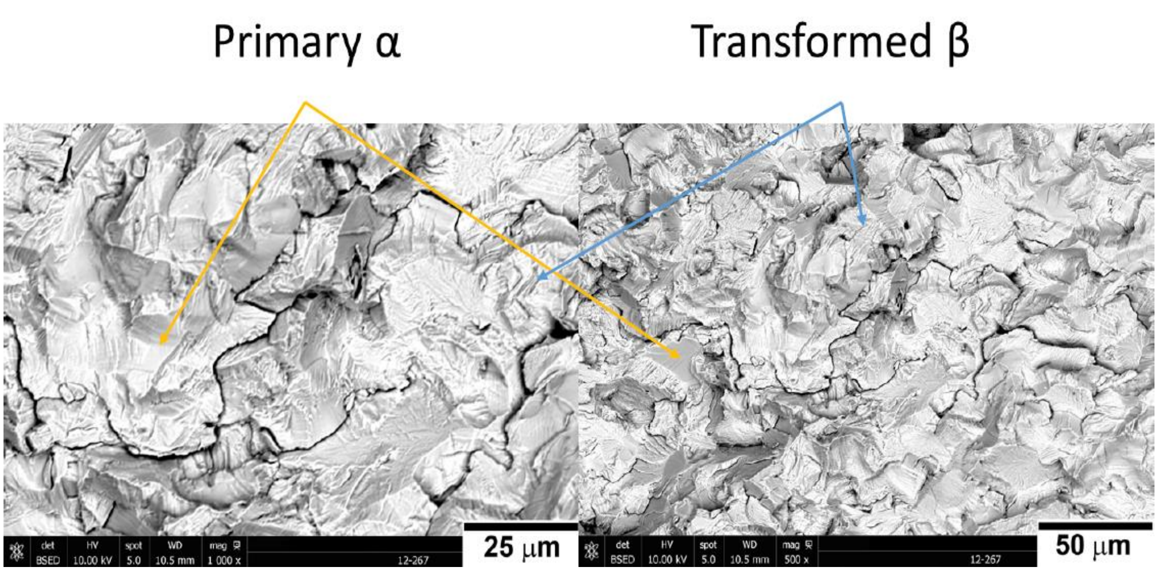

Figure 4: Primary Alpha and Transformed Beta Grains [Shown on a Fatigue Fracture Surface]

The figure above, Figure 4, showcases primary α and transformed (change in phase) β grains in specimen 12-267 on the fracture surface for two SEM backscatter images. The left side image has a micron bar of 25um and the right side image is at a micron bar of 50um. The test conditions that were used to create this fracture surface will be explained in the Experimental Design section.

CHAPTER IV

EXPERIMENTAL DESIGN

The nominal dimensions and image of the Compact Tension Specimen C(T) are shown in Figure 5. The preparation for the test began by making precise measurements of the C(T) specimen that were used in calculation of the stress intensity factor (K) according to the equation below.

$$K = \left(\frac{P}{\sqrt{(BW)}}\right) f\left(\frac{a}{w}\right) \tag{2.8}$$

$$\boldsymbol{f} = \left[\frac{2+\frac{a}{W}}{1-\frac{a^{\frac{3}{2}}}{W}}\right]\left(0.866 + 4.64\left(\frac{a}{W}\right) - 13.32\left(\frac{a}{W}\right)^2 + 14.72\left(\frac{a}{W}\right)^3 - 5.6\left(\frac{a}{W}\right)^4\right)$$

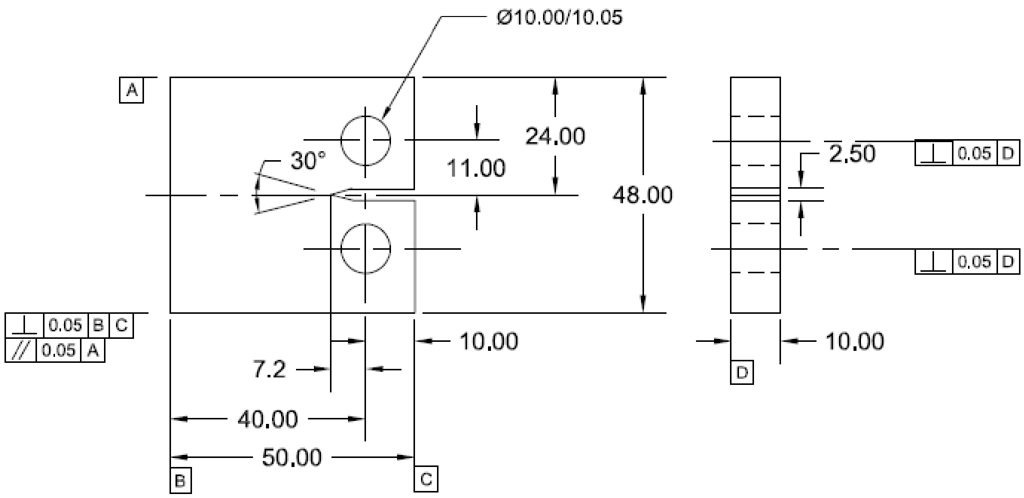

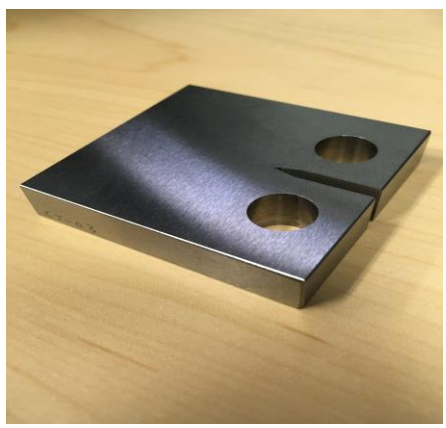

Figure 5: Compact Tension Specimen C(T) Dimensions

The specimen was then marked in specific locations to measure the crack length during the test using direct current potential drop (DCPD). Wiring installation was established at the marked locations via welds of both the current and DCPD voltage wires. These wires were thicker for current leads and thinner for voltage measurements and made of commercial purity titanium, which facilitated high-quality welds to the Ti-6242 specimen. The specimen was then mounted into the load-train clevises of the servo-hydraulic test machine and held at 2% of the selected load-range card in order to hold the specimen rigidly. The DCPD voltage pickup, DCPD voltage reference, and current wires were attached to the proper terminals. For the 10 mm thick, 40 mm wide C(T) specimen, the current supply was set to a constant current equal to 8 amps. The DCPD technique had a constant current being passed through the specimen, resulting in a two-dimensional electrical field, which is constant through the thickness at all points [27]. DCPD was used to detect the initiation of cracks and monitor their growth. The potential drop was measured using voltage probes on either side of the crack [28].

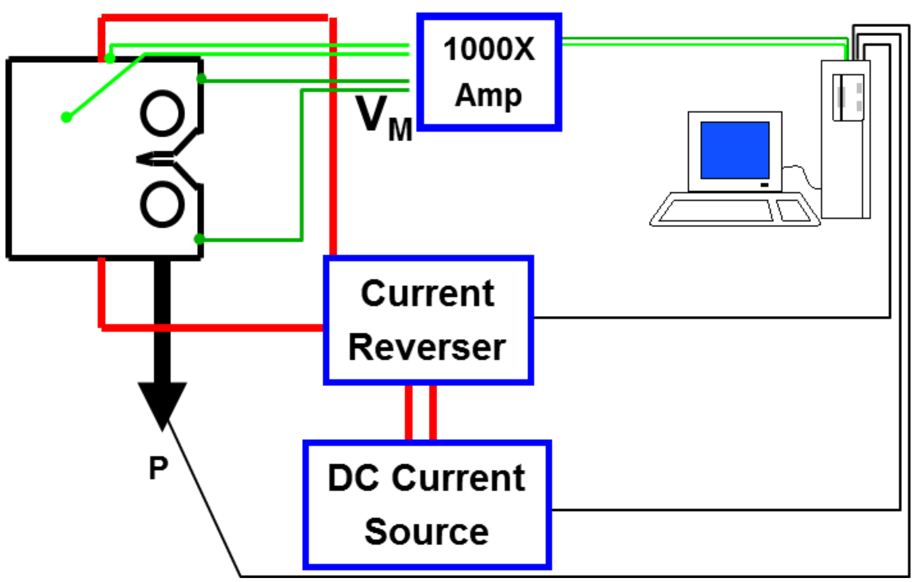

Figure 6: Connections [C(T) to Computer]

Pre-cracking was used to prepare the specimen for subsequent fatigue testing with programmed mission fatigue blocks. The pre-cracking provided a sharpened fatigue crack of adequate size and straightness and established an ideal load history for subsequent testing.

When the test began, the computer program WinMATE [29] ran a test matrix with the variables described below, in general accordance with ASTM specification E647 [27].

Throughout each test there were specific fatigue machine control settings used to control the variable and constant amplitude loading. The variables to be controlled or recorded included the crack length for each minor section of test, or the mission Block, and the major section of the test at a specific ΔK levels or the Batch of mission Blocks. The fatigue machine control software also controlled the frequency (Hz) of the cycles, the stress ratio (R), the overload ratio (OLR), and the number of cycles between overloads (CBO). A portion of a test matrix can be seen in Table 2.

Table 2: Test Matrix [Kmax 6 to 10]

Temperature (°C)	Kmax (Normal Cycle) (MPa√m)	Kmin (Normal Cycle) (MPa√m)	Frequency (Hz)	Load Ratio - R	ΔK (MPa√m)	Overload Ratio - OLR	Kmax (Overload Cycle) (MPa√m)	Normal Cycles Between Overloads - CBO	Batch
22.5	6	*3*	5	0.500	3.00	1.000	6		1
22.5	6	*3*	5	0.500	3.00	1.250	7.5	5	1
22.5	6	*3*	5	0.500	3.00	1.250	7.5	20	1
22.5	6	*3*	5	0.500	3.00	1.250	7.5	40	1
22.5	6	*3*	5	0.500	3.00	1.000	6		2
22.5	6	*3*	5	0.500	3.00	1.500	9	5	2
22.5	6	*3*	5	0.500	3.00	1.500	9	20	2
22.5	6	*3*	5	0.500	3.00	1.500	9	40	2
22.5	8	*4*	5	0.500	4.00	1.000	8		3
22.5	8	*4*	5	0.500	4.00	1.250	10	5	3
22.5	8	*4*	5	0.500	4.00	1.250	10	20	3
22.5	8	*4*	5	0.500	4.00	1.250	10	40	3
22.5	8	*4*	5	0.500	4.00	1.000	8		4
22.5	8	*4*	5	0.500	4.00	1.500	12	5	4
22.5	8	*4*	5	0.500	4.00	1.500	12	20	4
22.5	8	*4*	5	0.500	4.00	1.500	12	40	4
22.5	10	*5*	5	0.500	5.00	1.000	10		5
22.5	10	*5*	5	0.500	5.00	1.250	12.5	5	5
22.5	10	*5*	5	0.500	5.00	1.250	12.5	20	5
22.5	10	*5*	5	0.500	5.00	1.250	12.5	40	5
22.5	10	*5*	5	0.500	5.00	1.000	10		6
22.5	10	*5*	5	0.500	5.00	1.500	15	5	6
22.5	10	*5*	5	0.500	5.00	1.500	15	20	6
22.5	10	*5*	5	0.500	5.00	1.500	15	40	6

Each test was performed a frequency of 5 Hz and a number of batches of constant amplitude baseline fatigue were performed at ΔK levels of 3, 4, 5, 6, and 7.5 $MPa\sqrt{m}$, with an equivalent K max of 6, 8, 10, 12, and 15 $MPa\sqrt{m}$, at a stress ratio of 0.5. Since it is commonly believed that the fatigue crack growth behavior of titanium alloys is not significantly influenced by loading frequency at ambient conditions, the loading frequency of 5 Hz enabled more rapid characterization of the materiel behavior and yet good control of the fatigue parameters. Throughout testing, the baseline stress ratio remained at 0.5, so crack closure was assumed negligible. The batches of fatigue spectrum block subsections that included a baseline block without overloads, blocks with a single overload (SOL), for example Figure 7, and blocks with various cycles between overload (CBO), for example Figure 8. CBO blocks included 5, 10, 20, 40 and 80 cycles, although not all CBO's were used on each C(T) specimen test. Overload ratios (OLR) of 1.25 and 1.50 were used throughout the tests at each different ΔK level, see Table 3.

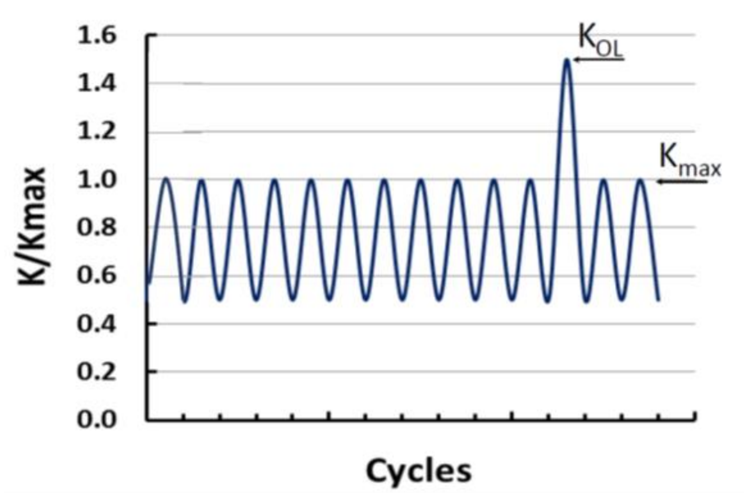

Figure 7: Waveform [Single Overload]

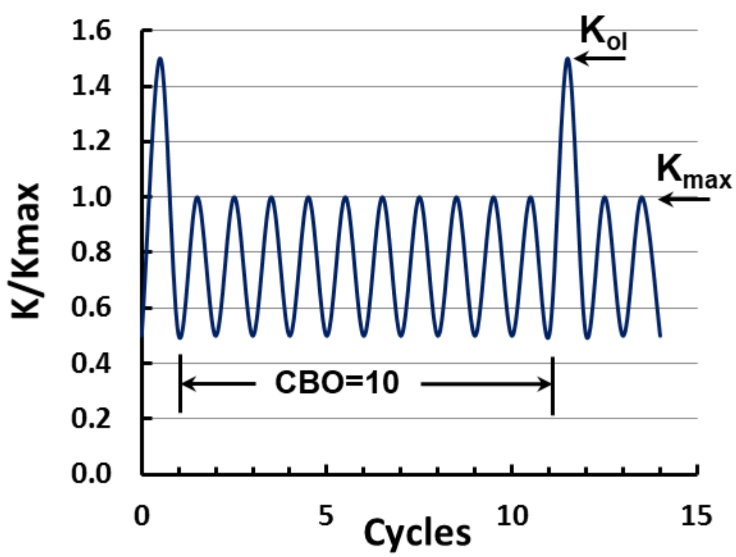

Figure 8: Waveform [10 CBO]

Table 3: Testing K Levels

Testing K Levels					
K_{Min} (MPa$\sqrt{m}$)	3	4	5	6	7.5
K_{Max} (MPa$\sqrt{m}$)	6	8	10	12	15
1.25 K_{OL} (MPa$\sqrt{m}$)	7.5	10	12.5	15	18.75
1.50 K_{OL} (MPa$\sqrt{m}$)	9	12	15	18	22.5

Throughout testing, crack length was periodically measured using a low-power traveling microscope. Crack size was monitored by direct current potential drop (DCPD). Once the test concluded, the specimen was broken open, uninstalled from clevises, and the welded wires were removed. The C(T) specimen was then heat tinted at 420 °C, for approximately 4 hours and then air cooled for two hours, based on prior experience. As a result, the original silver colored fracture surface of the C(T) specimen was transformed into a varying gold surface depending upon the surface state, (Figure 13). This allowed for a much clearer view of crack-front features throughout various stages of the test.

CHAPTER V

RESULTS

Tension tests were performed, in general accordance with test method ASTM E8 [30], in order to measure the yield stress (σ_{ys}), the ultimate tensile stress (UTS), and the modulus of elasticity (E) for use in the load interaction crack growth models. Figure 9 illustrates the complete stress vs strain curve, while Figure 10 focuses on the modulus region of the test. The modulus was 118.8 GPa, the yield strength was 920 MPa, and the ultimate tensile strength was 1024 MPa.

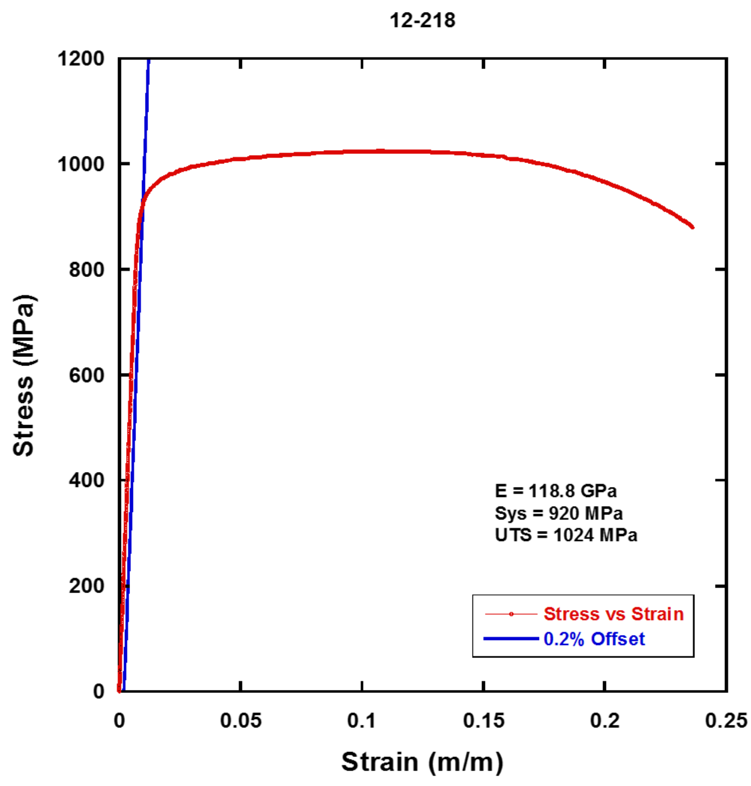

Figure 9: Tension Test

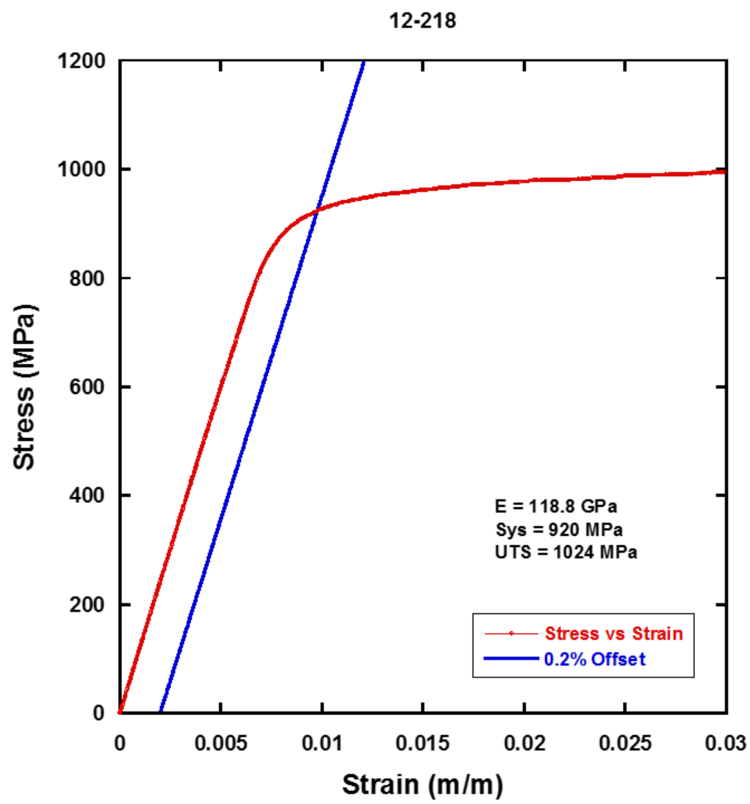

Figure 10: Tension Test Modulus Region

As a basis for understanding effects of repeated overloads at varying CBOs, single overload (SOL) tests were performed. These tests were conducted at a K_{MAX} of 10 and 15, and at OLRs of 1.25 and 1.50, using both constant ΔP and constant ΔK controls, (see Table 4). With constant ΔK controlled test, there was a possibility of load shedding artificially retarding the crack growth rates. With the constant ΔP controlled tests, the load range was held constant, removing any effect of load shedding. Figure 11, shows a typical result of a SOL test from literature in terms of crack length (a) and number of cycles (N). Results of the SOLs performed under the current project will be reviewed in the discussion section.

Table 4: Single Overload Tests

Single Overloads			
OLR	$K_{max,OL}$	K_{max}	Control
1.25	12.5	10	K
1.5	15	10	P
1.5	15	10	K
1.25	18.75	15	P
1.25	18.75	15	K
1.5	22.5	15	P
1.5	22.5	15	K

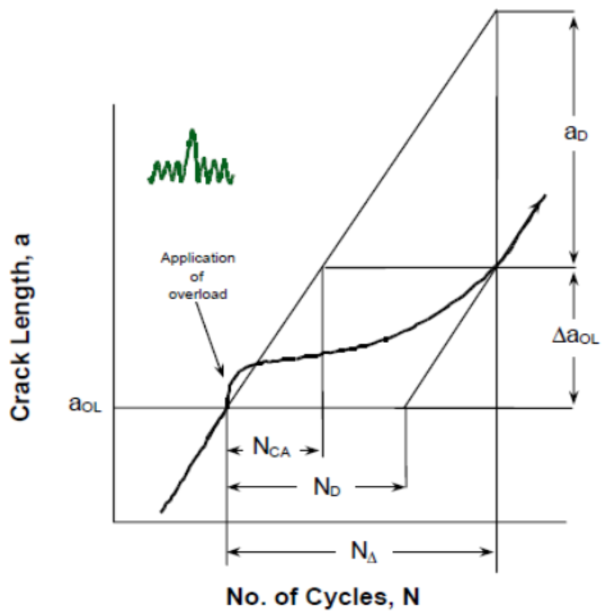

Figure 11: Single Overload Example [10]

To begin analysis of the data collected throughout testing, the fracture surface of each C(T) specimen was first observed under an optical microscope to measure the true length of the crack at the periodic mission intervals and to correct for any curvature of the crack front. An example is shown in Figure 13. These measurements were used to correct the DCPD measured crack length and subsequent K calculations.

The Figure 12 shows an optical microscope image of the fracture surface of specimen 12-267. This image highlights the changes in the fracture surface color and associated reflectivity as revealed by heat tinting. The lighter versus darker sections indicate notable changes in the test.

These sections indicate where certain batches started and ended. Included in the figure are SEM secondary images that show details of batches 1 and 5.

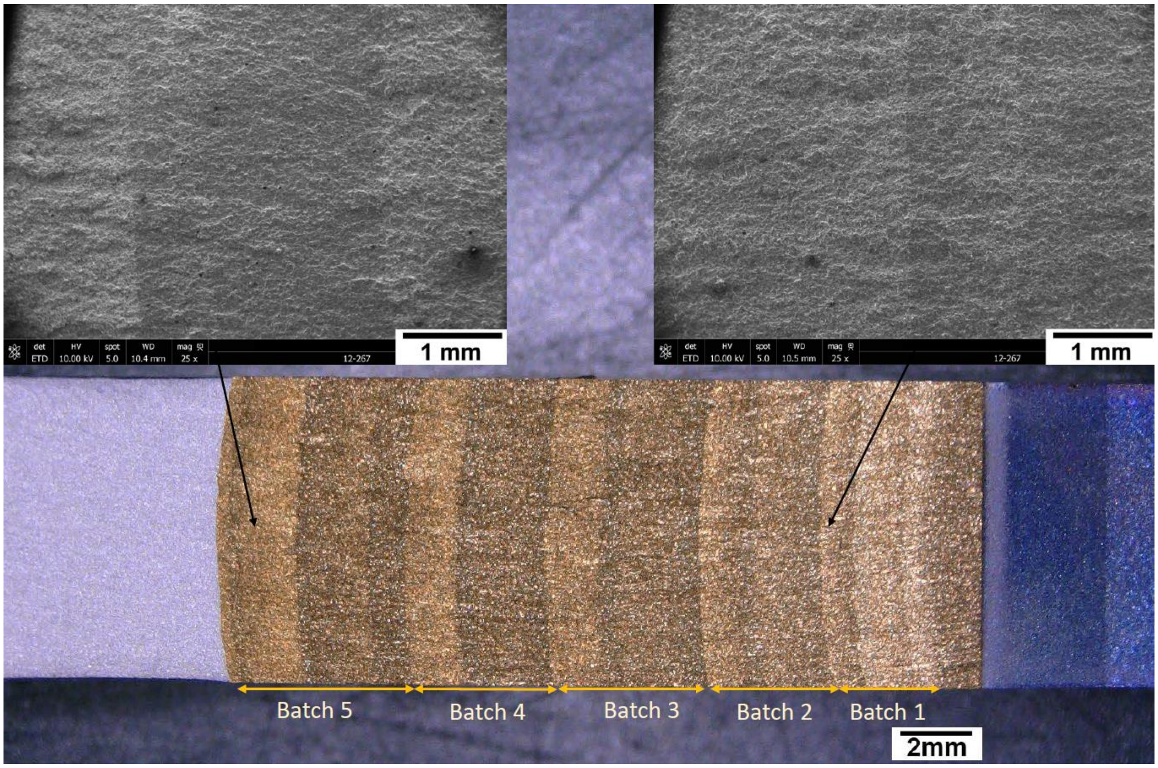

Figure 12: 12-267 Fracture Surface Map

Details of the crack front measurements are shown in Figure 13.

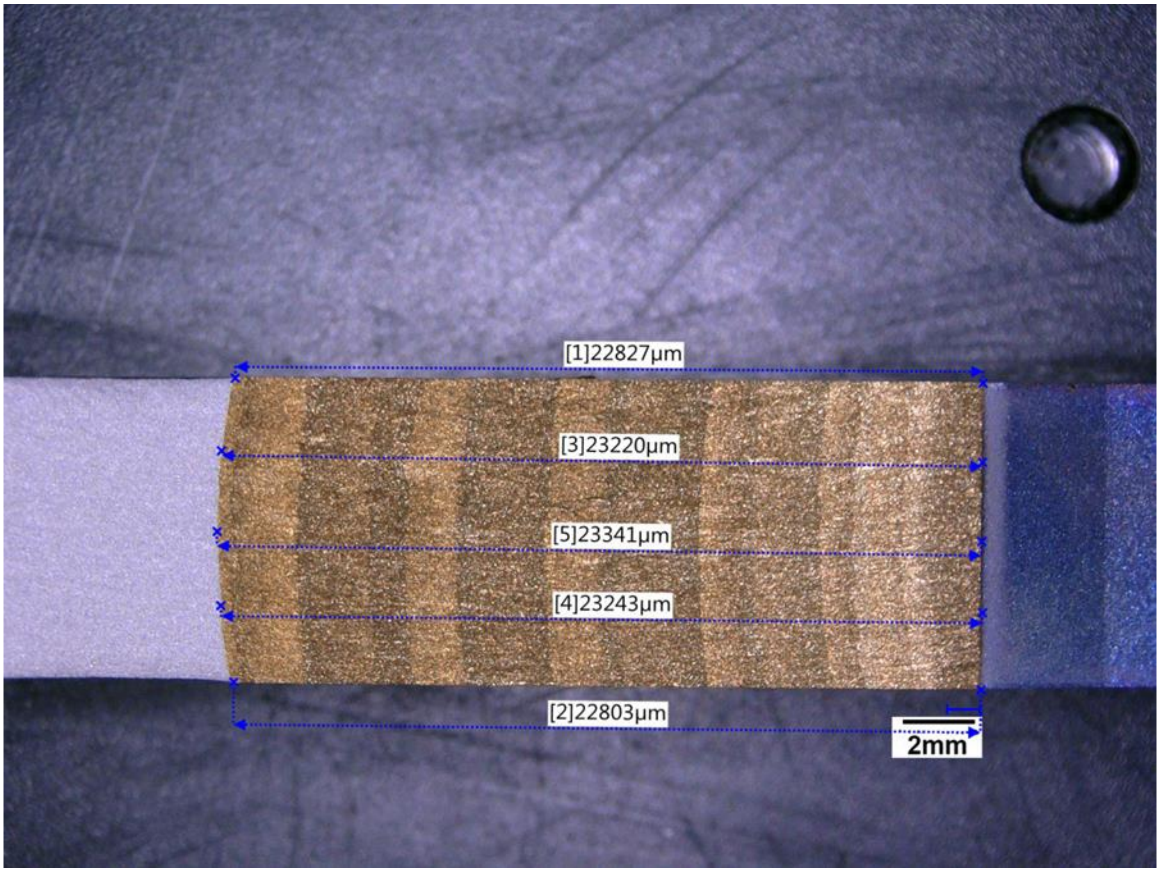

Figure 13: Details of Fractographic Crack Length Measurement

Five crack length points were measured on the fracture surface to locate precisely the crack lengths; an example is shown in Figure 13. Once the recorded crack lengths were corrected, the crack growth rate and applied ΔK were determined for each block of the experiment. The fatigue crack growth rates were taken at the baseline levels throughout each batch for each specimen. The da/dN vs ΔK baseline values were fitted via a power law trend line and these fits were then used to obtain the material constants C and n, of the Paris Law, Figure 14. It is important to stress that each point on Figure 14 represents an average crack growth rate that was determined for a block of crack growth. Typically, during a block, the crack was extended 0.3 to 0.4 mm and the average crack growth rate and applied ΔK were plotted as a single point on the fatigue crack growth vs ΔK figure.

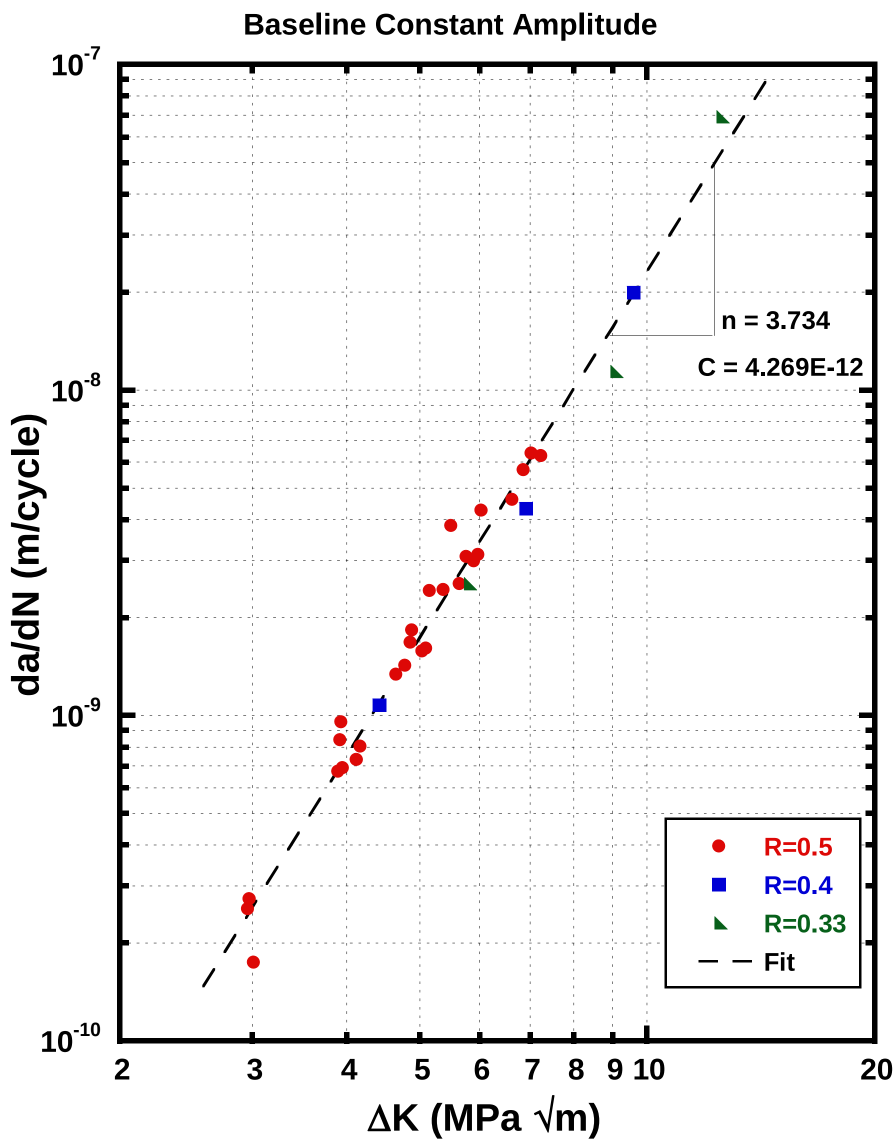

Figure 14: Baseline Constant Amplitude Fatigue Crack Growth Rates [da/dN vs ΔK]

The material constants are then used as a foundation block to creating further plots to reduce effects of experimental measurement scatter. The baseline fatigue crack growth rate at R = 0.5 is shown in the circle symbols. During the testing, blocks were inserted containing constant amplitude cycling at the overload conditions that resulted in lower stress ratios. The overload ratio of 1.25 resulted in an R for the baseline cycles of 0.4 (square symbols) and the overload ratio of 1.50 resulted in a baseline cycle R of 0.333 (triangle symbol). As shown, over the range of stress ratio from 0.33 to 0.5 the baseline crack growth behavior essentially equivalent, and all of the constant amplitude cycling data were used to compute baseline Paris law constants.

In a similar manner, the fatigue crack growth rates versus ΔK were plotted for CBO = 5, 10, 20, 40, and 80 for OLR = 1.25 and 1.50 for each block of loading at the various K levels. These fatigue crack growth rate data were fitted via a power-law trend line, as exemplified in Figure 15 for 5 CBO at OLR = 1.25. The remainder of the fits can be found in APPENDIX B.

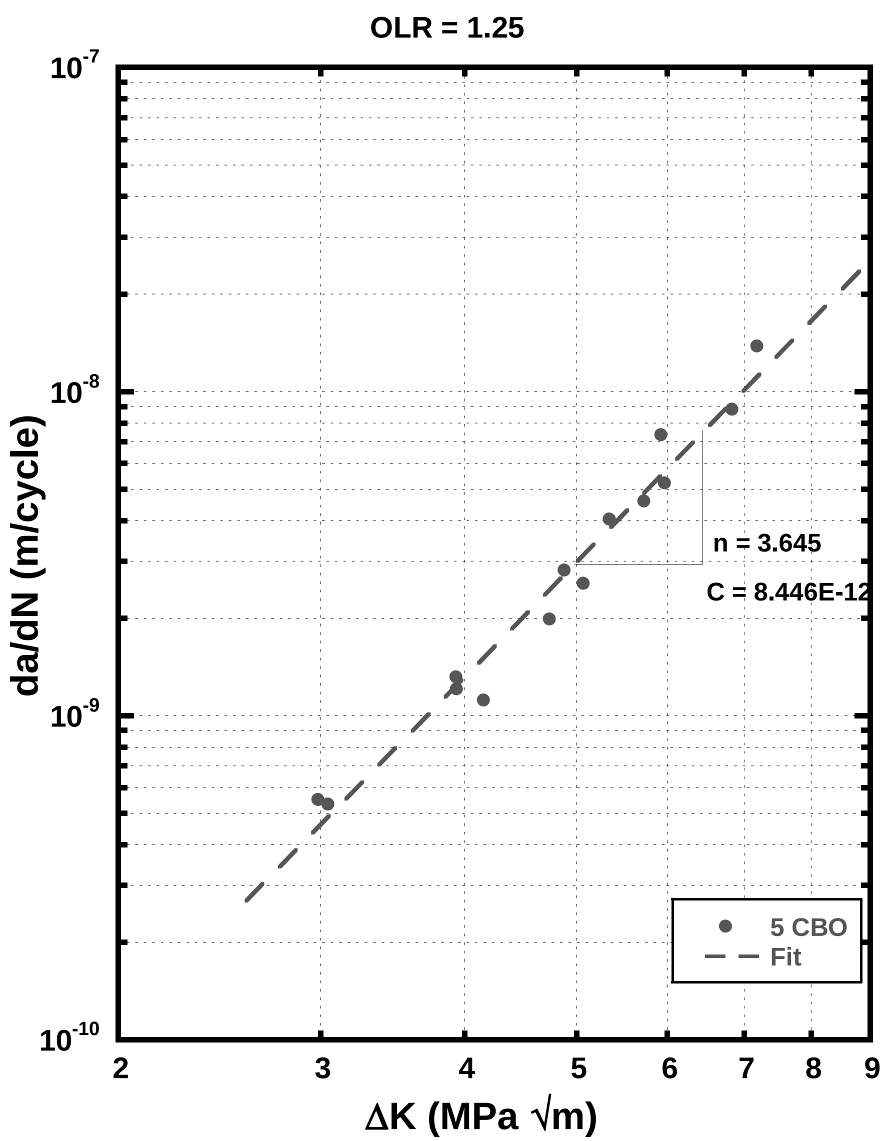

Figure 15: Paris Power Law Fit 5 CBO OLR = 1.25 [da/dN vs ΔK]

These fits were then used to obtain the material constants C (m/cycle) and n (unit-less), in the Paris Power Law. Table 5 shows the fits for all of the test conditions in this study.

Table 5: Paris Power Law Master Fits Material Constants

Paris Power Law Master Fits Material Constants						
OLR = 1.25	Baseline	5 CBO	10 CBO	20 CBO	40 CBO	80 CBO
C	4.268E-12	8.445E-12	6.725E-12	7.653E-12	6.022E-12	9.486E-12
n	3.734	3.645	3.690	3.497	3.544	3.229
OLR = 1.5	Baseline	5 CBO	10 CBO	20 CBO	40 CBO	80 CBO
C	4.268E-12	3.906E-12	3.778E-12	2.595E-12	3.028E-12	5.737E-12
n	3.734	4.642	4.538	4.520	4.228	3.609

The C and n Paris power law constants in Table 5 were used to compare the crack growth behavior of the material at the range of test conditions. The crack growth rates, da/dN versus, ΔK, for OLR = 1.25 and the various CBOs are shown in Figure 16. Also shown in the figure is a dashed line that plots the crack growth rate of the overload cycling as if it was referenced to the baseline ΔK. That is, this line represents the equivalent crack growth rate that would be seen if CBO = 0, and all cycling was at the overload condition. Generally, as the CBO increased, the crack growth rate decreased. This can be seen in the consistent reduction in growth rate for CBO = 5, 10, 20 and 40. The CBO = 80 trend started out out faster than CBO = 40 at low ΔK and was slower than CBO = 40 and the baseline trend at high ΔK. This lower slope is apparent in the coefficients in Table 5 but it is not clear why this is happening. As the number of cycles between overload increases, the growth rate must approach the baseline growth rate. All behavior for the CBO = 80 condition were derived from a single specimen, and it is possible that the material variability is influencing those data. When disregarding the CBO = 80 data, there was a trend that the OLR = 1.25 increased the growth rate over the baseline for all conditions, and there is no apparent retardation, as was seen in IN100 under similar block loading [31].

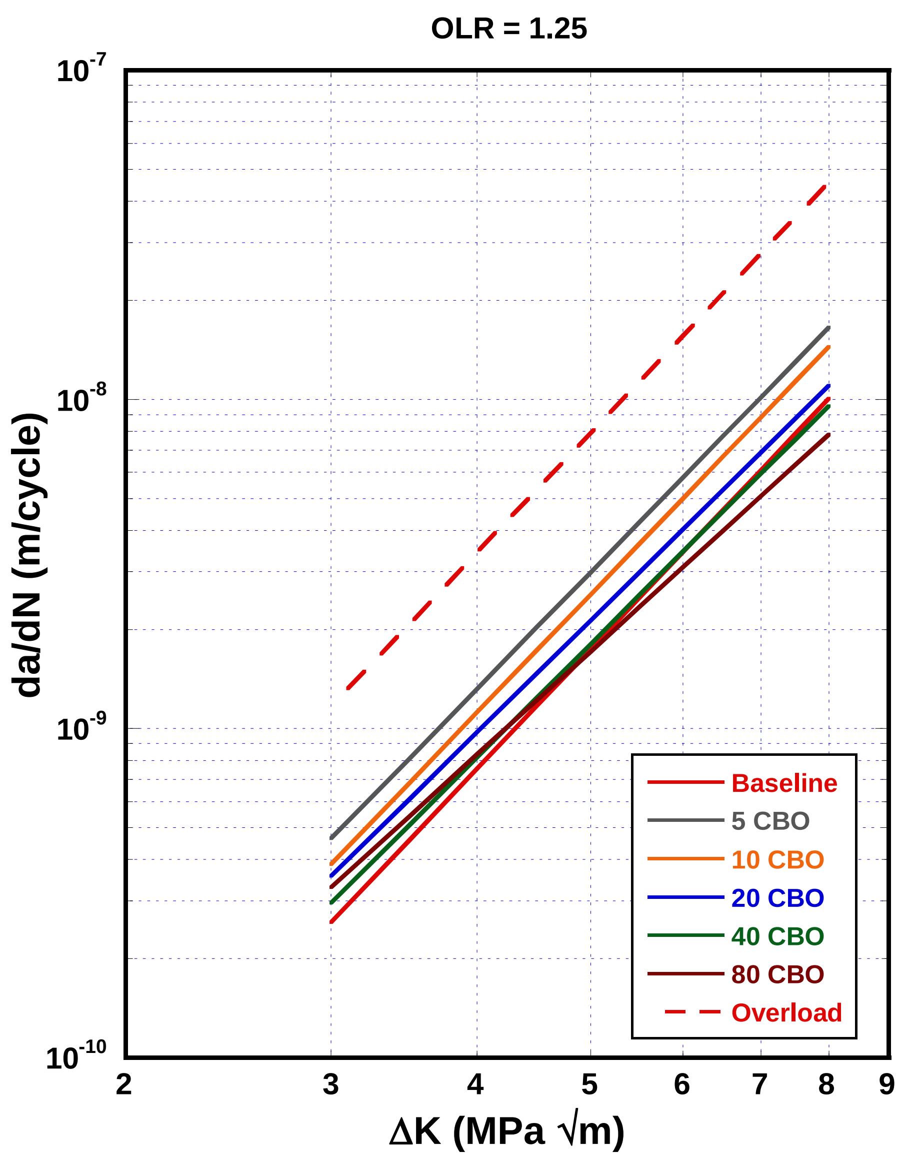

Figure 16: Master Fits OLR = 1.25 [da/dN vs ΔK]

The crack growth rate data, da/dN vs ΔK, for OLR = 1.50 and the various CBOs are shown in Figure 17. As before the dashed line plots the crack growth rate of the overload cycling as referenced to the baseline ΔK – representing the CBO = 0 condition.

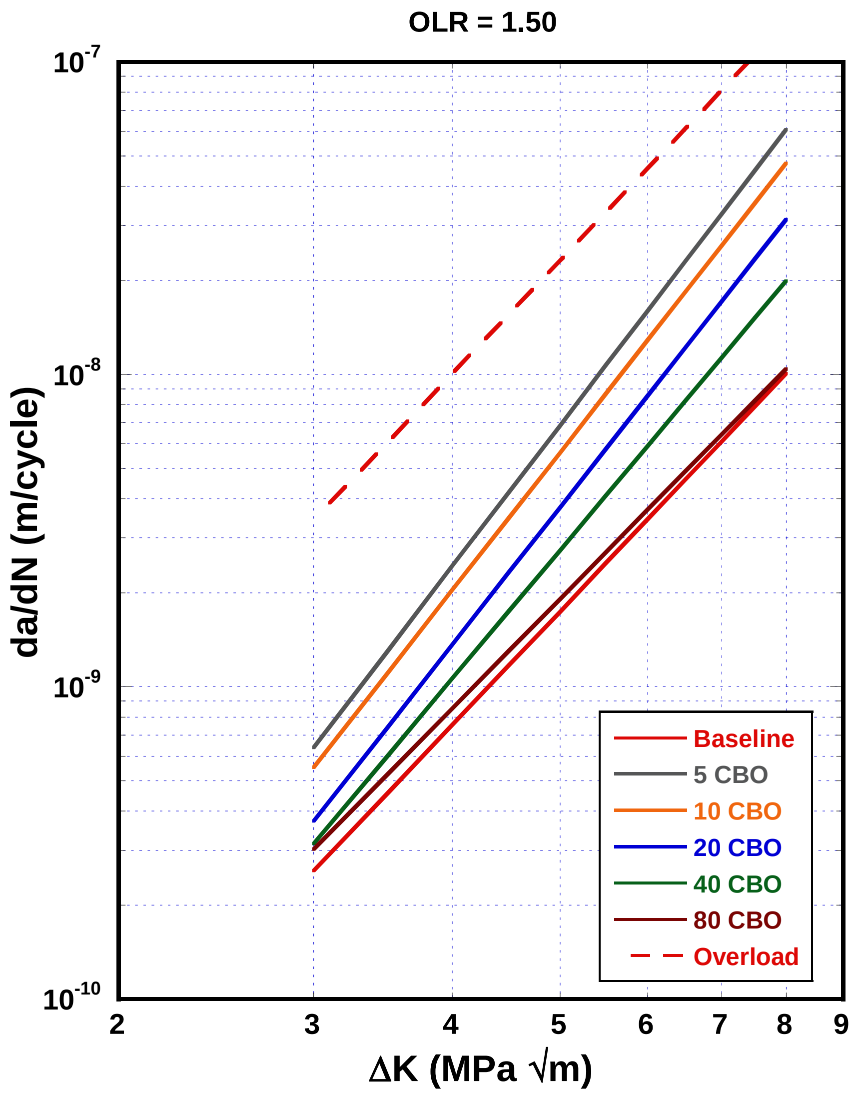

Figure 17: Master Fits OLR = 1.50 [da/dN vs ΔK]

Again, the crack growth curves layer wherein the lowest CBO has the fastest growth rate and the largest CBO has the slowest growth rate. In all cases, the periodic overload increased the growth rate as compared to the baseline. It is noted that the CBO = 5, 10, 20, and 40 had Paris exponents that were significantly higher than the baseline, while the CBO = 80 has a Paris exponent that was lower than the baseline. Again, the CBO = 80 data were from a single specimen and had a significantly smaller number of data points (only 5) in comparison to the other cases. It could be that experimental variability is affecting these data as well. The significantly higher

Paris exponent for the CBO = 5, 10, 20, and 40 means that as ΔK increases, the curve's distance from the baseline curve increases. However, the CBO = 80 result indicates that higher CBO crack growth behavior trends to the baseline, as it should.

CHAPTER VI

DISCUSSION

While an aircraft is in flight, the stress ratio values in the engine are largely positive. This leaves a number of possible stress ratio values to consider for testing. The concept of crack closure has been discussed in previous sections. Throughout testing a stress ratio of 0.5 was used. This ratio was selected in order to assure that crack closure effects were negligible. By not having to accommodate the effects of crack closure, the test program was able to focus on intrinsic effects of overloads in Ti-6Al-2Sn-4Zr-2Mo. A total of five C(T) specimens was tested.

Single Overload

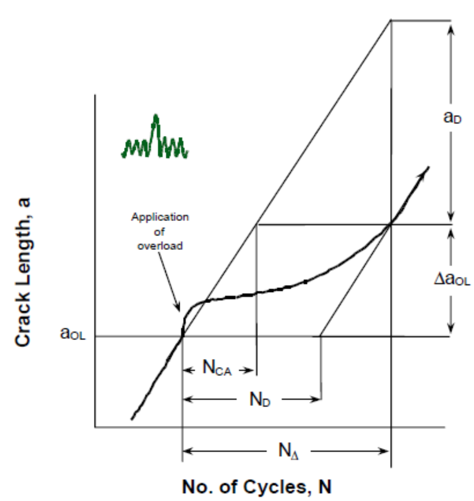

Figure 18: Single OL [a vs N] Description [10]

Figures 11 and 18 depict a typical single OL in terms of crack length versus number of cycles. When overloads do not produce fracture, they generally result in crack growth retardation and as such are considered beneficial to fatigue crack growth [10]. In the figure, N_{Δ} equals the number of cycles necessary to return to a steady-state crack growth rate, and Δa_{OL} is the corresponding increase in crack length needed to resume the steady-state growth rate. N_{CA} equals the number of cycles under constant amplitude to reach the same crack size. The number of delay cycles, N_D, equals N_{Δ} - N_{CA}, which is a measure of the extent of the retardation effect [10].

An overload causes a larger plastic zone to develop ahead of the crack tip. Initially the fatigue crack growth rate accelerates due to the higher stress intensity factor of the overload. The dominant behavior after an overload, however, is crack growth retardation. For low stress rations, once the overload is applied, the crack closure level begins to increase to a maximum, slowing the crack, and then closure gradually decreases to the normal level as the crack grows though the larger plastic zone [32]. After the initial acceleration of the fatigue crack, the crack growth rate decelerates to a minimum value at some point after the overload application, called delayed retardation; see Figure 19. Subsequently, the crack growth rate gradually returns to its steady state value [15]. This is the theoretical single overload (SOL) outcome for various materials at low stress ratios.

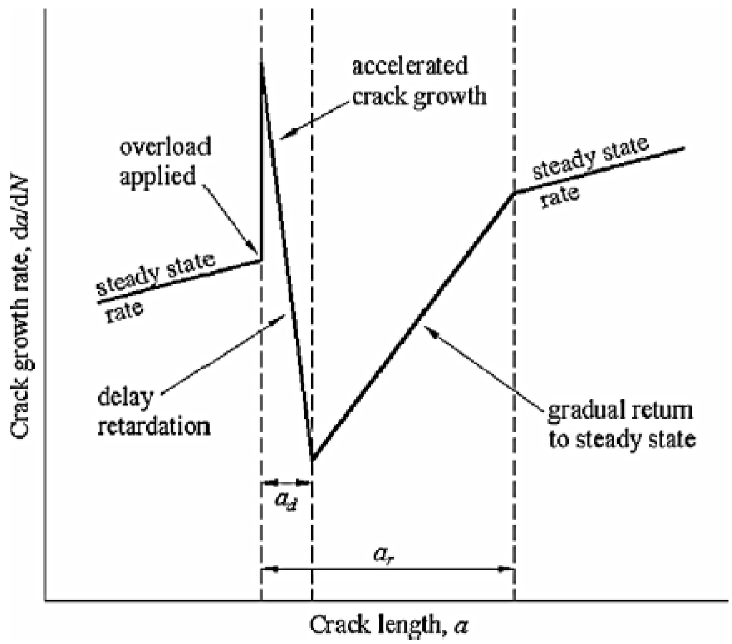

Figure 19: Schematic Crack Growth Rate Curve Showing Delayed Retardation Following Tensile Overload [15]

It is important to estimate the plastic zone size in front of the crack tip in considering the effect of single and sequential load interactions. Directly ahead of the crack tip, the baseline plastic zone size is called, $r_{p,i}$. The baseline plastic zone is formed from the constant baseline maximum K level and remains throughout block load testing. The overload plastic zone, $r_{P,OL}$, is formed from the application of an overload. The effects of the overload plastic zone are evident until the end of the transition from the baseline to overload plastic zone, at which point the baseline plastic zone makes contact with the forward boundary of the overload plastic zone or the single overload case. Figure 20 depicts a C(T) specimen and the baseline and overload plastic zones (great enlarged for illustration). Also shown are the instantaneous crack length (a_i), the overload crack length (a_{OL}), and the crack length to the forward extent of overload plastic zone (a_P).

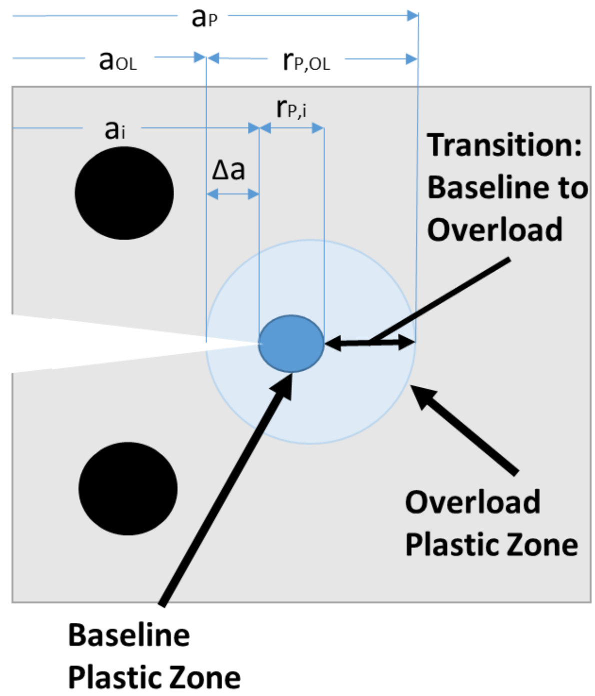

Figure 20: Plastic Zone Sizes

The overload plastic zone ($r_{p,OL}$) and the baseline plastic zone ($r_{p,i}$) size calculations are shown in Table 6. The sizes of $r_{p,i}$ and $r_{p,OL}$ are obtained by the following equations:

$$rp,i = \alpha\left[\frac{Kmax}{\sigma ys}\right]^2 \qquad (2.9) \qquad\qquad rp,OL = \alpha\left[\frac{Kmax,OL}{\sigma ys}\right]^2 \qquad (3.0)$$

α = Plastic Zone Size Constraint Factor

σ_{ys} = yield stress

Constraint around the crack tip determines the plastic zone size factor. Here, the monotonic plastic zone size (diameter) factor α varies between 1/π for plane stress and 1/3π for plane strain [9]. Table 6's calculations for baseline and overload plastic zone sizes were used to show the number of crack growth baseline cycles needed after an overload for a return to steady state crack growth rate.

Table 6: Plastic Zone Sizes

Plastic Zone Sizes									
Plane Stress	OLR	Kmax,OL (MPa√m)	Kmax (MPa√m)	ΔK (MPa√m)	rp,OL (um)	rp,i (um)	Δrp (um)	Baseline da/dN (m/cycle)	Cycles
	1.25	7.5	6	3	21.15	13.54	7.62	2.581E-10	29506
		10	8	4	37.61	24.07	13.54	7.556E-10	17918
		12.5	10	5	58.76	37.61	21.15	1.738E-09	12169
		15	12	6	84.62	54.15	30.46	3.434E-09	8871
		18.75	15	7.5	132.21	84.62	47.60	7.900E-09	6025
	1.5	9	6	3	30.46	13.54	16.92	2.581E-10	65570
		12	8	4	54.15	24.07	30.09	7.556E-10	39817
		15	10	5	84.62	37.61	47.01	1.738E-09	27042
		18	12	6	121.85	54.15	67.69	3.434E-09	19713
		22.5	15	7.5	190.39	84.62	105.77	7.900E-09	13388
Plane Stress	OLR	Kmax,OL (MPa√m)	Kmax (MPa√m)	ΔK (MPa√m)	rp,OL (um)	rp,i (um)	Δrp (um)	Baseline da/dN (m/cycle)	Cycles
	1.25	7.5	6	3	7.05	4.51	2.54	2.581E-10	9835
		10	8	4	12.54	8.02	4.51	7.556E-10	5973
		12.5	10	5	19.59	12.54	7.05	1.738E-09	4056
		15	12	6	28.21	18.05	10.15	3.434E-09	2957
		18.75	15	7.5	44.07	28.21	15.87	7.900E-09	2008
	1.5	9	6	3	10.15	4.51	5.64	2.581E-10	21857
		12	8	4	18.05	8.02	10.03	7.556E-10	13272
		15	10	5	28.21	12.54	15.67	1.738E-09	9014
		18	12	6	40.62	18.05	22.56	3.434E-09	6571
		22.5	15	7.5	63.46	28.21	35.26	7.900E-09	4463

Δrp above is the difference between the baseline plastic zone and the overload plastic zone, which is the theoretical amount of crack growth needed after an overload for a return to steady state crack growth rate. The number of cycles required to grow the crack this distance at the baseline crack growth rate is also shown in the table. Figures 21 and 22 show the single overload crack growth (a-N) and crack growth rate (da/dN-ΔK) results for two control conditions at Kmax = 10 with OLR = 1.25 and 1.50. The immediate increase in crack growth rate after the application of the single overload is shown, along with the total distance required to return to steady state after an overload. These figures depict the crack length (a) on the primary y-axis, the number of cycles (N) on the x-axis, and crack growth rate (da/dN) on the secondary y-axis. From these data, the accelerated crack growth, delay retardation, and gradual return to steady state are measured. These figures were created using Mathematica with a Gaussian filtering and sliding quadratic polynomial smoothing technique, which allows for different levels of filtering and/or smoothing in da/dN and a vs N. The blue points depicted in each figure shows the a vs N curve, while the grey points represent da/dN vs N. All other dashed lines are labeled accordingly on each plot. Both Figure 21 and 22 presents an a vs N curve that showed an increase in crack growth rate after the overload is applied but no retardation. As well as, there is no difference between constant ΔK controlled and constant ΔP controlled testing. See APPENDIX A: Single Overload [da/dN, a vs N] for more examples.

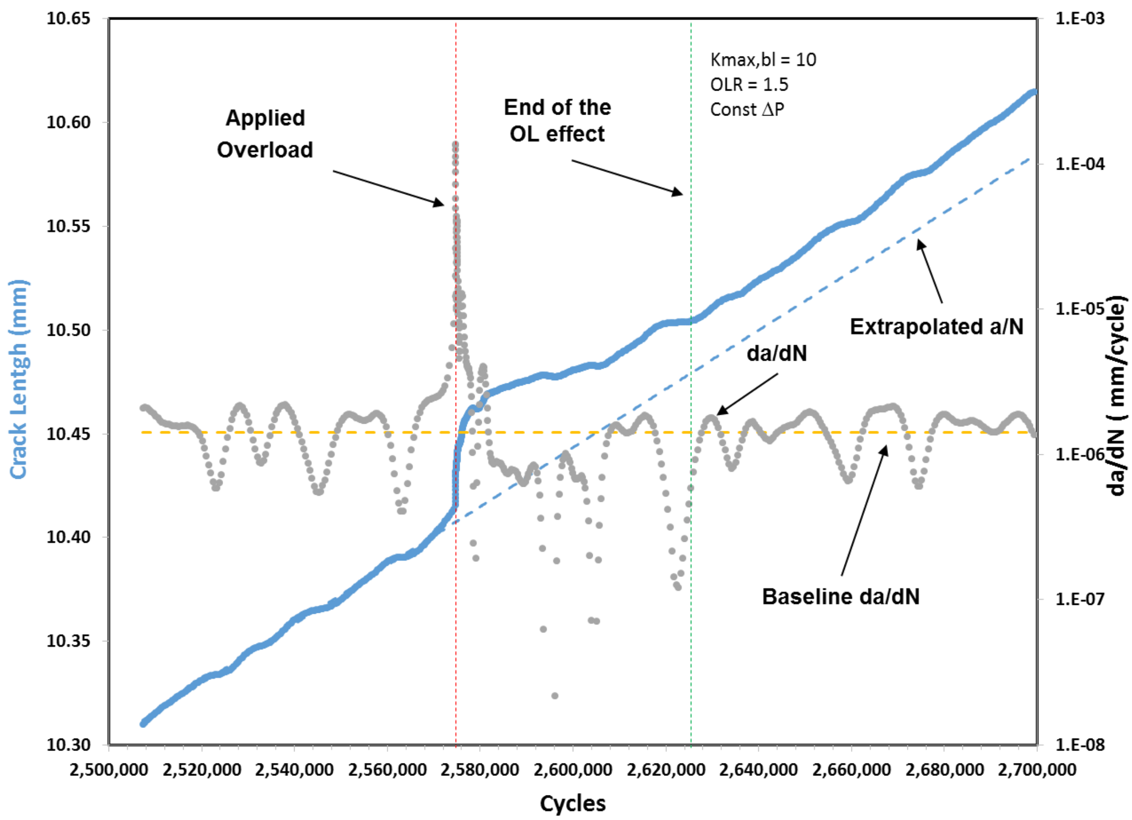

Figure 21: SOL K_{max} 10 OLR 1.50 Constant ΔP

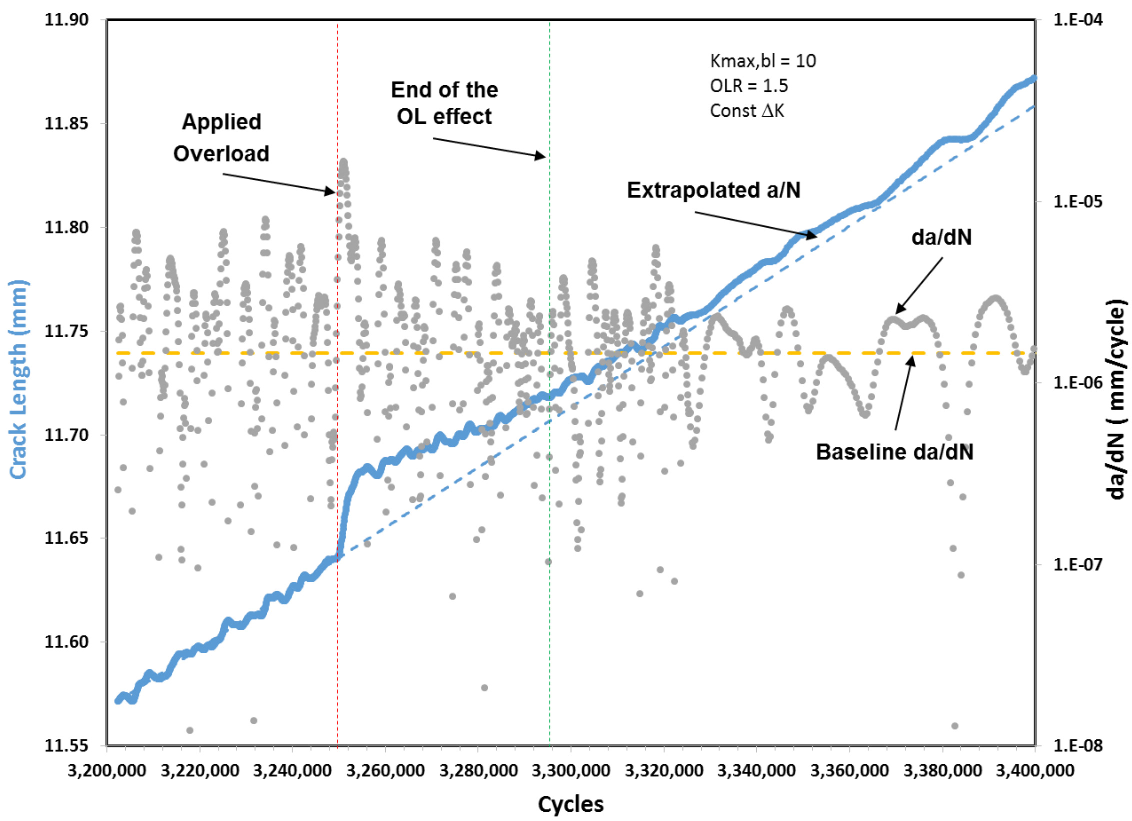

Figure 22: SOL K_{max} 10 OLR 1.50 Constant ΔK

Table 7, shows the total crack extension required to return to the steady state (SS) growth rate following the overload in comparison with the predicted extension. Also shown is the ratio of these two values.

Table 7: Plastic Zone Size Comparison

OLR	Kmax,OL	Kmax	Control	Total Return to SS (um) Actual	Plane *Stress* Prediction (um)	Prediction/Actual
1.25	12.5	10	K	59	21	0.36
1.5	15	10	P	60	47	0.78
1.5	15	10	K	65	47	0.72
1.25	18.75	15	K	50	48	0.95
1.25	18.75	15	P	70	48	0.68
1.5	22.5	15	K	75	106	1.41
1.5	22.5	15	P	200	106	0.53

OLR	Kmax,OL	Kmax	Control	Total Return to SS (um) Actual	Plane *Strain* Prediction (um)	Prediction/Actual
1.25	12.5	10	K	59	7	0.12
1.5	15	10	P	60	16	0.26
1.5	15	10	K	65	16	0.24
1.25	18.75	15	K	50	16	0.32
1.25	18.75	15	P	70	16	0.23
1.5	22.5	15	K	75	35	0.47
1.5	22.5	15	P	200	35	0.18

Due to variability in the crack growth rates, the measured point of return to steady state results shown in the table above are subjective, and therefore do not provide a solid answer to compare to the predicted results. A common theme however, was the ratio of accelerated crack growth to retardation. That is, the crack growth rate was affected for a larger distance than calculated, based on comparison of the baseline and overload plastic zone sizes. The acceleration was continuously larger than the retardation throughout SOL testing, meaning, that the acceleration was more damaging than the retardation was beneficial. This can be noticeably perceived through the da/dN log scale axis. The difference in scale shows the more influential impact of the accelerated crack growth, related to any retardation.

Repeat Overloads

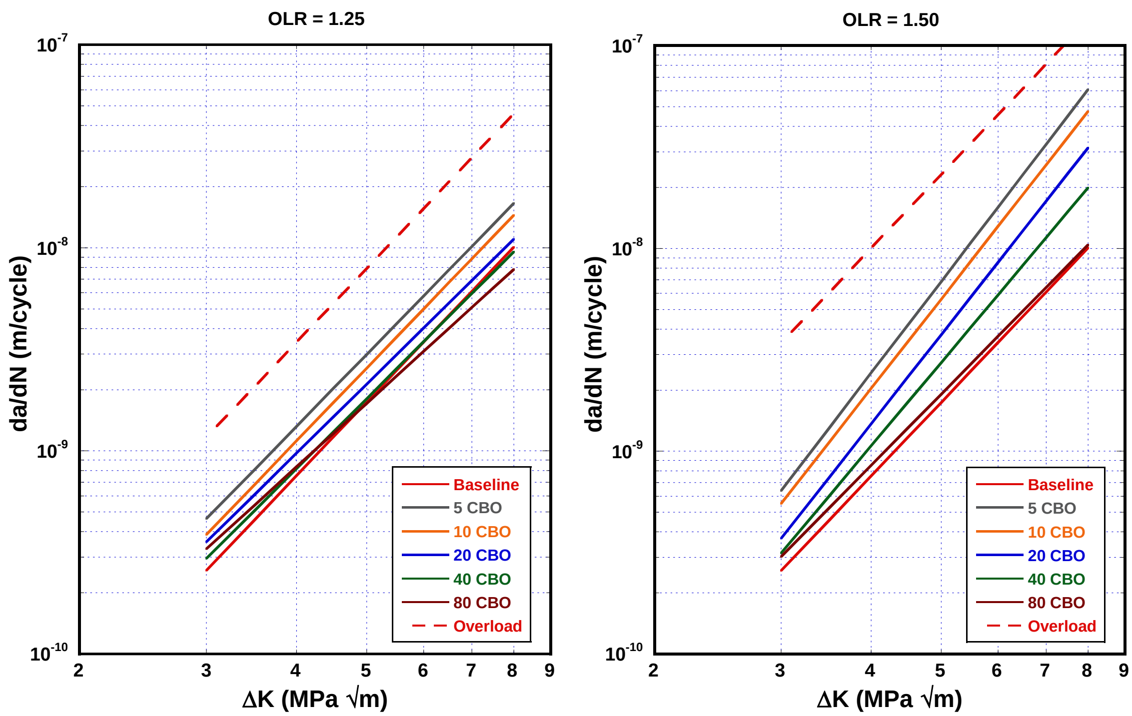

Figure 23: Master Fits OLR = 1.25 and 1.50

The Paris law constants from the Master Fits depicted above were already showcased in the results section, Figure 16 and 17, and these curves are pictured again in Figure 23, since they the foundation of the figures to come. For example, an alternative way to look at the crack growth data with periodic overload is found in Figure 24 where the crack growth rate as calculated from the Paris law constants is plotted versus CBO for various ΔK levels with OLR = 1.25. The dashed line indicates the baseline growth rate at that particular ΔK.

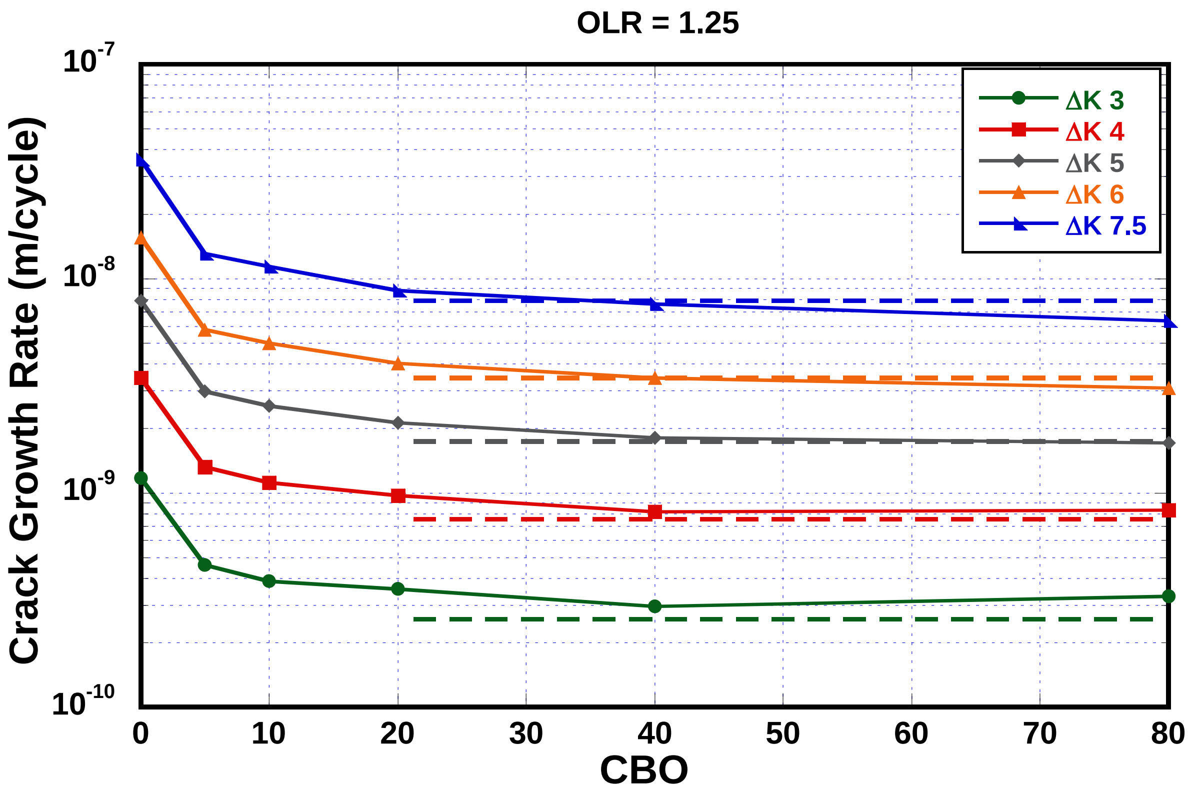

Figure 24: Paris Power Law OLR = 1.25 [da/dN vs CBO]

At the higher-level ΔK's of 5, 6, and 7.5, the crack growth rates eventually slowed to or just below, the baseline crack growth rate. The crack growth rates took longer to match the baseline at lower ΔK's, 3 and 4. Remember that the CBO = 80 results were not as robust as the other results. The effects of retardation are pulling the higher-level ΔK down to just below baseline between 20 to 40 CBO. The lower levels of ΔK take a little longer.

The behavior with the higher OLR = 1.50 is shown in Figure 25. The behavior for this condition is subtly different. Compared to the OLR = 1.25, the higher ΔK's approach the baseline slower than the low ΔK's.

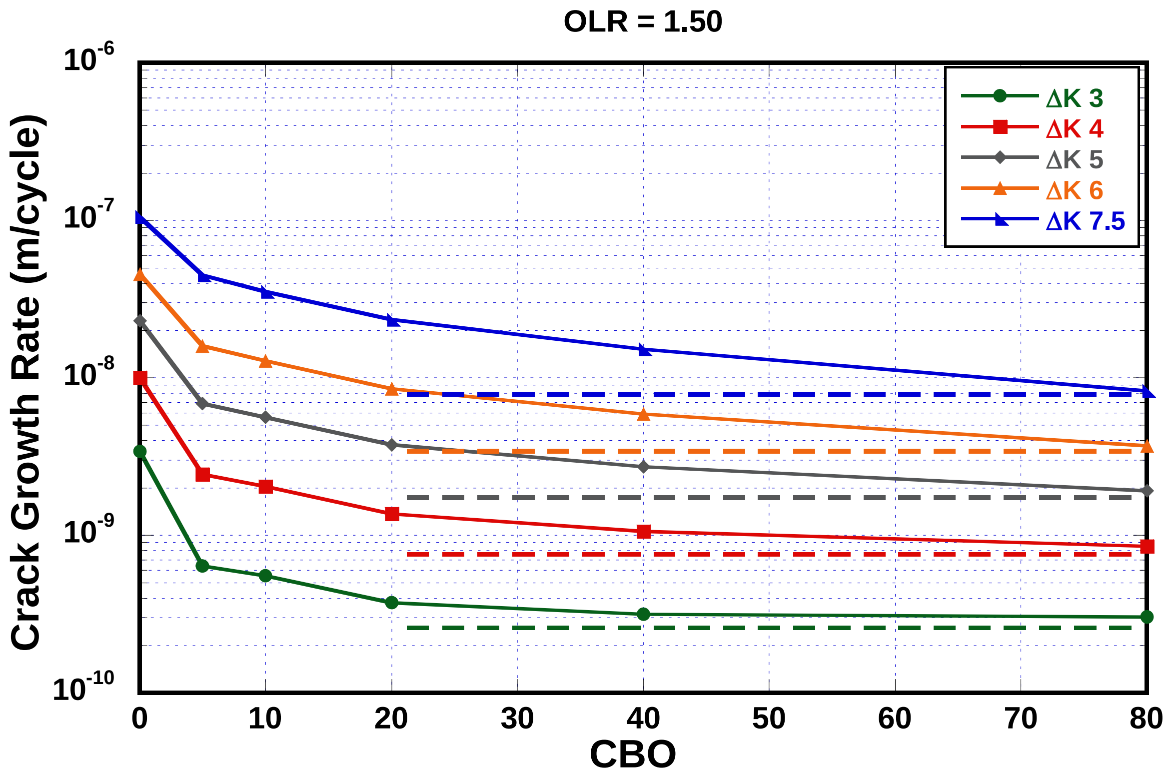

Figure 25: Paris Power Law OLR = 1.50 [da/dN vs CBO]

The overloads ratios of 1.50 produced a greater to increase crack growth rate. None of the ΔK levels crossed below the baseline rate by 80 CBO. However, the ΔK's of 3 and 4 were close to the baseline by CBO = 40, while the higher ΔK's were still significantly above the baseline at that CBO.

Miner's rule is the simplest linear damage model that can be applied to the periodic overload results, and it ignores all load interaction. This simple calculation shown below can be used to explain some of the behavior observed in the experiments.

$$\left(CBO * Baseline\left(\frac{da}{dN}\right) + OL\left(\frac{da}{dN}\right)\right)/(CBO + OL) \tag{3.1}$$

Baseline (da/dN) = baseline crack growth rate [da/dN]

OL (da/dN) = overload crack growth rate [da/dN]

Figure 26 and 27 show these calculations in terms of crack growth rate versus CBO at various ΔK levels for OLR = 1.25 and 1.50, respectively.

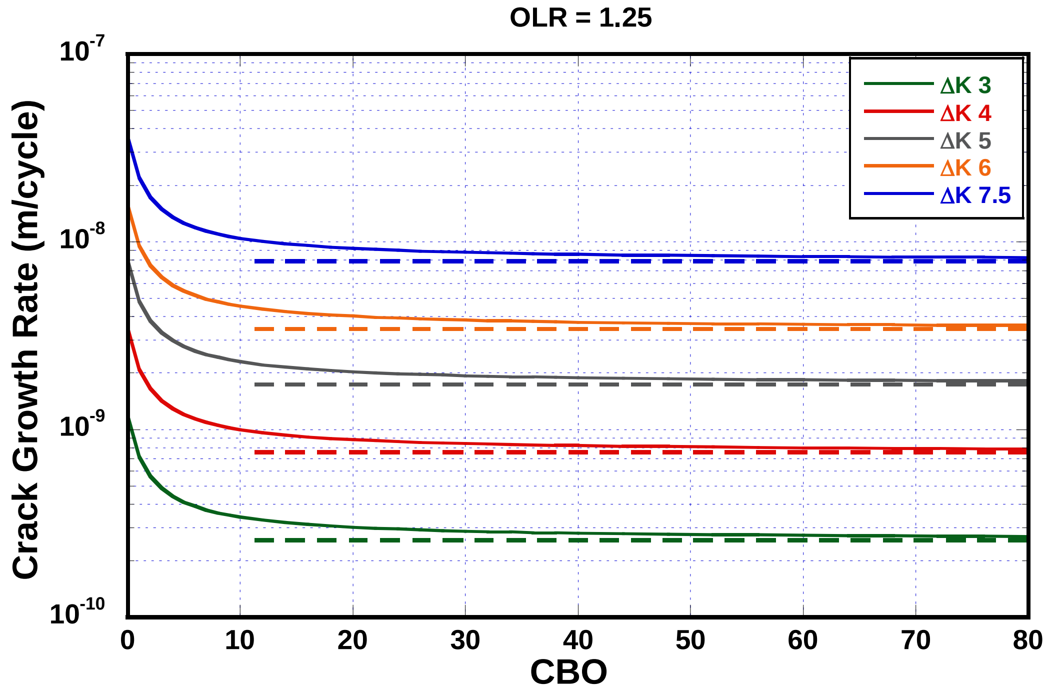

Figure 26: Miners Rule OLR = 1.25 [da/dN vs CBO]

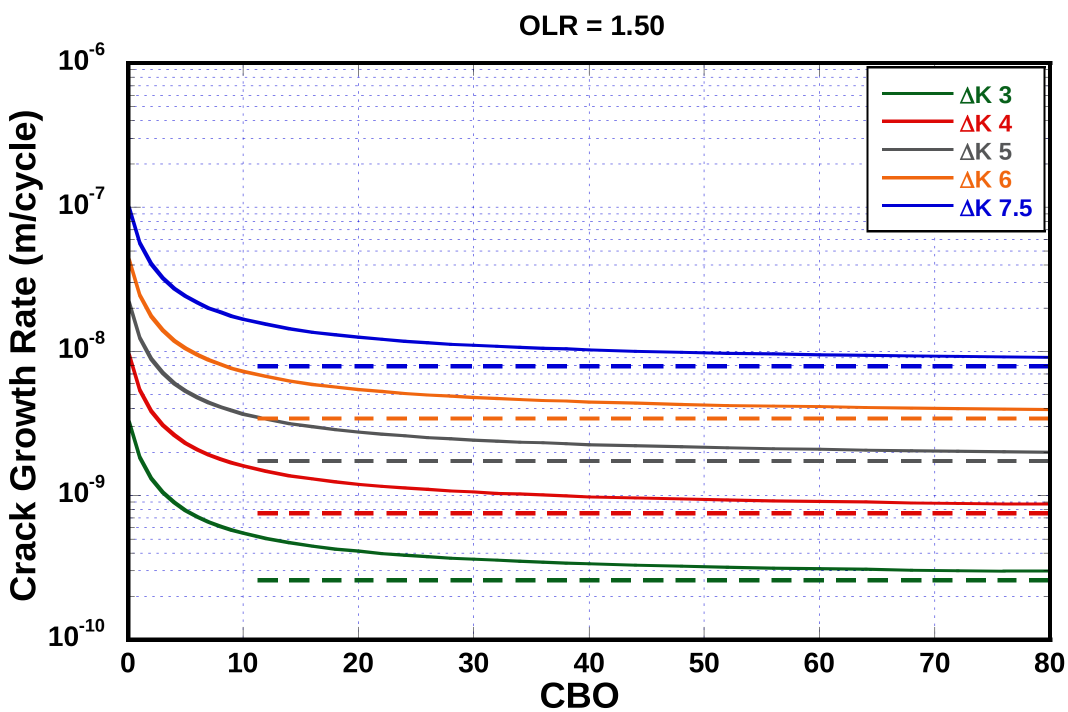

Figure 27: Miners Rule OLR = 1.50 [da/dN vs CBO]

Miner's rule obviously trends toward the baseline but technically will never reach it and cannot predict retardation below the baseline. The OLR = 1.25 is uniformly within 8.6% of the baseline by CBO = 40, and the OLR = 1.50 takes more cycles, CBO = 145, to get that close to the baseline.

Figure 28 and 29 show the direct comparison of Miner's rule and the experiments in terms of crack growth rate versus CBO at various ΔK's for OLR = 1.25 and 1.50, respectively.

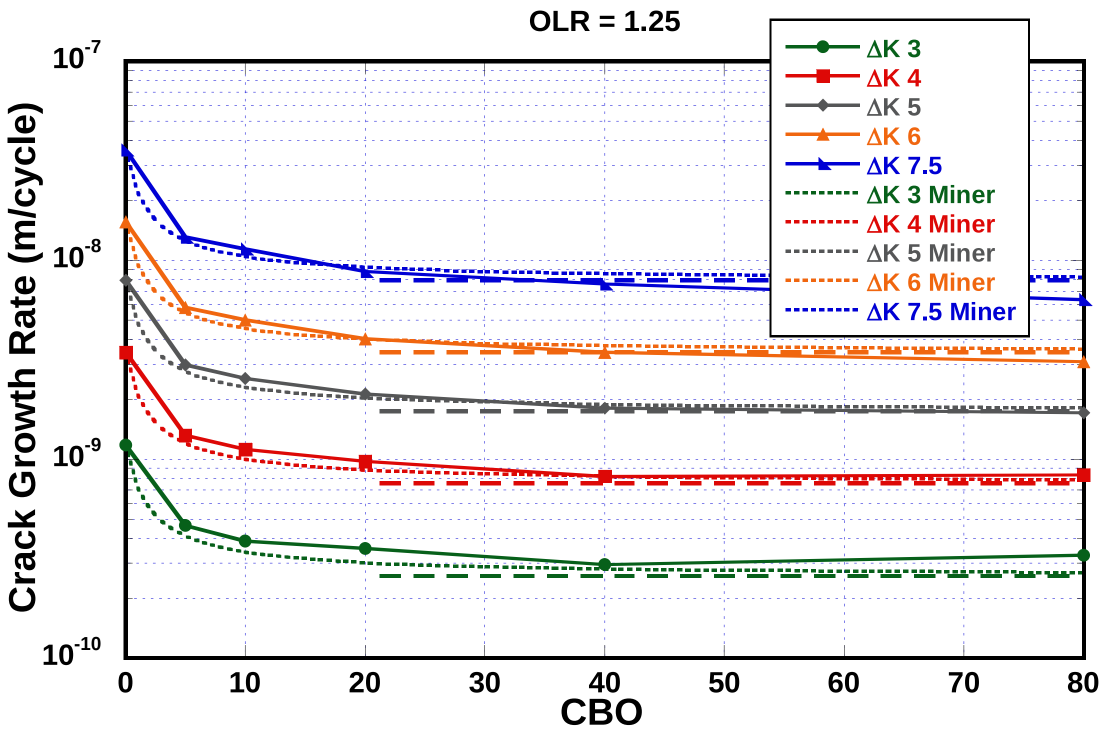

Figure 28: Direct Comparison of Paris and Miner's OLR = 1.25 [da/dN vs CBO]

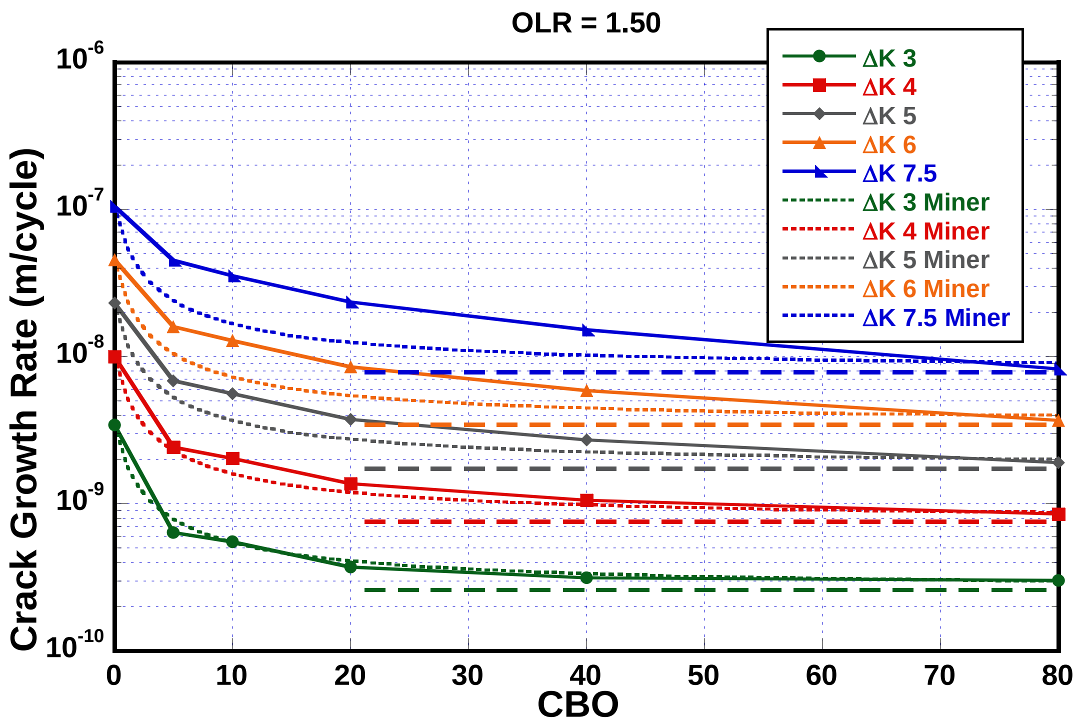

Figure 29: Direct Comparison of Paris and Miner's OLR = 1.50 [da/dN vs CBO]

The OLR = 1.25, Figure 28, is well predicted by linear damage summation of the Miner's rule indicating, surprisingly, that load interaction does not strongly contribute to the crack growth rate for these low overloads. The increased overload, OLR = 1.50, is well predicted by Miner's rule at low ΔK, but Miner's rule increasingly under predicts the crack growth rate as ΔK increases – especially in the range of CBO = 10 to 20, Figure 29. The fact that the cracks are growing faster at high ΔK means that the overload is not retarding the crack due a compressive residual stress, and it must be inducing damage ahead of the crack tip to accelerate the crack growth rate.

It is illustrative to compare the measured or actual crack growth rate versus the crack growth rate predicted by the Miner's rule calculation – termed A/P. When the ratio A/P > 1, the measured growth rate is faster than that predicted by Miner's rule. Figure 30 and 31 show A/P for the OLR = 1.25 and 1.50, respectively, as cumulative distribution functions. The values are grouped by their respective CBOs.

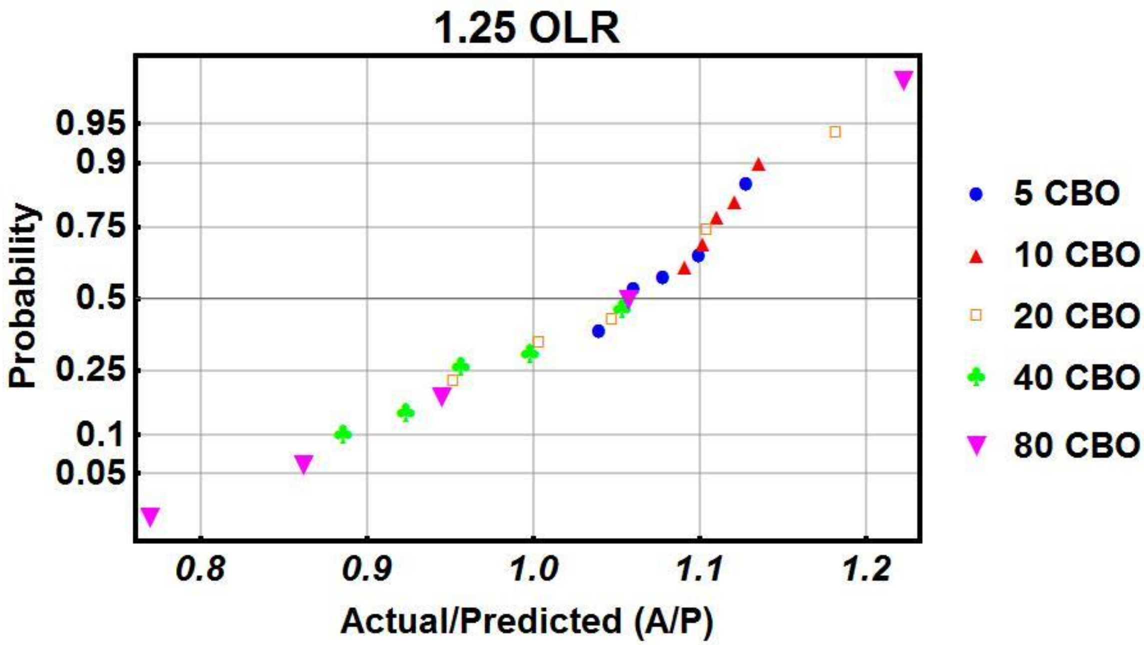

Figure 30: Probability vs A/P OLR = 1.25

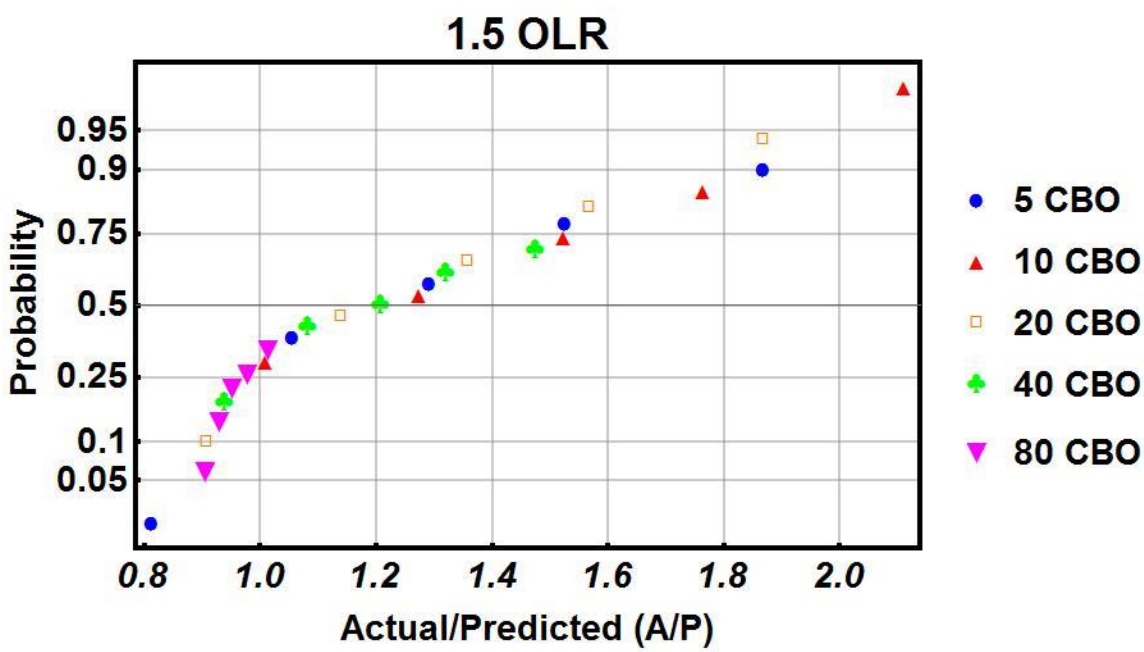

Figure 31: Probability vs A/P OLR = 1.5

The A/P for OLR = 1.25, Figure 30, is tightly grouped around 1, ranging from 0.77 to 1.3. This scatter is comparable to normal crack growth rate scatter, indicating that the Miner's rule does a relatively good job predicting the growth rates at relatively low OLRs. For the 1.50 OLR, the majority of the points had an A/P greater than 1. The values ranged from 0.82 to 2.15 with a 50% probability of about 1.2. This shows that the actual fatigue crack growth rates are mostly faster than the Miner's rule predictions. These are consistent with the results shown in Figure 28 and 29. The influence of CBO is relatively random with the exception of the CBO = 5 results, which are clumped at for both OLRs near the 50% probability and the CBO = 80 for the OLR = 1.50 condition where these results are distributed around A/P = 1.

Figure 32 plots the measured growth rates divided by the Miner's rule predictions (the same A/P) versus ΔK for CBO = 5 to 80. The results for OLR = 1.25 are shown as solid lines and OLR = 1.50 are dashed lines. Again the OLR = 1.25 is better predicted by Miner's rule, with the slopes of CBO = 5 to 40 being relatively flat with respect to ΔK. The CBO = 80 case exhibits the greatest ΔK dependence, growing faster the Miner's rule at low ΔK and slower at high ΔK. Again, recall that the CBO = 80 results are not as robust as the rest of the results. It would be expected that the CBO = 80 results would exhibit the least ΔK dependence, since at a large number of cycles between overloads the growth rate for both should trend towards the baseline growth rate.

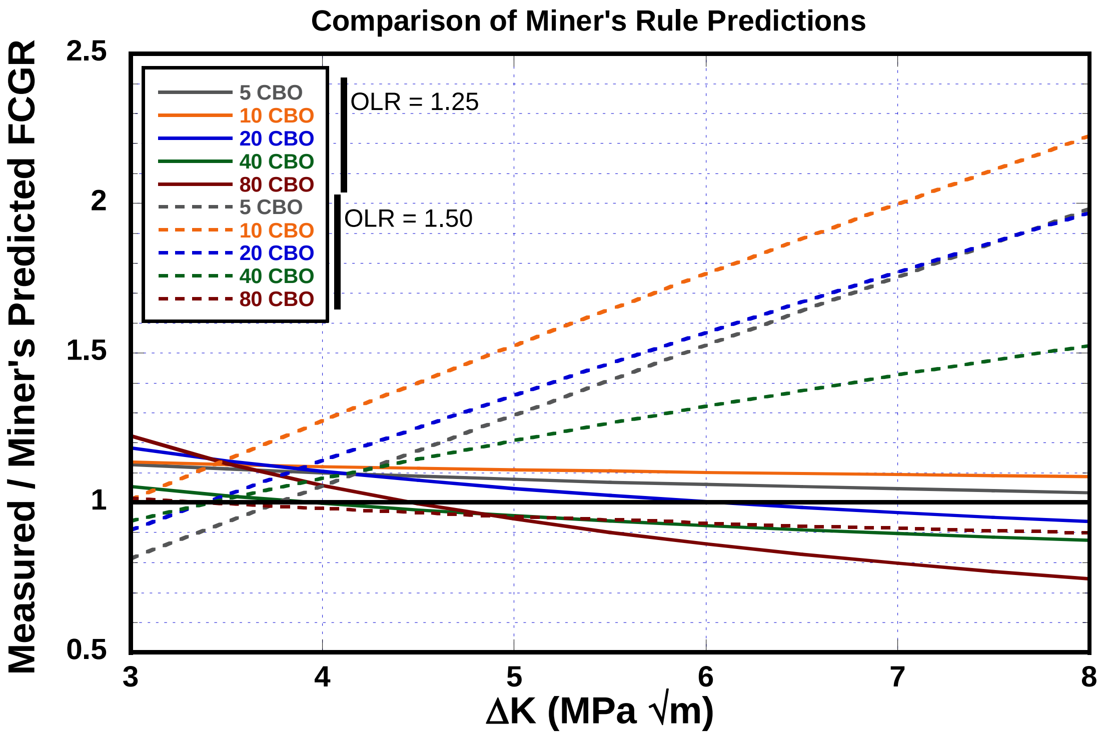

Figure 32: Comparison of Miner's Rule Predictions [Ratio vs delta K]

There is a clear separation in slope of the OLR 1.50 with CBO = 5, 10, 20, and 40, with the rest of field. The standard 2X approximate variation in crack growth rate is represented by A/P = 0.5 to A/P = 1.5. All of the OLR 1.25 lines slopes are similar, along with OLR 1.50's 80 CBO. Only the OLR = 1.50, CBO = 5 to 40 are outside of that scatter band and only at the higher ΔK. This supports the hypothesis that the higher overload must be damaging material ahead of the crack tip.

Figure 33 shows that subtracting the crack growth during a 20 CBO block from the growth observed during a 40 CBO block gives the average growth rate contribution from cycles 21 through 40 which eliminates effect of the overload and initial portion of the block. This is average growth rate is then plotted at 30 CBO or the average CBO of 20 and 40. The continued process on other blocks allowed for the completion of Figures 34 and 35, which depict the local crack growth rate calculated data points at varying ΔKs through 0 to 60 CBO at OLR 1.25 to 1.50.

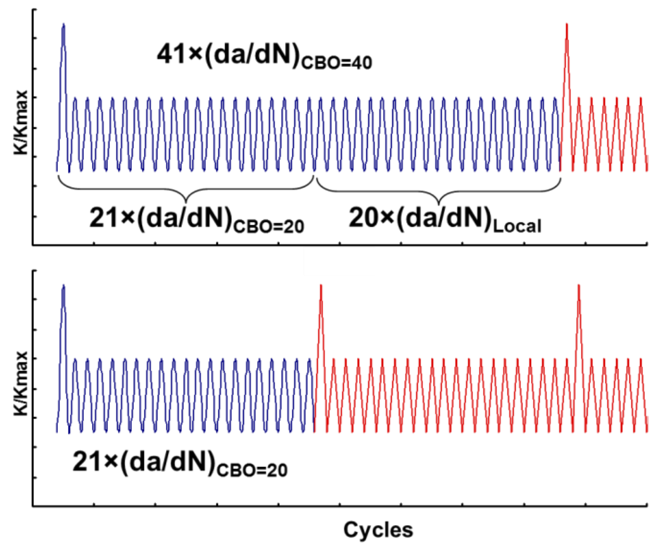

Figure 33: Local Crack Growth Rate Cycles

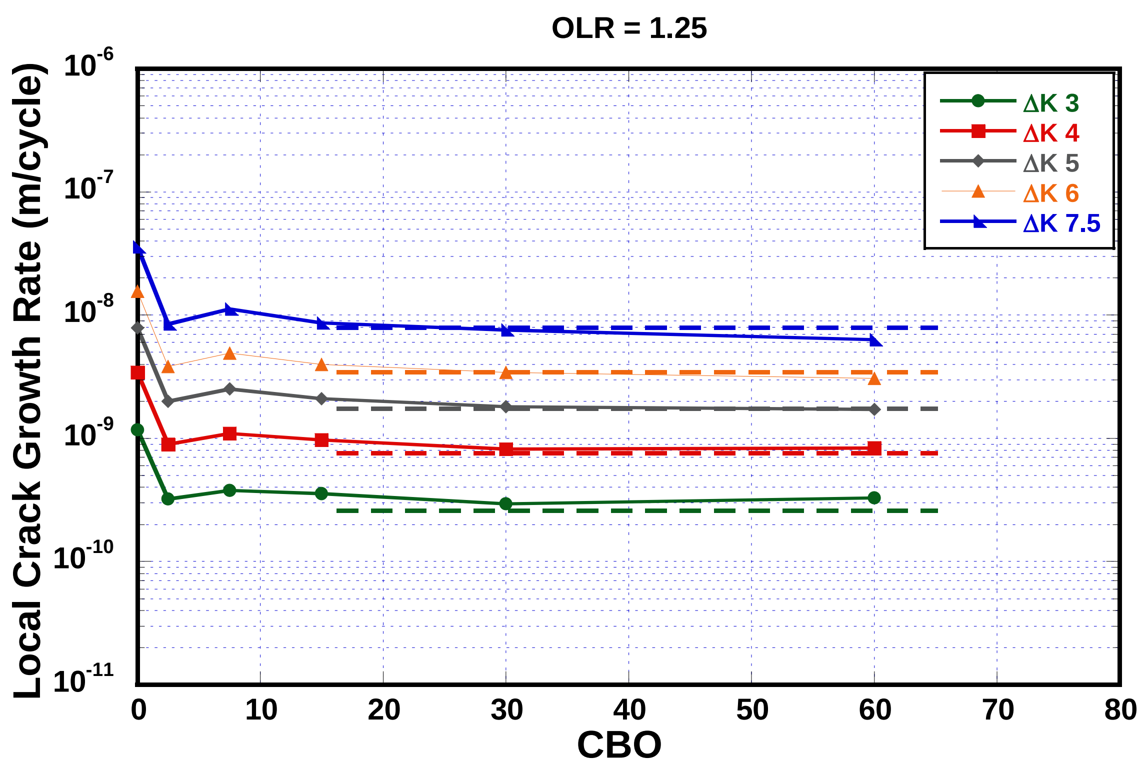

Figure 34: Local Crack Growth Rate OLR = 1.25 [da/dN vs CBO]

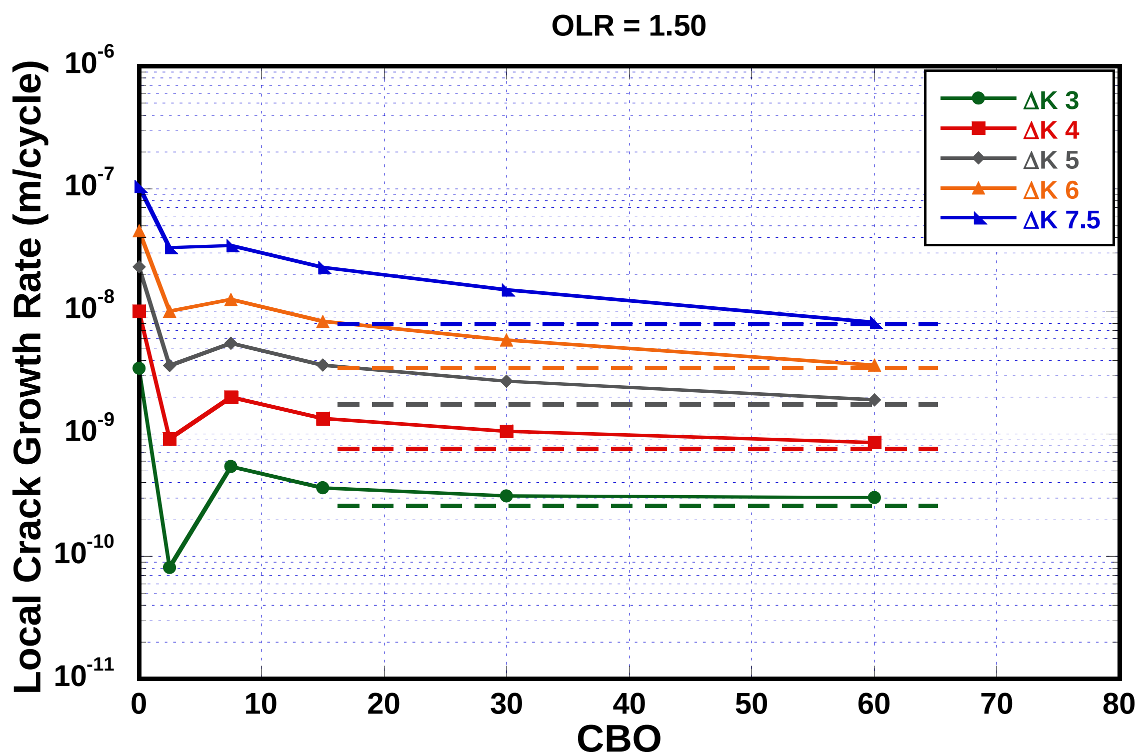

Figure 35: Local Crack Growth Rate OLR = 1.50 [da/dN vs CBO]

In Figure 34, the FCGR drops to the baseline right away, consistent with Miner's rule calculations, and the crack growth rates are relatively constant from 2.5 to 60 CBO. In Figure 35, the initial drop in FCGR at 2.5 CBO is greater for low ΔK's compared to high ΔK's. At 2.5 CBO, the local growth rate is lower than the baseline at ΔK of 3 but higher at the higher ΔK's. This is attributed to process zone damage. The slopes of OLR = 1.50 at ΔK's 4 to 7.5 would indicate that at higher CBOs the local crack growth rate would trend below the baseline.

An overall conclusion from the repeated overloads is that minor cycles are more damaging than traditionally thought, due to the acceleration in crack growth rate. This can be seen especially at the higher OLR and higher K levels. The results in terms of retardation were not as expected, based on historical understanding. In order to create a clear connection to what this means for turbine engines, two additional blocks were run. These blocks had the same conditions as the 5 CBO blocks at OLR = 1.25 and 1.50, except these blocks were performed in terms of underloads. For example, for the OLR = 1.50 there is a Kmax = 15 $MPa\sqrt{m}$, Kmin = 10 $MPa\sqrt{m}$, and an underload (UL) = 5 $MPa\sqrt{m}$, see Figure 36. The original overload waveform can be seen in Figure 37 where there is a Kmax = 10 $MPa\sqrt{m}$, Kmin = 5 $MPa\sqrt{m}$, and an OL = 15 $MPa\sqrt{m}$. That is, the major cycles are the same, 15 to 5 $MPa\sqrt{m}$, the minor cycles have the same ΔK, but the R is increased for the underload condition. Figure 38, shows a-N data for 3 OL blocks and 1 UL block. Focusing on the crack growth rates (da/dN) shown in Table 8, there is a negligible difference between the average crack growth rates, which means that the conditions of this overload study are applicable to the underload cycling. This was also seen in OLR = 1.25. The UL blocks allow for a more direct comparison of what happens during cycling, which will be explained in the following section.

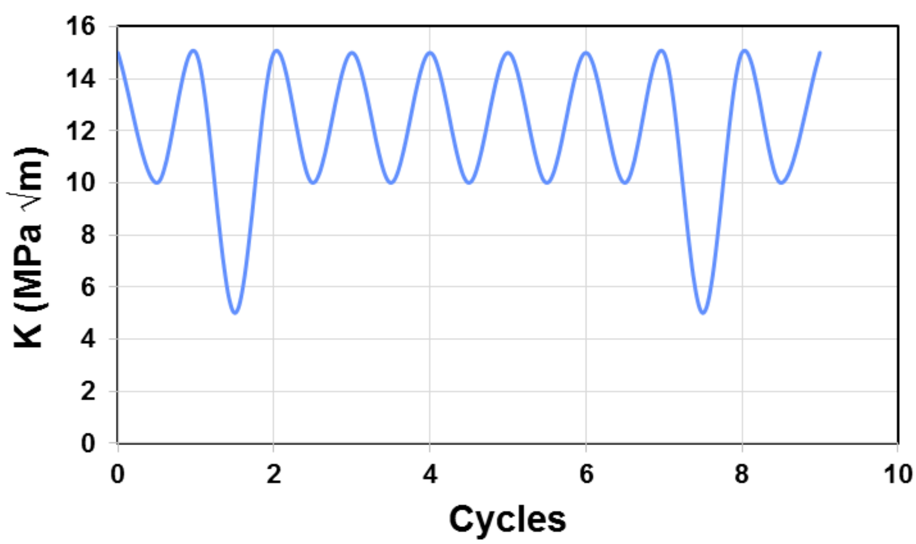

Figure 36: Waveform [Underload]

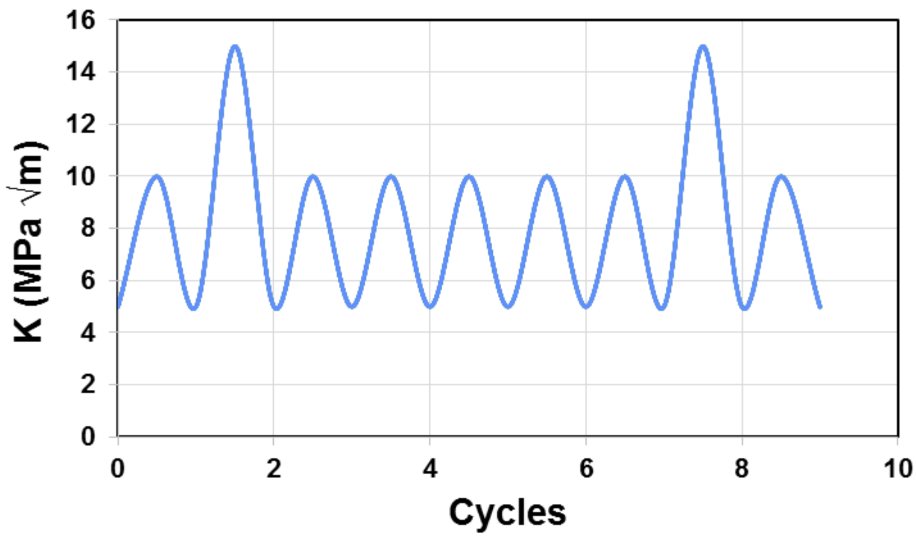

Figure 37: Waveform [Overload]

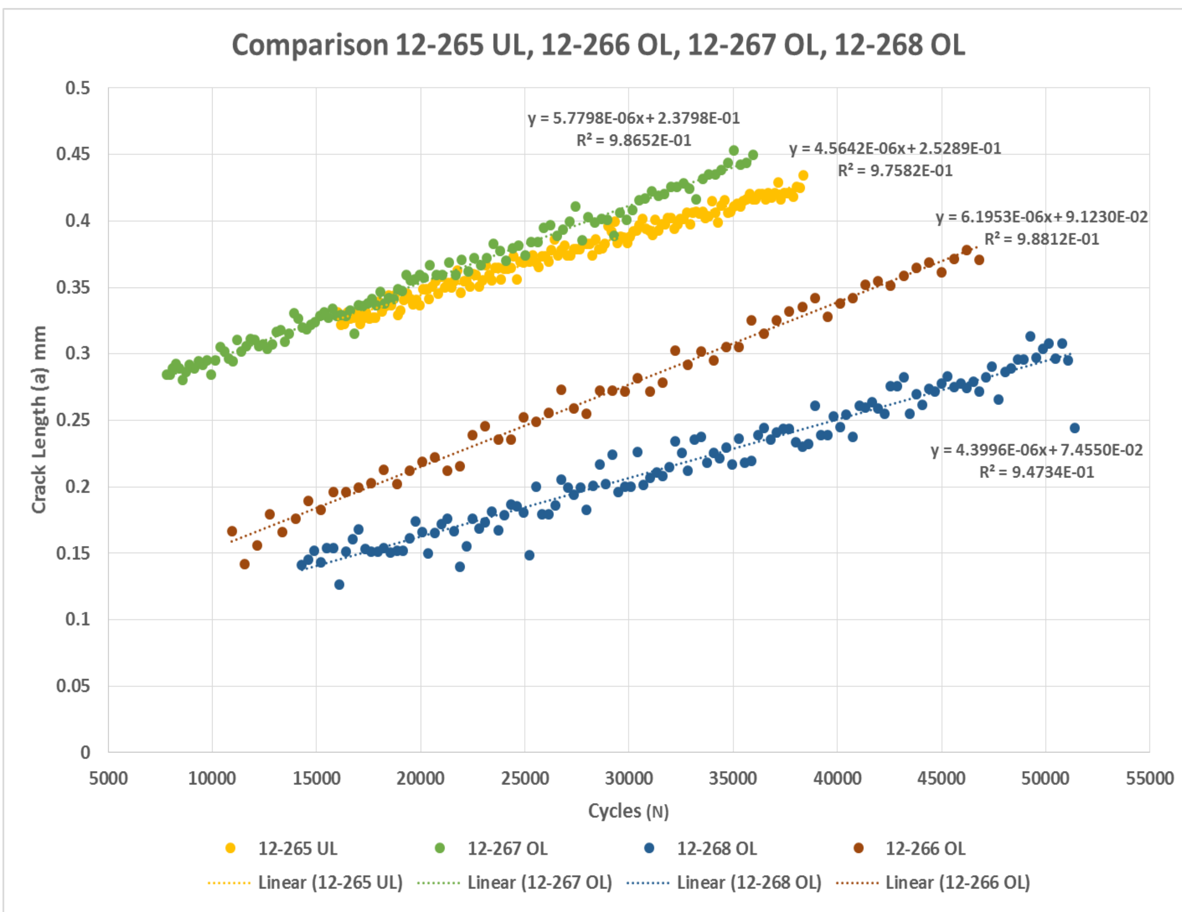

Figure 38: Comparison 12-265 UL, 12-266 OL, 12-267 OL, 12-268 OL

Table 8: Underload and Overload Comparison

Underload and Overload Comparison					
OLR = 1.5	12-265 UL:	12-266 OL:	12-267 OL:	12-268 OL:	Average OL:
da/dN	4.564E-06	6.195E-06	5.780E-06	4.400E-06	5.458E-06

Implications for Turbine Engine Lifing

The USAF tracks turbine engine usage by a cycle counting metric termed Total Accumulated Cycles (TACs). Each type of engine has an individual method to track TACs but the concept is similar for all engine types wherein the cyclic content of engine operation is monitored to count major and minor cycles. This is accomplished by tracking the engine rotor speeds; either the low pressure spool (N1), the fan and low turbine, or the high pressure spool (N2), the high compressor and high turbine. Some engine types simply track the throttle position or the power lever angle (PLA). These methods are used to track the cyclic nature of the engine operation because $\boldsymbol{\sigma}_{hoop} \propto \omega^2$, where ω is the rotational speed. PLA is related to rotational speed based on the thermodynamics of the engine operation, so all of the tracking methods are based on the same physics.

Typically, TACs are calculated for each flight or sortie through this equation [33]:

$$TAC = LCF + (.25\ x\ FTC) + (.025\ x\ CIC) \tag{3.2}$$

LCF – Low Cycle Fatigue or Type I

FTC – Full Thermal Cycle or Type III

CIC – Cruise Intermediate Cruise or Type IV

If the PLA is utilized to track the cyclic content of a sortie, the “gates” are set as follows: LCF are counted each time the PLA moves from 0 through 85 degrees, and then back to 0 degrees. This corresponds to a stop – full throttle (PLA = 85) – stop cycle and each flight has a single LCF cycle. FTC are counted each time the PLA moves from greater than or equal to 85 degrees down to less than or equal to 22 degrees, then back to greater than or equal to 85 degrees. This is tracked at one fourth of the damage of a major cycle. CIC are counted each time the PLA moves from greater than or equal to 85 degrees, down to any between 22 and 58 degrees, then back to greater than or equal to 85 degrees. This is the smallest cycle that is tracked and is counted as one fortieth of the damage of a major cycle.

Table 9, depicts a range of PLA, N1, and N2 from the F100 engine performance model in terms of normalized stress. In addition, it shows the level of normalized stress that triggers a count of LCF, FTC, and CIC. TACS are visually better represented as underloads. This is why the two-underload blocks were conducted; see Figure 39.

Table 9: PLA to Normalized Stress

PLA	Normalized Stress		
(°)	N1	N2	Average
0	0.0000	0.0000	0.0000
22	0.3279	0.5911	0.4595
58	0.8097	0.8494	0.8295
85	1.0000	1.0000	1.0000

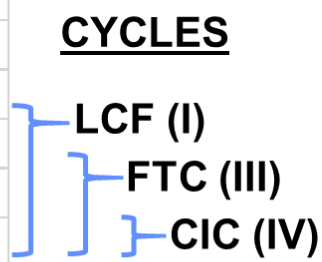

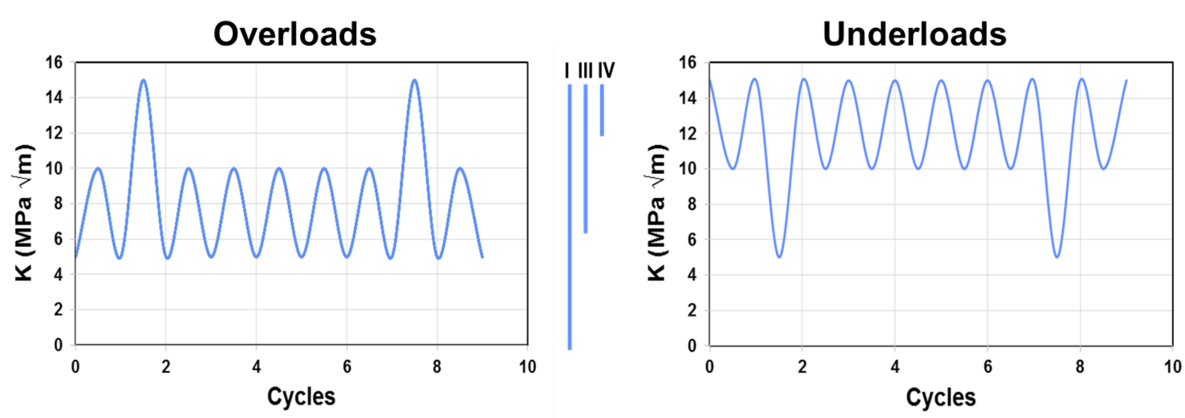

Figure 39: TAC Representation [Overload and Underload]

As depicted in Figure 40, in order to reach either LCF, FTC, or CIC, the cycle must cross a red dashed line representing a "gate." The gate normalized stress numbers were outlined in terms of PLA in Table 9. The schematic show, LCF was reached one time, and the FTC and CIC were reached three times.

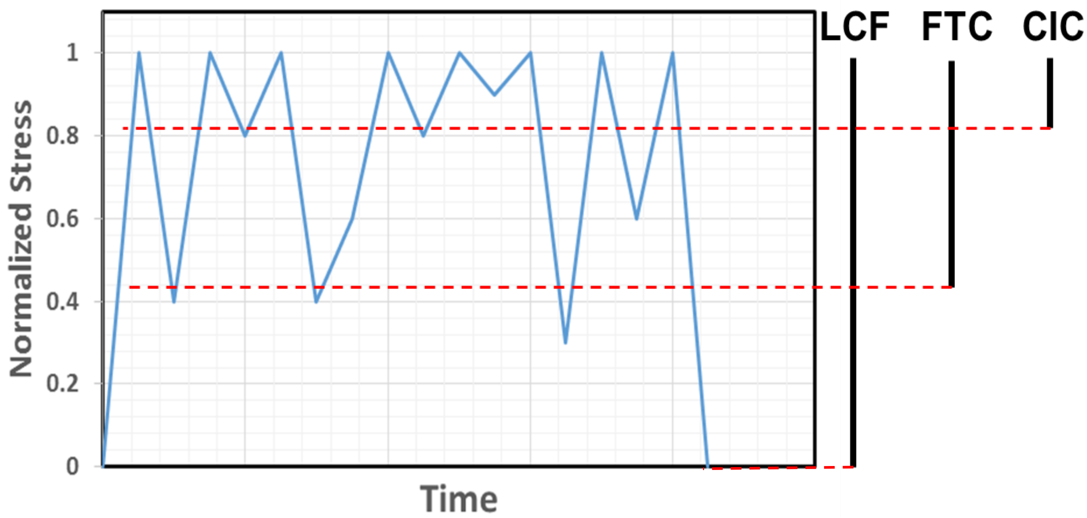

Figure 40: Normalized Stress vs PLA

The completed testing is a reflection of the minor cycles in turbine engines. Based on the TAC equation (3.2), the current testing contains both Type III (0.25 x FTC) and Type IV (0.025 x CIC) minor cycles. In Figure 41, the results suggest that minor cycles may be more damaging than a fourth or a fortieth of the major cycles. The black dashed line represents a fourth of a major cycle and the orange dashed line represents a fortieth of a major cycle. For OLR = 1.25, the crack growth rate of 5 and 10 CBO is higher than a fourth of a major cycle, meaning that the da/dN for those two CBOs has been more damaging than the fourth of a major cycle. This is certainly the case at the fortieth of a major cycle with the large change in da/dN. For OLR = 1.50, the crack growth rate for the fourth of a major cycle is overlapped at the higher ΔK's but the fortieth is completely overtaken in da/dN. In both OLR cases, the minor cycles of the fourth and the fortieth were conservative in terms of damage expected by equation 3.2.

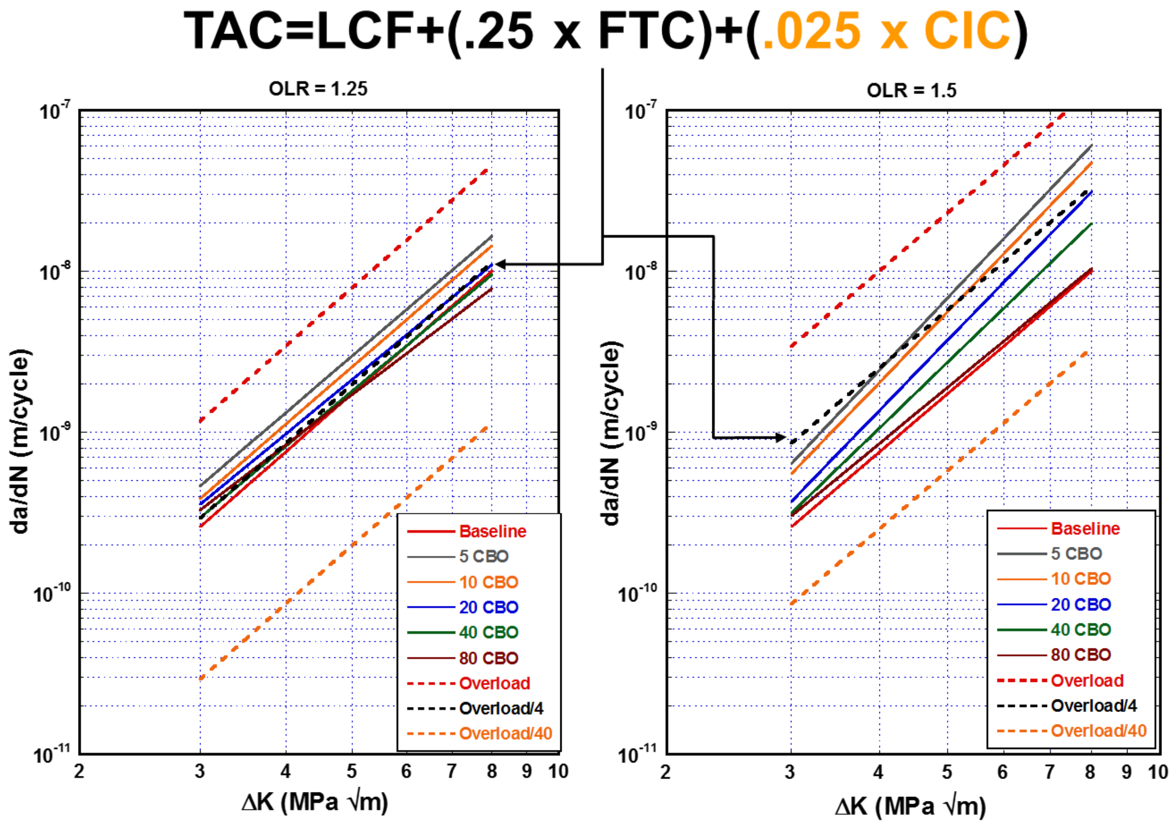

Figure 41: TAC Major and Minor Cycles [da/dN vs ΔK]

CHAPTER VII

CONCLUSIONS AND RECOMMENDATIONS

Conclusions

Aircraft turbine engines, especially military engines, experience variable amplitude loading during operation. The purpose of this study was to understand the effects of single and repeated overloads during fatigue crack growth in Ti-6Al-2Sn-4Zr-2Mo found in aircraft turbine engine rotor components.

The conclusions are stated as follows:

- The baseline, constant amplitude test confirmed that crack growth behavior was similar for R of 0.33 to 0.5, supporting the negligible impact of crack closure in the experimental program.
- The crack growth rate (da/dN) acceleration following a single overload was consistently larger than the retardation throughout the experiments. As such, the da/dN acceleration was typically more damaging than the retardation was beneficial.
- The crack growth rate for repeated overloads separated by various blocks of R = 0.5 baseline fatigue cycles was reasonably predicted by Miner's Rule – especially at low overload ratios. This confirmed the lack of retarded crack growth rates in this material for the studied overload ratios of 1.25 and 1.50.

- Due to the acceleration in crack growth rate following an overload, minor cycles were more damaging than originally thought. This was especially true at the higher overload ratio and higher K levels.
- The crack growth rates were similar for overload and underload loading conditions demonstrating the applicability to current turbine engine life tracking methods.
- The current method to account for minor cycles in military turbine life tracking, using TACs, may under predict the damage attributed to these cycles for the Ti-6242 material.

Recommendations

There is a multitude of paths that could be pursued in continuing to develop this topic. The following are examples:

- Additional tests with changes in baseline and overload fatigue conditions could be conducted.
  - For example, tests with underloads or running test at field reflective temperatures.
- The significance of the effects of mission overloads in terms of small cracks in Ti-6242 should be investigated.
- Digital imaging correlation could be used to observe plastic zone sizes.
- Microstructural analysis could be performed on damage ahead of the crack tip.
  - Using transmission electron microscope (TEM) to examine material ahead of the crack tip.
- The completion of test at different CBOs.

- For example, one baseline cycle and one overload then repeat, and explore load sequences more representative of actual turbine engines operation.

BIBLIOGRAPHY

[1] R. Sunder, "Unraveling the Science of Variable Amplitude Fatigue," *Journal of ASTM International,* pp. 1-30, 2012.

[2] A. Fatemi and L. Yang, "Cumulative fatigue damage and life prediction theories a survey of the state of the art for homogeneous materials," *International Journal of Fatigue,* pp. 9-34, 1998.

[3] L. Lawson, E. Y. Chen and M. Meshii, "Near-threshold fatigue (a review)," *International Journal of Fatigue,* pp. 15-34, 1999.

[4] C. Gaelle, S.-B. Christine, L. Laurie and H. Zeline, "Near-threshold fatigue propagation of physically short and long cracks in Titanium alloy," *Structural Integrity Procedia,* pp. 950-957, 2016.

[5] R. Ritchie, "Mechanisms of fatigue crack propagation in ductile and brittle solids," *International Journal of Fracture,* pp. 55-83, 1999.

[6] E. Pessard, D. Bellett and F. Morel, "HAL," 22 October 2013. [Online]. Available: https://hal.archives-ouvertes.fr/hal-00875771.

[7] J. M. Larsen and C. G. Annis, Jr., "Observation of Crack Retardation Resulting from Load Sequencing Characteristic of Military Gas Turbine Operation," in *Effect of Load Spectrum Variables on Fatigue Crack Initiation and Propagation, ASTM STP 714*, 1980, pp. 91-107.

[8] J. M. Larsen, A. H. Rosenberger, G. A. Hartman, S. M. Russ and R. John, "The Role of Spectrum Loading in Damage-Tolerance Life-Management of Fracture Critical Turbine Engine Components," *NATO RTO (AVT) Symp. on Monitoring and Management of Gas Turbine Fleets for Extended Life and Reduced Costs,* 2001.

[9] H. Xiaoping, T. Moan and C. Weicheng, "An engineering model of fatigue crack growth under variable amplitude loading," *International Journal of Fatigue,* pp. 2-10, 2008.

[10] S. M. Russ, "Effect of Underloads on Fatigue Crack Growth of Ti-17," Georgia Institute of Technology, 2003.

[11] Sun, Xie, Zhao, Lei and Hong, "A cumulative damage model for fatigue life estimation of high-strength steels in high-cycle and very-high-cycle fatigue regimes," *Fatigue & Fracture of Engineering Materials & Structures,* pp. 638-647, 2011.

[12] R. Sunder, "Spectrum load fatigue--underlying mechanisms and their significance in testing and analysis," *International Journal of Fatigue,* pp. 971-981, 2003.

[13] R. O. Ritchie, "Fatigue behavior of long and short cracks in wrought and powder aluminum alloys," *U.S. Air Force Office of Scientific Research,* pp. 1-210, 1984.

[14] S. Dinda and D. Kujawski, "Correlation and prediction of fatigue crack growth for different R-ratios using Kmax and (delta)K+ parameters," *Engineering Fracture Mechanics,* pp. 1779-1790, 2004.

[15] B. Yuen and F. Taheri, "Proposed modifications to the Wheeler retardation model for multiple overloading fatigue life prediction," *International Journal of Fatigue,* pp. 1803-1819, 2006.

[16] S. Suresh, "Micromechanisms of fatigue crack growth retardation following overloads," *Engineering Fracture Mechanics,* vol. 18, no. 3, pp. 577-593, 1983.

[17] M. Skorupa, "Load interaction effects during fatigue crack growth under variable amplitude loading - a literature review (Part II qualitative interpretation)," *Fatigue Fracture Engineering Material Structures,* pp. 905-926, 1999.

[18] M. Haile, T.-K. Chen, F. Sediles, M. Shiao and D. Le, "Estimating crack growth in rotorcraft structures subjected to mission load spectrum," *International Journal of Fatigue,* pp. 142-149, 2012.

[19] R. Jones, L. Molent and K. Walker, "Fatigue crack growth in a diverse range of materials," *International Journal of Fatigue,* pp. 43-50, 2012.

[20] R. Ambriz and D. Jaramillo, "Mechanical Behavior of Precipitation Hardened Aluminum Alloys Welds," 2014. [Online]. Available: https://cdn.intechopen.com/pdfs-wm/46826.pdf. [Accessed 1 3 2018].

[21] J. Maierhofer, R. Pippan and H. Ganser, "Modified NASGRO equation for physically short cracks," *International Journal of Fatigue,* pp. 200-207, 2014.

[22] M. Ciavarella, P. D'Antuono and G. Demelio, "A simple finding on variable amplitude (Gassner) fatigue SN curves obtained using Miner's rule for unnotched or notched specimen," *Engineering Fracture Mechanics,* pp. 178-185, 2017.

[23] J. Shan, Z. Wei, H. Jingjing and W. Zili, "Comparative study between crack closure model and Willenborg model for fatigue prediction under overload effects," *Chinese Journal of Aeronautics,* pp. 1618-1625, 2016.

[24] A. Chamanfar, T. Pasang, A. Ventura and W. Misiolek, "Mechanical properties and microstructure of laser welded Ti-6Al-2Sn-4Zr-2Mo (Ti6242) titanium alloy," *Materials Science & Engineering A,* pp. 213-224, 2016.

[25] C. Szczepanski, "Ti-6242 Characterization," Dayton, 2012.

[26] International, ASTM, "E647 Standard Test Method for Measurement of Fatigue Crack Growth Rates," *ASTM International,* 2016.

[27] N. Merah, "DC Potential Drop Calibration in Creep-Fatigue Loading Conditions," *Journal of Testing and Evaluation,* pp. 301-306, 2000.

[28] G. Hartman, "WinMATE (University of Dayton Research Institute)," 2002.

[29] ASTM International, "E8/E8M Standard Test Methods for Tension Testing of Metallic Materials," *ASTM International,* 2016.

[30] J. M. Larsen, A. H. Rosenberger and G. A. Hartman, "A mission - Element Approach for Crack Growth under Turbine Engine Spectra," *Proceedings of the Eight International Fatigue Congress,* pp. 1029-1036, 2002.

[31] S. Jiang, W. Zhang and Z. Wang, "1785. A vibration fatigue analysis model considering interaction effects," *International LTD. Journal of Vibroengineering,* pp. 3650-3661, 2015.

[32] H. Pfoertner, "Extension of the Usable Engine Life by Modelling and Monitoring," *MTU Aero Engines GmbH,* 2000.

[33] J. Schon, "Spectrum fatigue loading of composite bolted joints--small cycle elimination," *International Journal of Fatigue,* pp. 73-78, 2006.

[34] Corbly and Packman, "On the Influence of Single and Multiple Peak Overloads on Fatigue Crack Propagation in 7075-T6511 Aluminum," *Engineering Fracture Mechanics,* vol. 5, pp. 479-497, 1973.

[35] O. Herasymchuk, "Microstructurally-dependent model for predicting the kinetics of physically small and long fatigue crack growth," *International Journal of Fatigue,* pp. 148-161, 2015.

[36] R. Jones, "Fatigue crack growth and damage tolerance," *Fatigue and Fracture of Engineering Materials and Structures,* pp. 463-483, 2014.

[37] R. Jones, A. McMillan and R. S. Raman, "Crack growth Does microstructure play a role," *Engineering Fracture Mechanics,* pp. 1-21, 2017.

[38] S. Khan, R. Alderliesten, C. Rans and R. Benedictus, "Application of a modified Wheeler model to predict fatigue crack growth in Fibre Metal Laminates under variable amplitude loading," *Engineering Fracture Mechanics,* pp. 1400-1416, 2010.

[39] R. Murthy, G. Palani and N. Iyer, "An Improved Wheeler Residual Stress Model For Remaining Life Assessment of Cracked Plate Panels," *Tech Science Press,* pp. 289-300, 2004.

[40] M. Liakat and M. Khonsari, "An experimental approach to estimate damage and remaining life of metals under uniaxial fatigue loading," *Materials and Design,* pp. 289-297, 2014.

[41] S. Lee, P. Liaw, H. Choo and R. Rogge, "A study on fatigue crack growth behavior subjected to a single tensile overload Part I. An overload-induced transient crack growth micromechanism," *ScienceDirect,* pp. 485-494, 2011.

[42] J. Baptista, F. Antunes, L. Correia and R. Branco, "A numerical study of the effect of single overloads on plasticity induced crack closure," *Theoretical and Applied Fracture Mechanics,* pp. 51-63, 2017.

[43] S. Benkabouche, H. Guechichi, A. Amrouche and M. Benkhettab, "A modified nonlinear fatigue damage accumulation model under multiaxial variable amplitude loading," *International Journal of Mechanical Sciences,* pp. 180-194, 2015.

[44] G. Harmain, "A model for predicting the retardation effect following a single overload," *Theoretical and Applied Fracture Mechanics,* pp. 80-88, 2010.

[45] L. JianTao, D. PingAn and Z. ZhenYu, "A general model of fatigue crack growth under varable amplitude loading," *Science China,* pp. 673-683, 2012.

[46] I. Aghoury and K. Galal, "A fatigue stress-life damage accumulation model for variable amplitude fatigue loading based on virtual target life," *Engineering Structures,* pp. 621-628, 2013.

[47] S. Kwofie and N. Rahbar, "A fatigue driving stress approach to damage and life prediction under variable amplitude loading," *International Journal of Damage Mechanics,* pp. 393-404, 2012.

[48] P. E. Carrion, N. Shamsaei and R. D. Moser, "Cyclic deformation and fatigue data for Ti-6Al-4V ELI under variable amplitude loading," *Data in Brief,* pp. 180-186, 2017.

[49] S. Pommier, "Cyclic plasticity and variable amplitude fatigue," *International Journal of Fatigue,* pp. 983-997, 2003.

[50] R. Heper and O. Vardar, "Elastic-plastic material response of fatigue crack surfaces profiles due to overload interactions," *International Journal of Fatigue,* pp. 801-810, 2003.

[51] S. Mikheevskiy, G. Glinka and E. Lee, "Fatigue Crack Growth Analysis Under Spectrum Loading in Various Environmental Conditions," *The Minerals, Metals and Materials Society and ASM International,* pp. 1301-1310, 2012.

[52] J.-H. Kim, S.-B. Lee and S.-G. Hong, "Fatigue crack growth behavior of Al7050-T7451 attachment lugs under flight spectrum variation," *Theoretical and Applied Fracture Mechanics,* pp. 135-144, 2003.

[53] Q. Jianke, X. Feng, Y. Ma, J. Lei, Y. Liu, A. Huang, D. Rugg and R. Yang, "Fatigue crack growth behvior of beta-annealed Ti-6Al-2Sn-4Zr-xMo (x = 2, 4 and 6) alloys: Influence of microsturcture and stress ratio," *Jianke Qiu, Xin Feng, Yingjie Ma, Jiafeng Lei, Yuyin Liu, Aijun Huang, David Rugg, Rui Yang,* pp. 150-160, 2016.

[54] M. Hornqvist and T. Mansson, "Fatigue crack growth in Ti-6242 under elasto-plastic loading conditions," *ScienceDirect,* pp. 223-229, 2010.

[55] Borrego, Costa and Ferreira, "Crack propagation of 7050 aluminum alloy under constant amplitude loading and peak overloads," *Procedia Engineering,* pp. 613-620, 2015.

[56] S. K. Paul and Tarafder, "Cyclic plastic deformation response at fatigue crack tips," *International Journal of Pressure Vessels and Piping,* vol. 101, pp. 81-90, 2013.

[57] C. Szczepanski, J. Sushant, Shade, Wheeler and J. Larsen, "Demonstration of an in situ microscale fatigue testing technique on a titanium alloy," *International Journal of Fatigue,* vol. 57, pp. 131-139, 2013.

[58] H.-w. Zhou, H.-q. Liu, D.-q. Yi, Y. Xiao, X.-l. Zhao, J. Wang and Q. Gao, "Effect of alpha phase on fatigue crack growth of Ti-6242 alloy," *Journal of Iron and Steel Research, International,* pp. 811-822, 2017.

[59] V. K. Sahu, A. Kumar, Mohanty, Verma and Ray, "Effect of low-temperature overload on fatigue crack growth retardation and prediction of post overload fatigue life," *Aerospace Science and Technology,* vol. 33, pp. 100-106, 2014.

[60] C. Hernandez and J. Duran, "Evaluation of three current methods for including the mean stress effect in fatigue crack growth rate prediction," *Fatigue and Fracture of Engineering Materials and Structures,* pp. 410-419, 2014.

[61] Newman Jr., Anagnostou and Rusk, "Fatigue and crack-growth analyses on 7075-T651 aluminum alloy coupons under constant and variable amplitude loading," *International Journal of Fatigue,* pp. 133-143, 2014.

[62] Newman Jr., Kota and Lacy, "Fatigue and crack-growth behavior in a titanium alloy under constant-amplitude and spectrum loading," *Engineering Fracture Mechanics,* 2017.

[63] S. Abdullah, S. M. Beden and A. K. Ariffin, "Fatigue Crack Growth Simulation of Aluminium Alloy under Cyclic Sequence Effects," *Aluminium Alloys, Theory and Applications,* pp. 237-258, 2011.

[64] A. Ray and R. Patankar, "Fatigue crack growth under variable amplitude loading (Part I - Model formulation in state-space setting)," *Applied Mathematical Modelling,* pp. 979-994, 2001.

[65] F. Romeiro, M. Freitas and M. Fonte, "Fatigue crack growth with overloads_underloads: Interaction effects and surface roughness," *International Journal of Fatigue,* pp. 1889-1894, 2009.

[66] H.-Z. Huang, J. Gong, M. Zuo, S.-P. Zhu and Q. Liao, "Fatigue Life Estimation of an Aircraft Engine Under Different Load Spectrums," *Int. J. Turbo Jet-Engines,* pp. 259-267, 2012.

[67] J. Ge, Y. Sun and S. Zhou, "Fatigue life estimation under multiaxial random loading by means of the equivalent Lemaitre stress and multiaxial S-N curve methods," *International Journal of Fatigue,* pp. 65-74, 2015.

[68] H. Liu, D.-G. Shang, J.-Z. Liu and Z.-K. Guo, "Fatigue life prediction based on crack closure for 6156 Al-alloy laser welded joints under variable amplitude loading," *International Jounral of Fatigue,* pp. 11-18, 2015.

[69] J. Kim, J. Yi, J. Kim, G. Zi and J. S. Kong, "Fatigue life prediction methodology using entropy index of stress interaction and crack severity index of effective stress," *International Journal of Damage Mechanics,* pp. 375-392, 2012.

[70] F. Chen, F. Wang and W. Cui, "Fatigue life prediction of engineering structures subjected to variable amplitude loading using the improved crack growth rate model," *Fatigue and Fracture of Engineering Materials and Structures,* pp. 278-290, 2011.

[71] F.-J. Zuo, H.-Z. Huang, S.-P. Zhu, Z. Lv and H. Gao, "Fatigue life prediction under variable amplitude loading using a non-linear damage accumulation model," *International Journal of Damage Mechanics,* pp. 1-18, 2014.

[72] S. Jha, R. John and J. Larsen, "Incorporating small fatigue crack growth in probabilistic life prediction (Effect of stress ratio in Ti-6Al-2Sn-4Zr-6Mo)," *International Journal of Fatigue,* pp. 83-95, 2013.

[73] M. Sander, T. Muller and J. Lebahn, "Influence of mean stress and variable amplitude on the fatigue behaviour of a high-strength steel in VHCF regime," *International Journal of Fatigue,* pp. 10-20, 2014.

[74] K. Zakaria, S. Abdullah, M. Ghazali and C. Azhari, "Influence of spectrum loading sequences on fatigue life in a high-temperature environment," *Engineering Failure Analysis,* pp. 111-123, 2013.

[75] Z. Tao, D. Shang, H. Liu and H. Chen, "Life prediction based on weight-averaged maximum shear strain range plane under multiaxial variable amplitude loading," *Fatigue and Fracture of Engineering Materials and Structures,* pp. 907-920, 2015.

[76] C. Ward-Close, A. Blom and R. Ritchies, "Mechanisms associated with transient fatigue crack growth under variable amplitude loading An experimental and numerical study," *Engineering Fracture Mechanics,* pp. 613-638, 1989.

[77] R. Sunder, N. E. Ashbaugh, W. J. Porter and A. H. Rosenberger, "Multi-Mechanism Synergy in Variable-Amplitude Fatigue," *Journal of ASTM International,* pp. 1-21, 2004.

[78] N. Saintier, T. Palin-luc, J. Benabes and F. Cocheteux, "Non-local energy based fatigue life calculation method under multiaxial variable amplitude loadings," *International Journal of Fatigue,* pp. 68-83, 2013.

[79] M. V. Pereira, F. Darwish, A. Camarao and S. Motta, "On the prediction of fatigue crack retardation using Wheeler and Willenborg models," June 2007. [Online]. Available: http://dx.doi.org/10.1590/S1516-14392007000200002.

[80] W. Ochensberger and O. Kolednik, "Overload effect revisited - Investigation by use of configurational forces," *International Journal of Fatigue,* pp. 161-173, 2016.

[81] L. Borrego, J. D. Costa and A. M. Ferreira, "Plasticity induced closure under variable amplitude loading in AlMgSi aluminum alloys," *Structural Integrity Procedia,* pp. 85-92, 2017.

[82] A. H. Noroozi, G. Glinka and S. Lambert, "Prediction of fatigue crack growth under constant amplitude loading and a single overload based on elasto-plastic crack tip stresses and strains," *Engineering Fracture Mechanics,* pp. 188-206, 2008.

[83] G. Dhondt, "Prediction of three-dimensional crack propagation paths taking high cycle fatigue into account," *Focussed on Crack Paths,* pp. 108-113, 2016.

[84] A. Alessandra and D. Straub, "Reliability assessment of high cycle fatigue under variable amplitude loading Review and solutions," *Engineering Fracture Mechanics,* pp. 40-66, 2014.

[85] M. J. Caton, R. John, W. J. Porter and M. E. Burba, "Stress ratio effects on small fatigue crack growth in Ti-6Al-4V," *International Journal of Fatigue,* pp. 36-45, 2012.

[86] R. Filip, K. Kubiak, W. Ziaja and J. Sieniawski, "The effect of microstructure on the mechanical properties of two-phase titanium alloys," *Journal of Materials Processing Technology,* pp. 84-89, 2003.

[87] ASMinternational, "Titanium and its Alloys," January 2008. [Online]. Available: asminternational.org. [Accessed January 2018].

[88] M. Sander, T. Muller and C. Stacker, "Very high cycle fatigue behavior under constant and variable amplitude loading," *Structural Integrity Procedia,* pp. 34-41, 2016.

[89] S. Stanzl-Tschegg, "Very high cycle fatigue measuring techniques," *International Journal of Fatigue,* pp. 2-17, 2014.

[90] ASTM International, "E399 Standard Test Method for Linear-Elastic Plane-Strain Fracture Toughness Klc of Metallic Materials," *ASTM International,* 2013.

[91] O. EZIK, "Calculation of the actual cost of engine maintenance," *Air Force Institute of Technology,* 2003.

APPENDIX A

Single Overload [da/dN, a vs N]

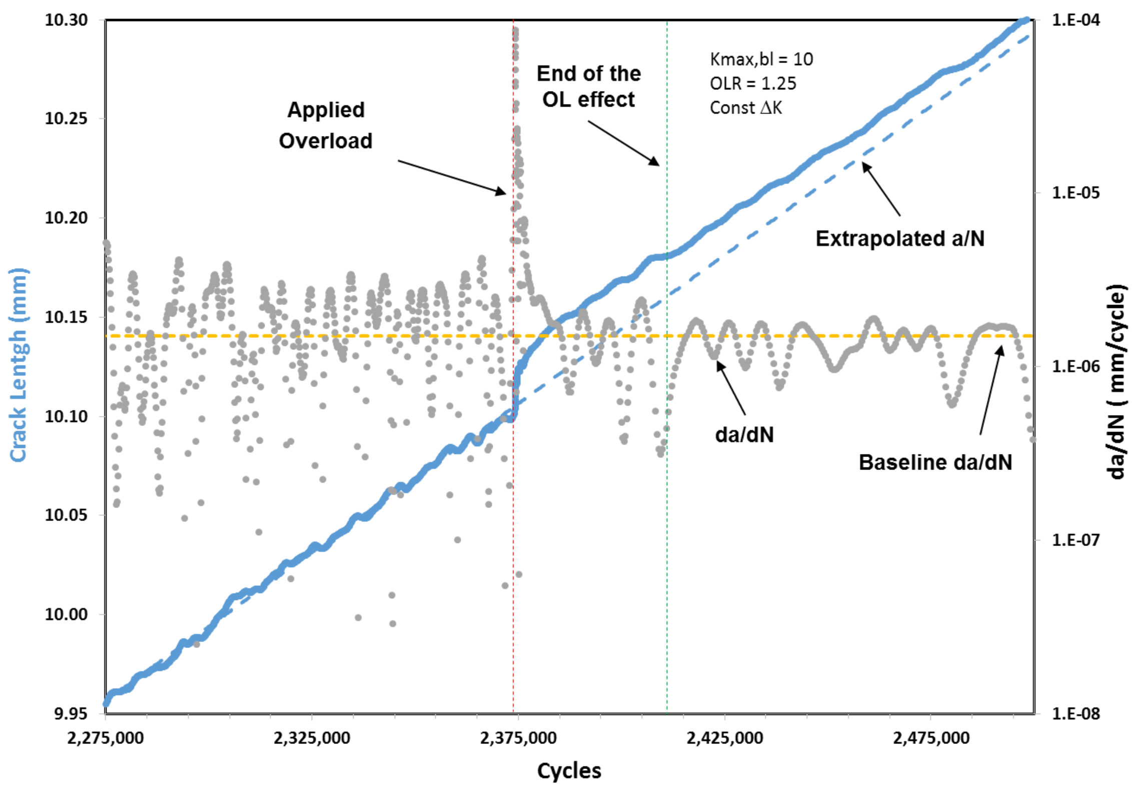

Figure 42: SOL K_{max} 10 OLR 1.25 Constant ΔK

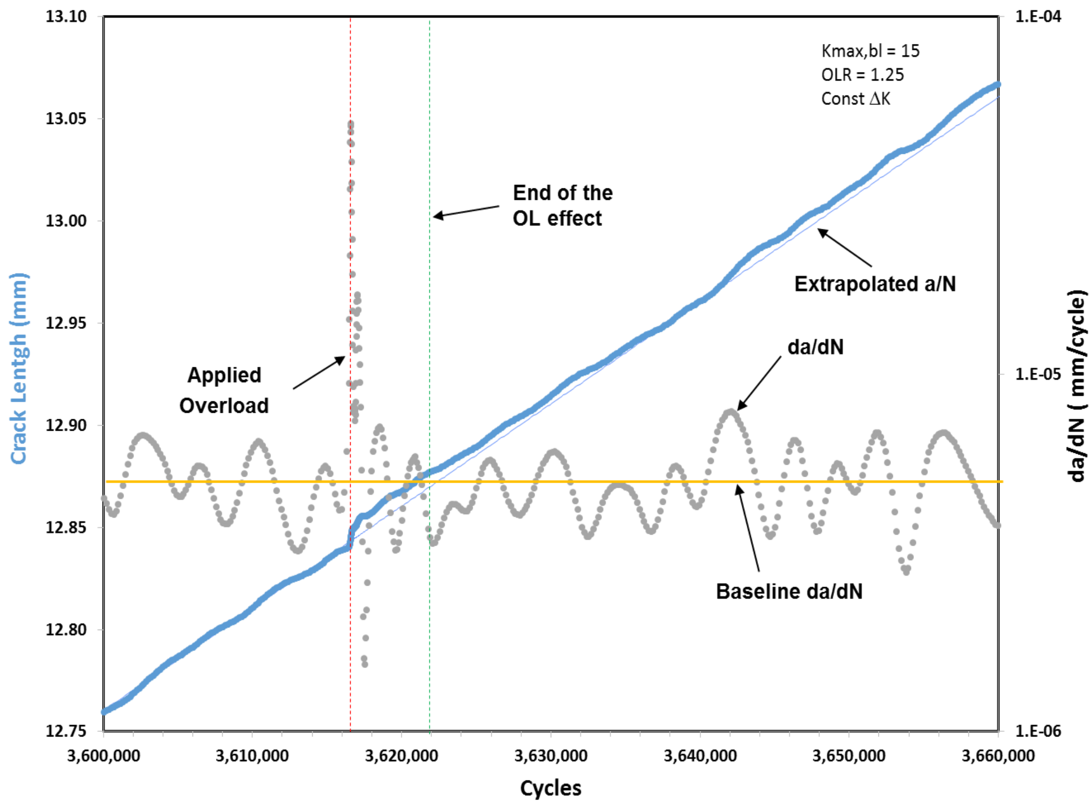

Figure 43: SOL K_{max} 15 OLR 1.25 Constant ΔK

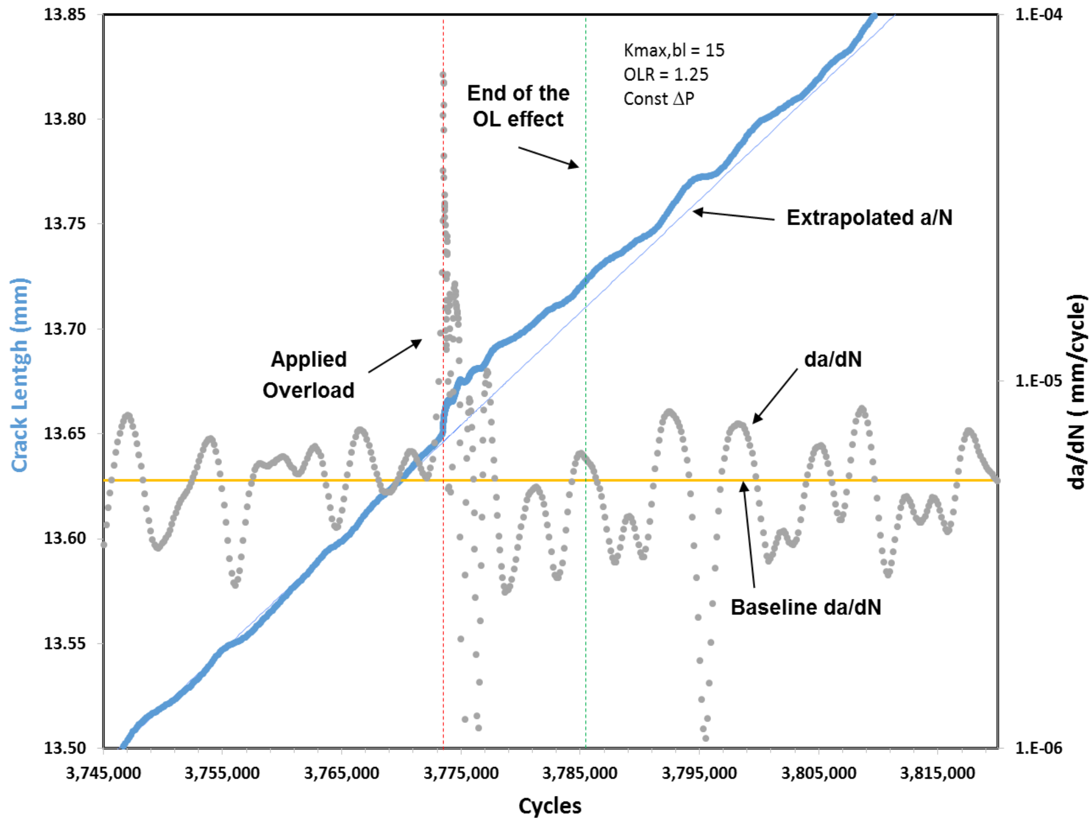

Figure 44: SOL K_{max} 15 OLR 1.25 Constant ΔP

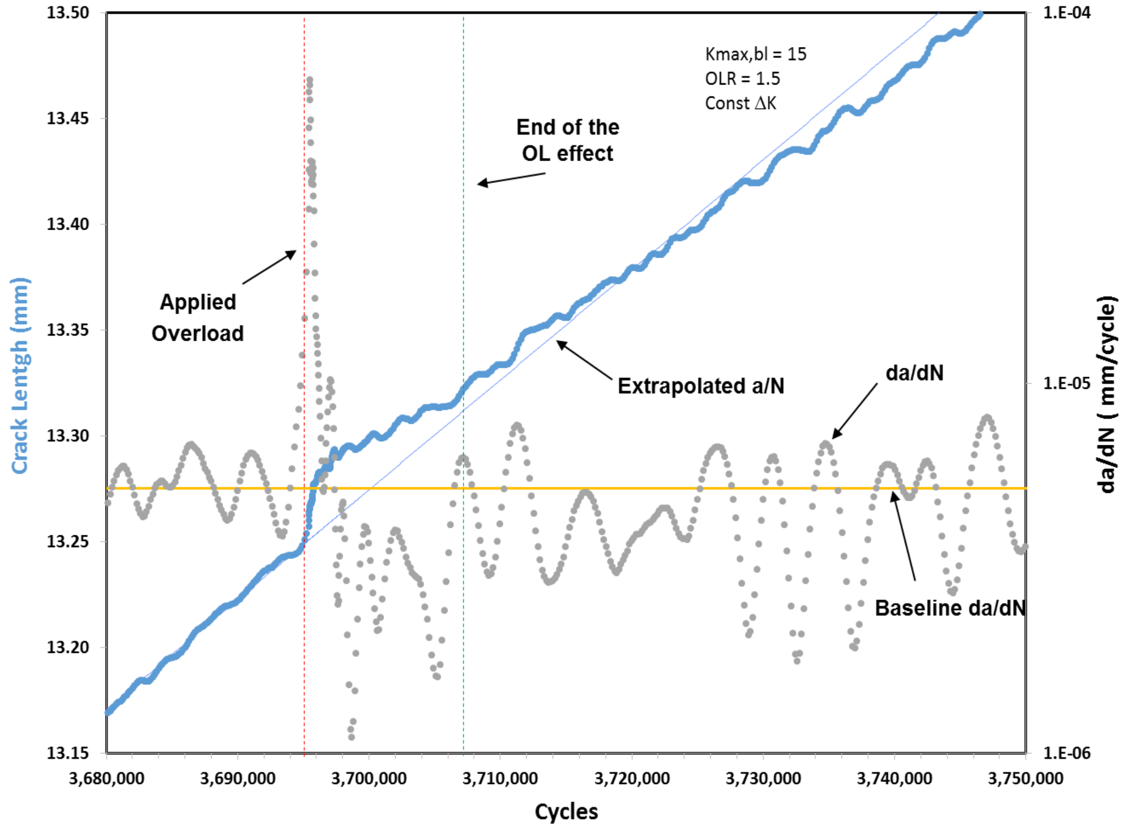

Figure 45: SOL K_{max} 15 OLR 1.50 Constant ΔK

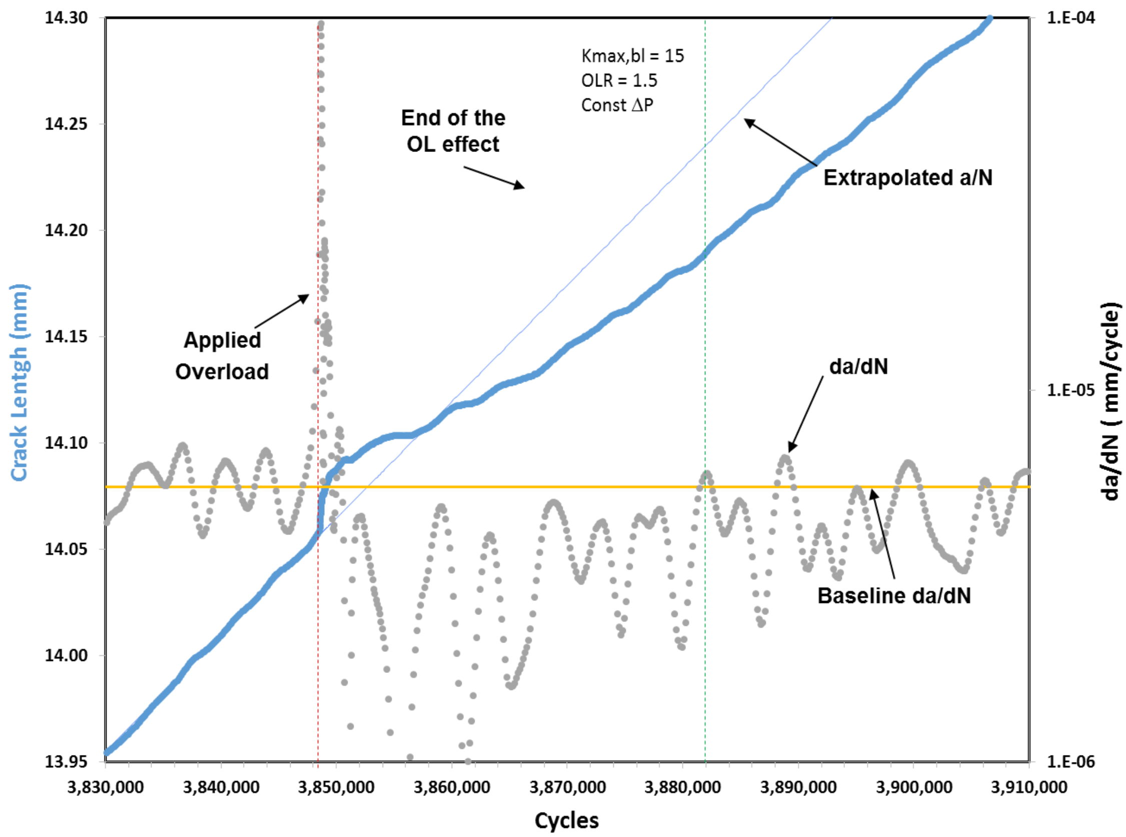

Figure 46: SOL K_{max} 15 OLR 1.50 Constant ΔP

APPENDIX B

<u>Paris Power Law Data Fits</u>

This section contains all of the Paris Power Law fitted data at 5, 10, 20, 40, and 80 CBO for both OLR = 1.25 and 1.50.

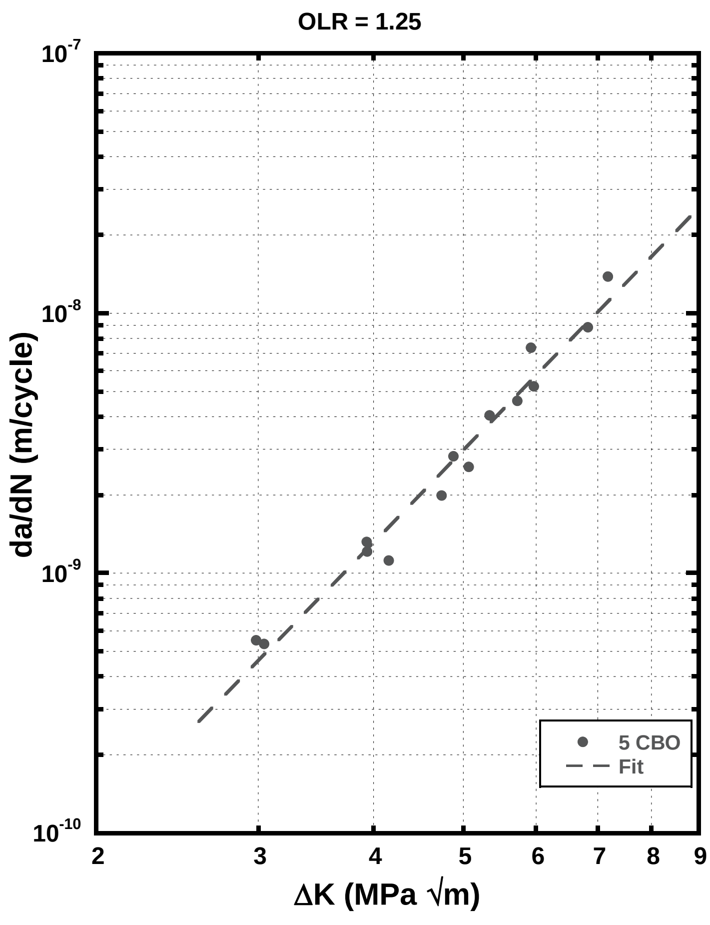

Figure 47: Paris Power Law Fit 5 CBO OLR = 1.25 [da/dN vs ΔK]

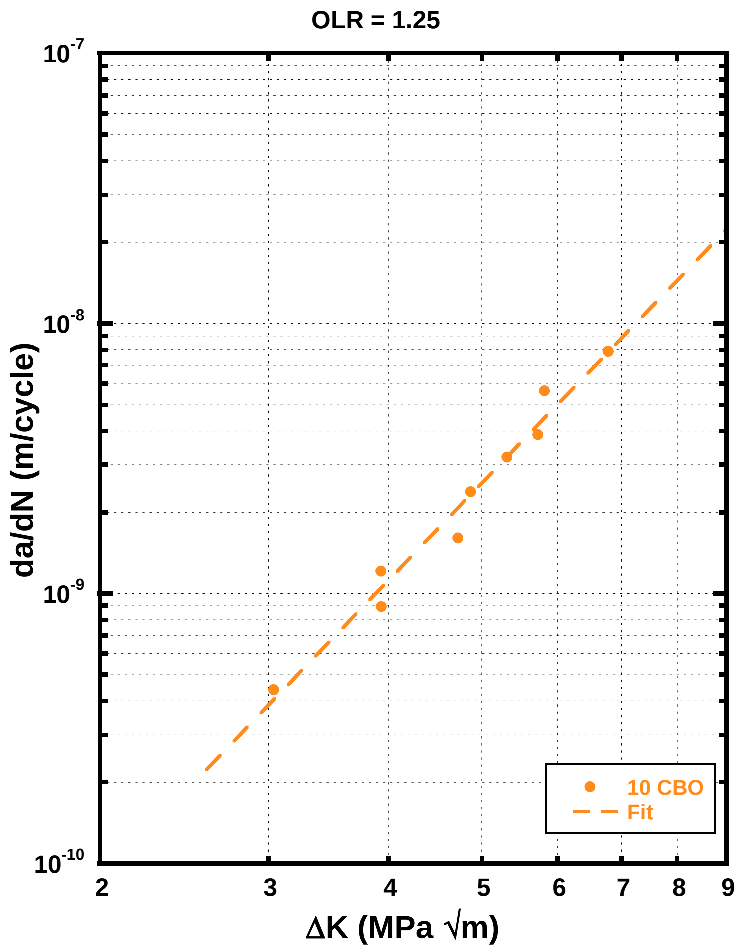

Figure 48: Paris Power Law Fit 10 CBO OLR = 1.25 [da/dN vs ΔK]

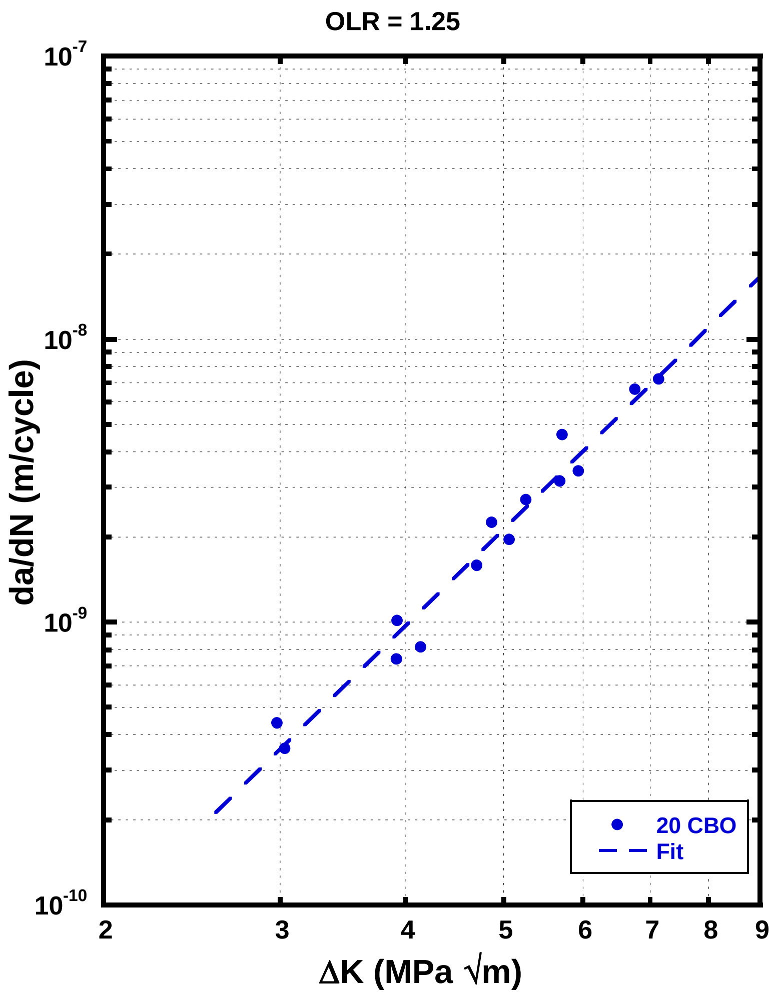

Figure 49: Paris Power Law Fit 20 CBO OLR = 1.25 [da/dN vs ΔK]

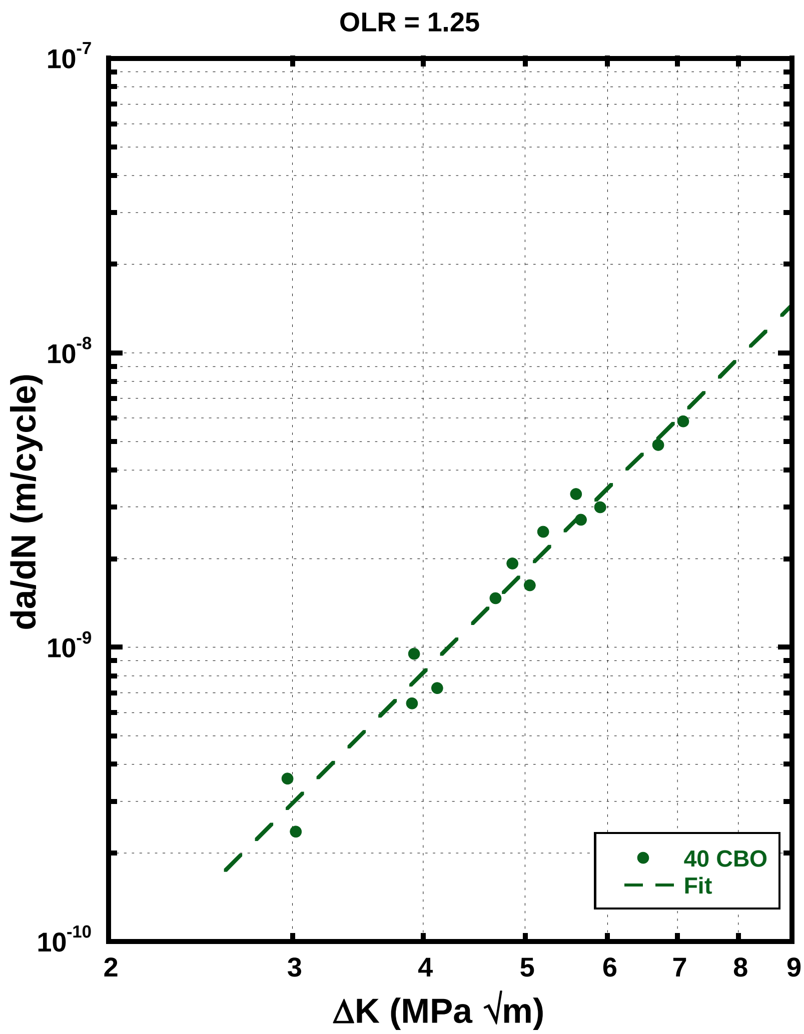

Figure 50: Paris Power Law Fit 40 CBO OLR = 1.25 [da/dN vs ΔK]

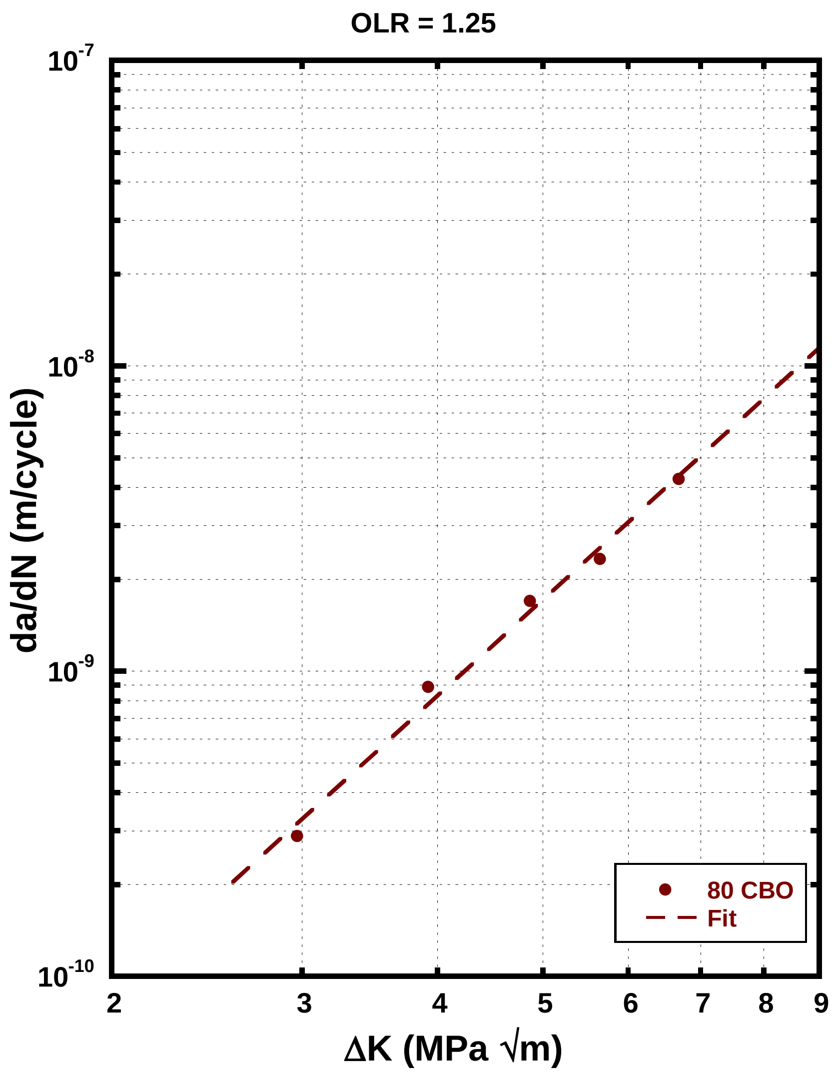

Figure 51: Paris Power Law Fit 80 CBO OLR = 1.25 [da/dN vs ΔK]

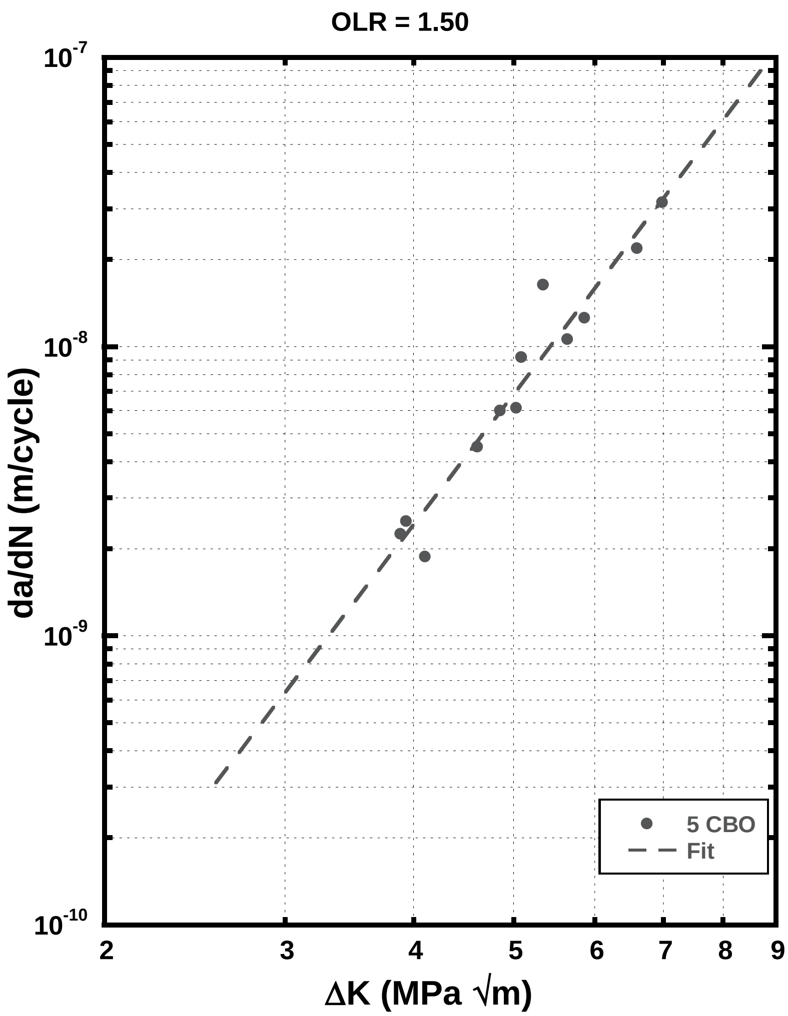

Figure 52: Paris Power Law Fit 5 CBO OLR = 1.50 [da/dN vs ΔK]

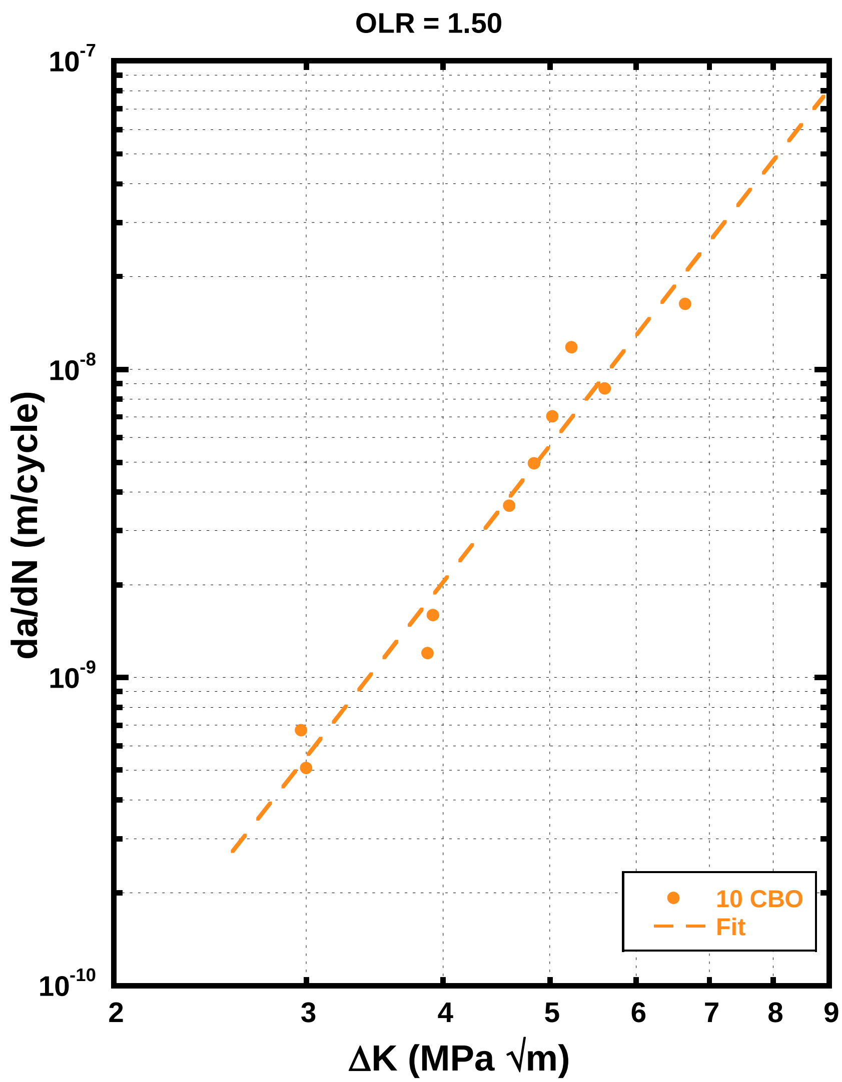

Figure 53: Paris Power Law Fit 10 CBO OLR = 1.50 [da/dN vs ΔK]

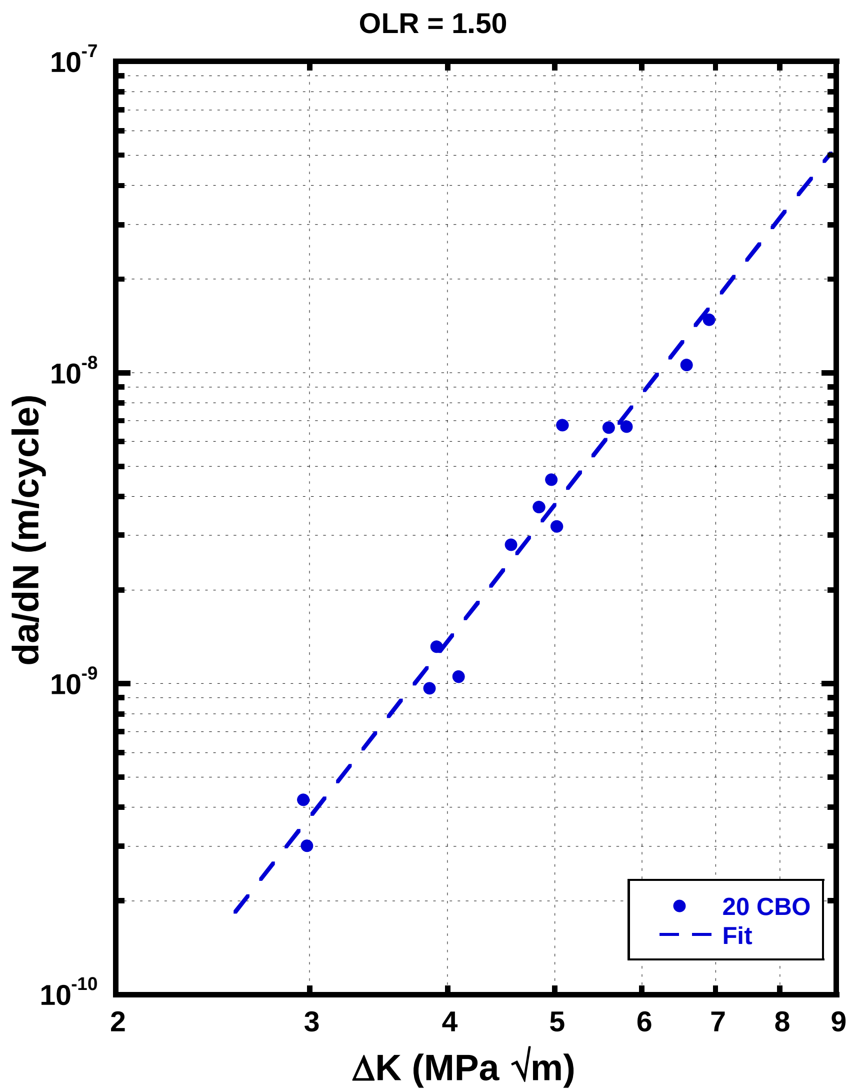

Figure 54: Paris Power Law Fit 20 CBO OLR = 1.50 [da/dN vs ΔK]

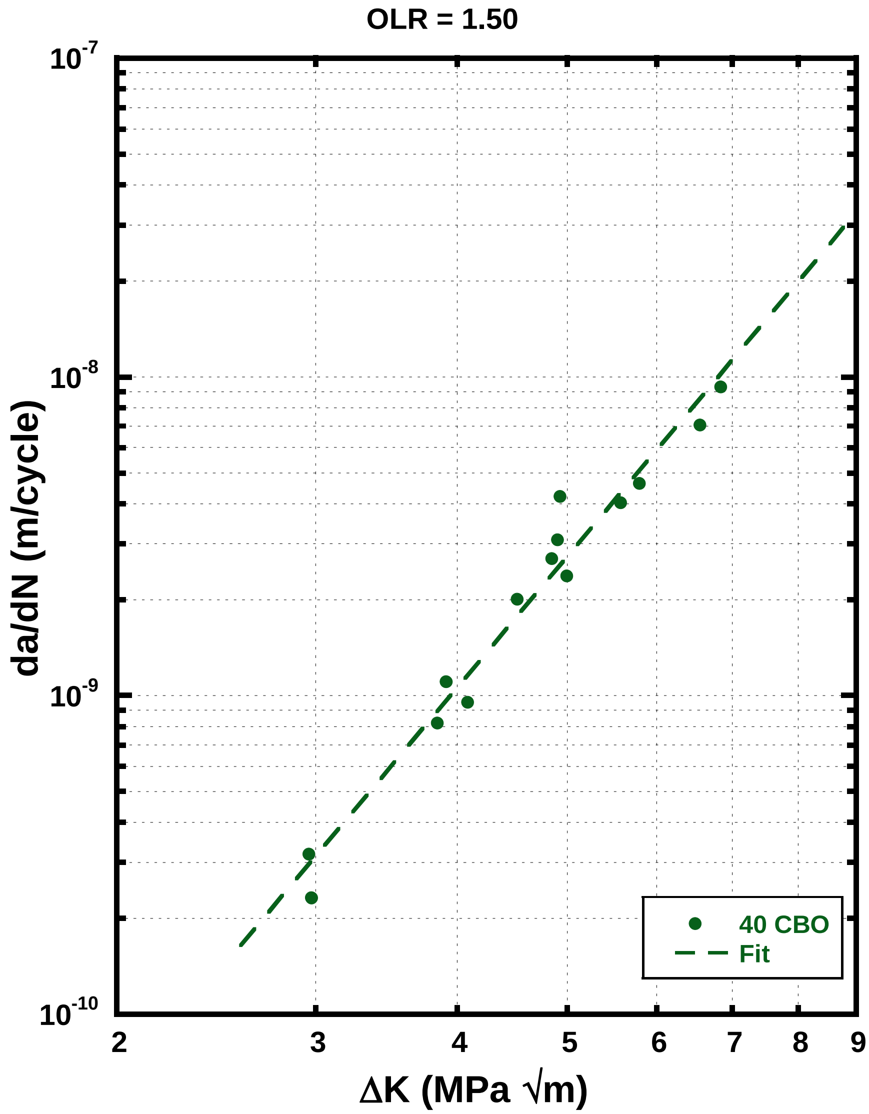

Figure 55: Paris Power Law Fit 40 CBO OLR = 1.50 [da/dN vs ΔK]

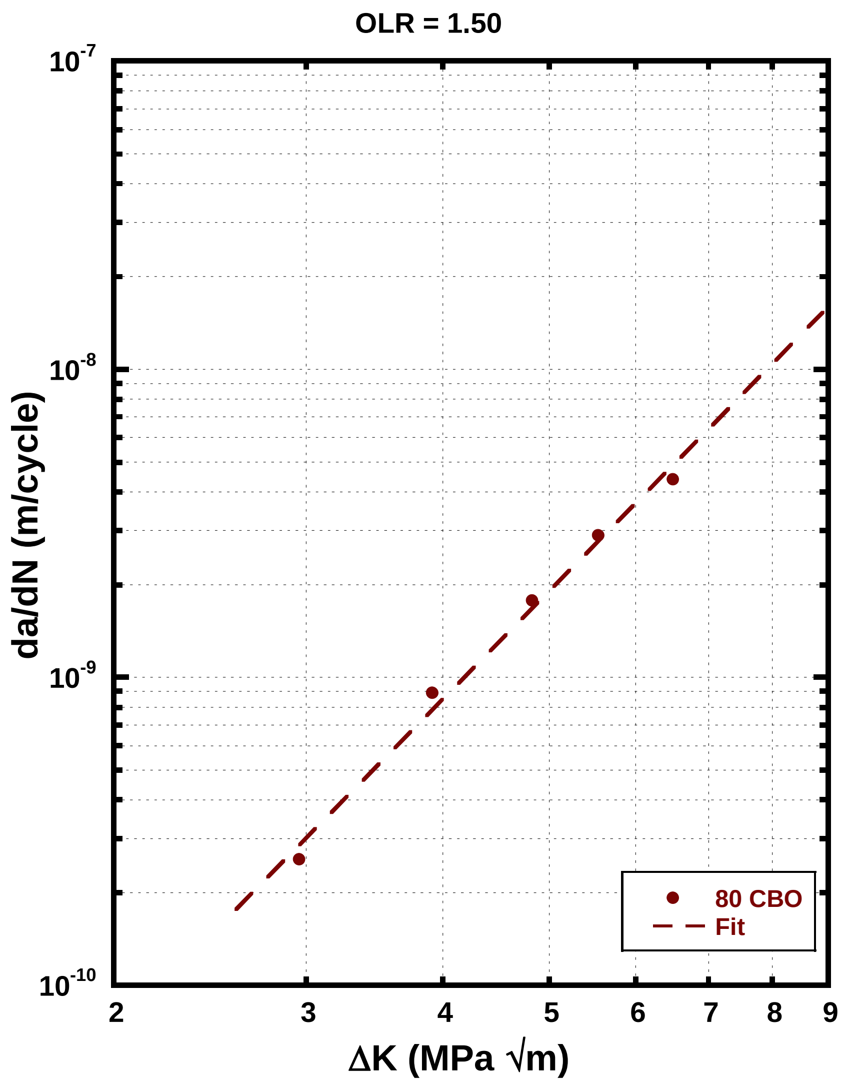

Figure 56: Paris Power Law Fit 80 CBO OLR = 1.50 [da/dN vs ΔK]

B.1 Measured/Miner's Predicted FCGR

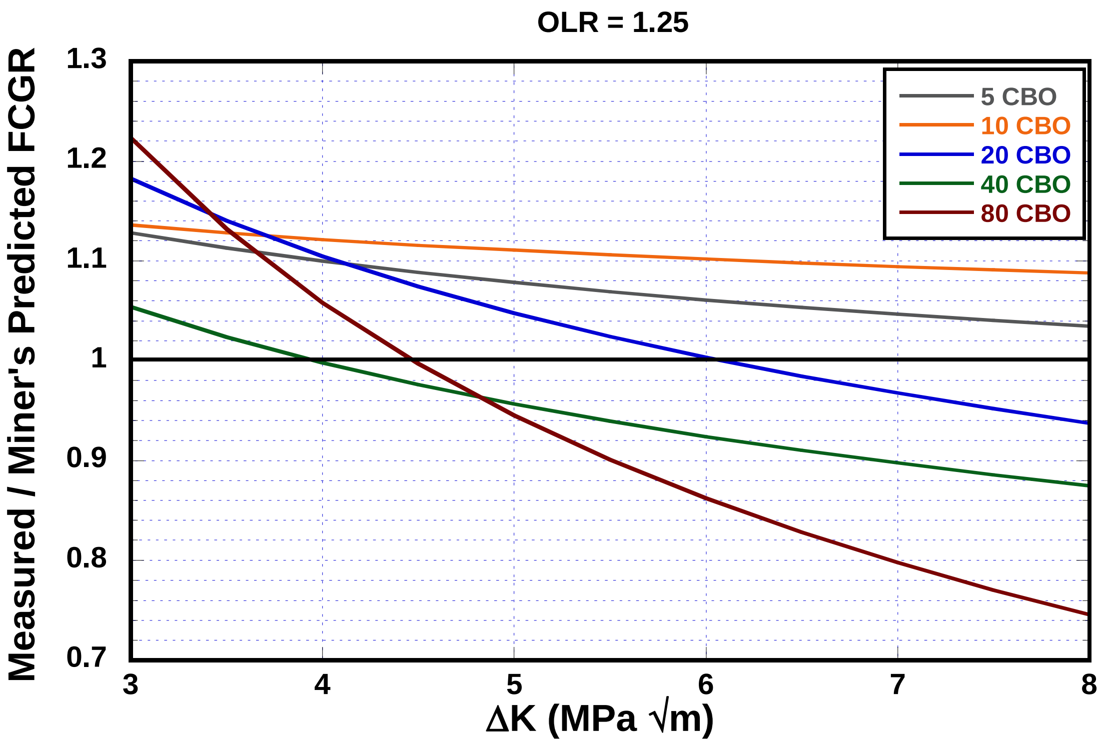

Figure 57: Measured/Miner's Predicted FCGR [OLR = 1.25]

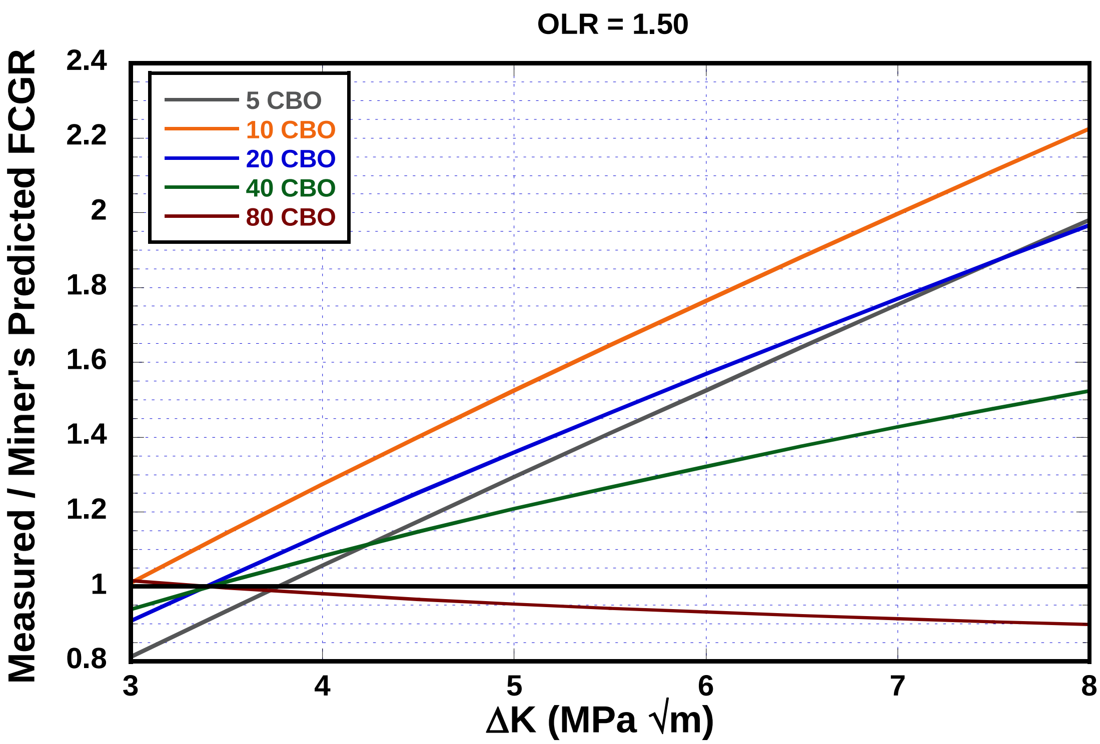

Figure 58: Measured/Miner's Predicted FCGR [OLR = 1.50]

B.2 Comparison of OL and BL Normalized Local Crack Growth Rate

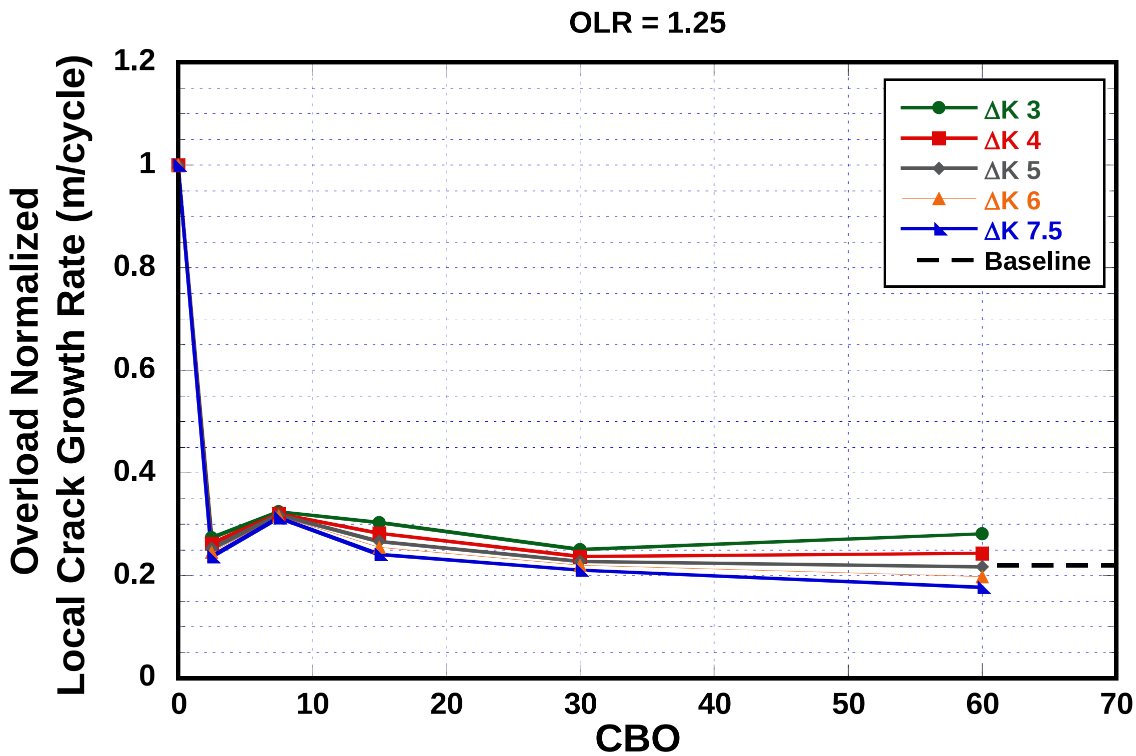

Figure 59: Overload Normalized Local Crack Growth Rate OLR = 1.25 [da/dN vs CBO]

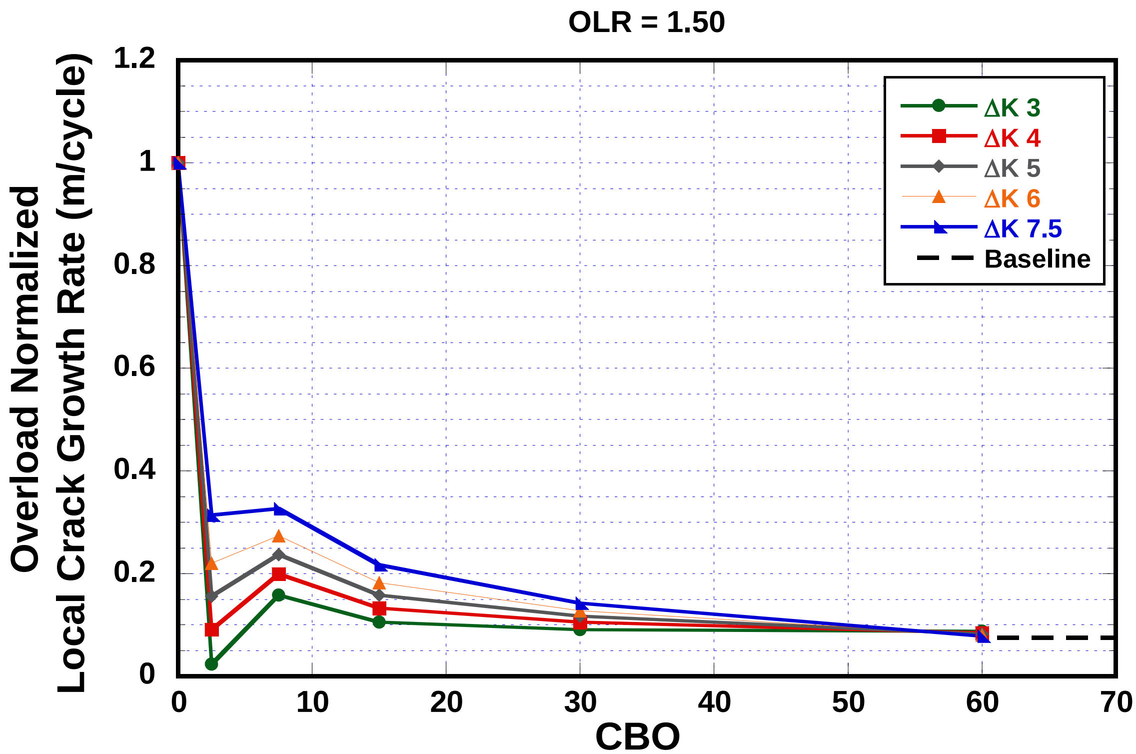

Figure 60: Overload Normalized Local Crack Growth Rate OLR = 1.50 [da/dN vs CBO]

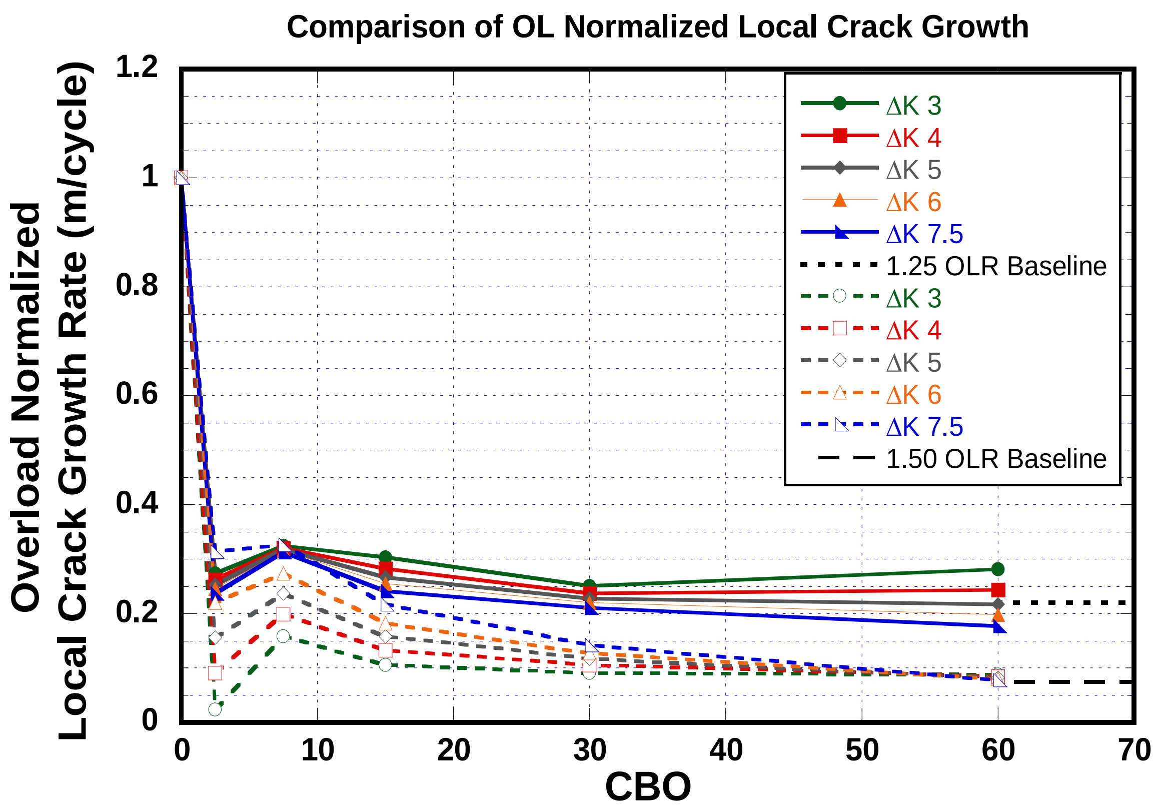

Figure 61: Comparison of OL Normalized Local Crack Growth Rate

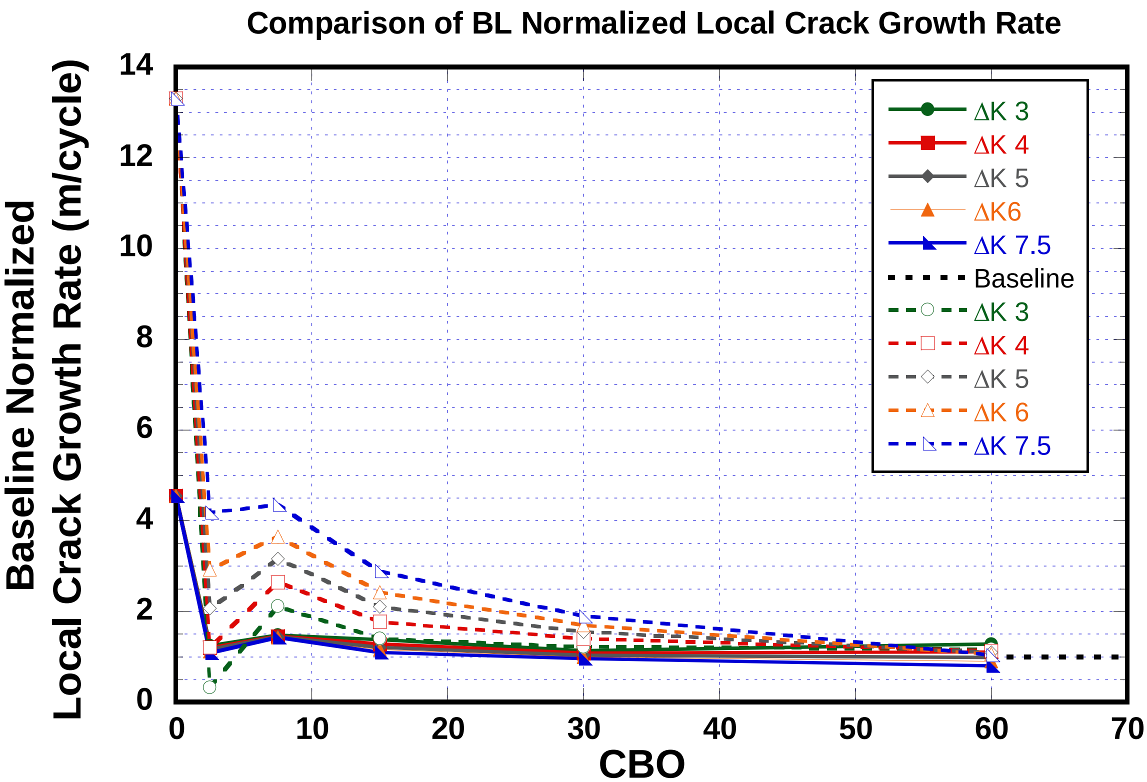

Figure 62: Comparison of BL Normalized Local Crack Growth Rate

B.3 Actual/Predicted (A/P) Probability

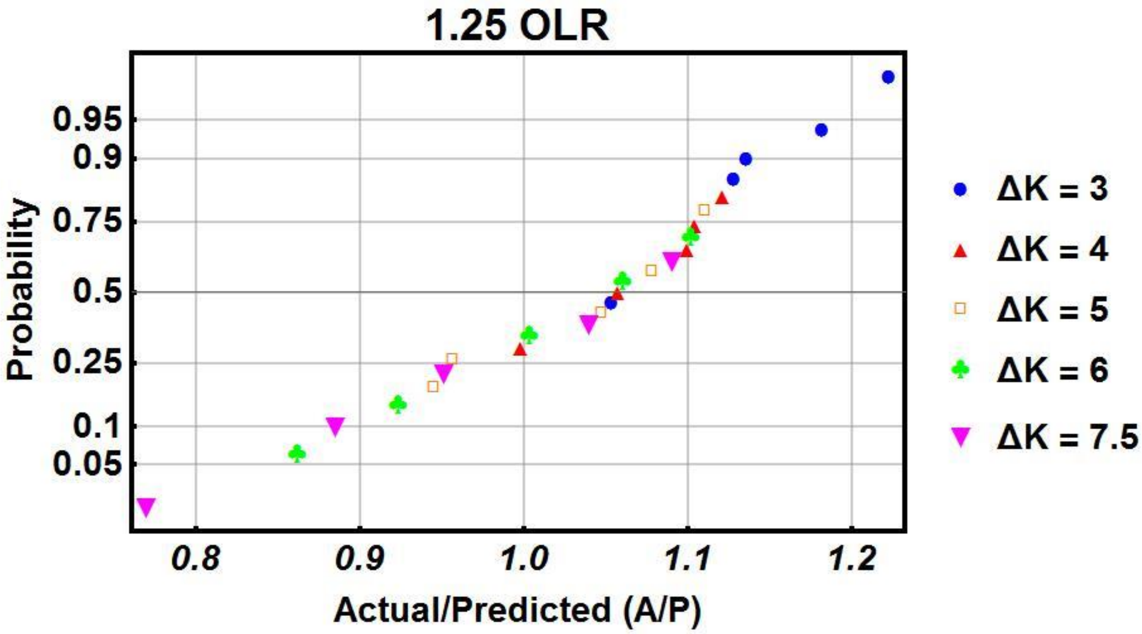

Figure 63: Actual/Predicted vs Probability OLR = 1.25 [ΔK]

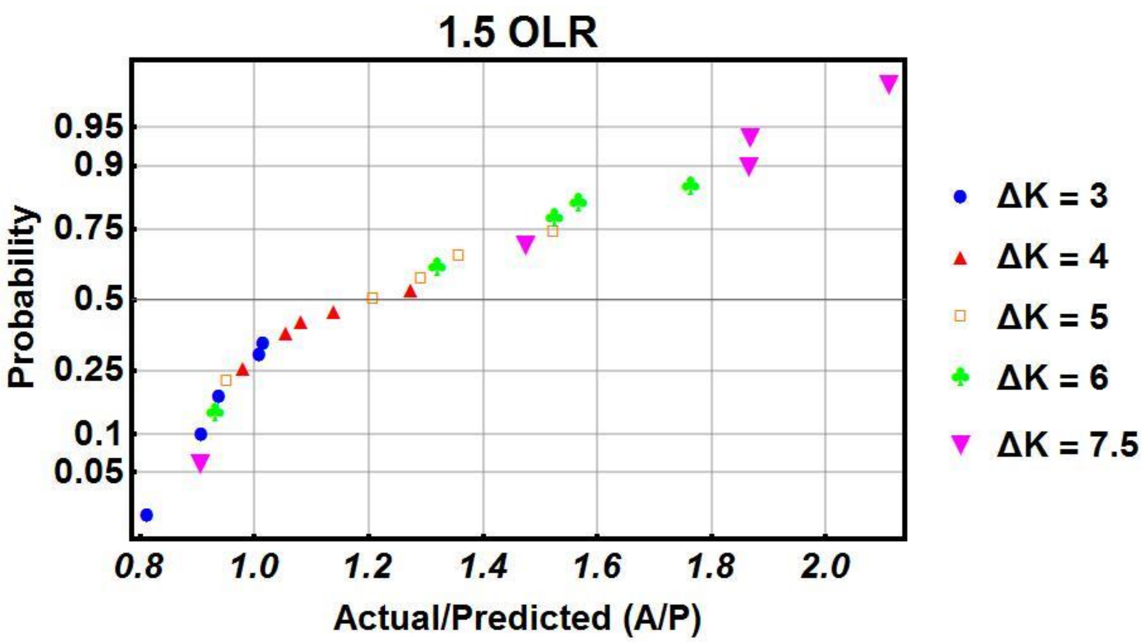

Figure 64: Actual/Predicted vs Probability OLR = 1.50 [ΔK]

B.4 Measured/Miner's Prediction FCGR

The figure below places the ratios at OLR 1.25 of measured Paris power law divided by Miner's rule predicted across CBO. Throughout this figure, there is constant separation ΔK with no overlap taking place. All ΔK's except 7.5 are at or above one by 20 CBO. Once passed that, ΔK of 5, 6, and 7.5 continue below one.

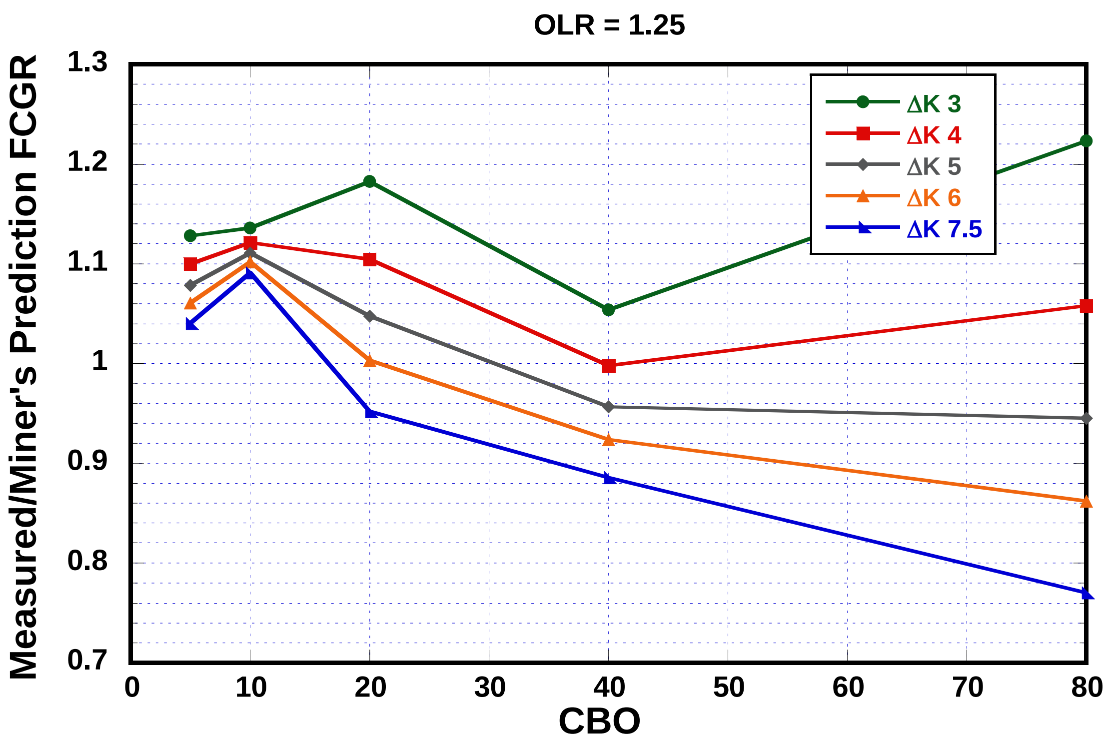

Figure 65: Measured/Miner's Prediction FCGR vs CBO [OLR = 1.25]

The figure below illustrates the ratios at OLR 1.25 of measured Paris power law divided by Miner's rule predicted across CBO. There is clear separation in ΔK up until around 70 CBO. The dramatic change that occurs here could be connected to the number of points taken in figure "OLR = 1.5 80 CBO."

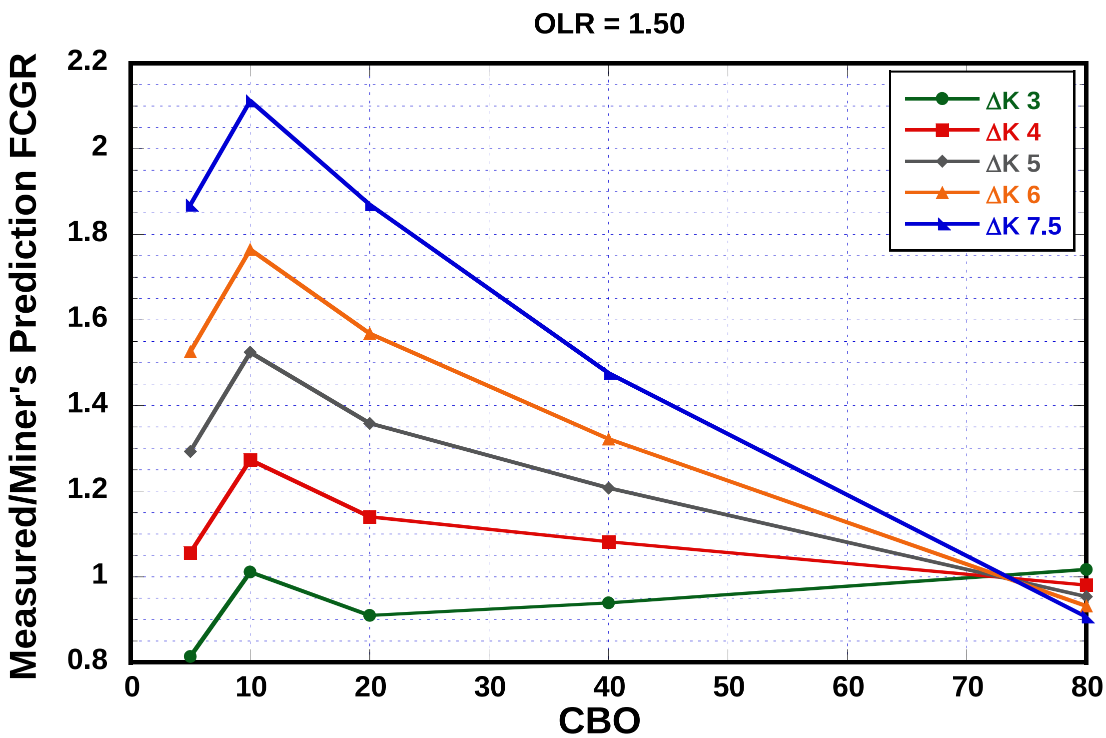

Figure 66: Measured/Miner's Prediction FCGR vs CBO [OLR = 1.50]

The figure below portrays the ratios at OLR 1.25 and 1.5 of measured Paris power law divided by Miner's rule predicted across CBO. For the majority of this figure the OLR 1.25 and 1.5 ΔK's are completely opposite.

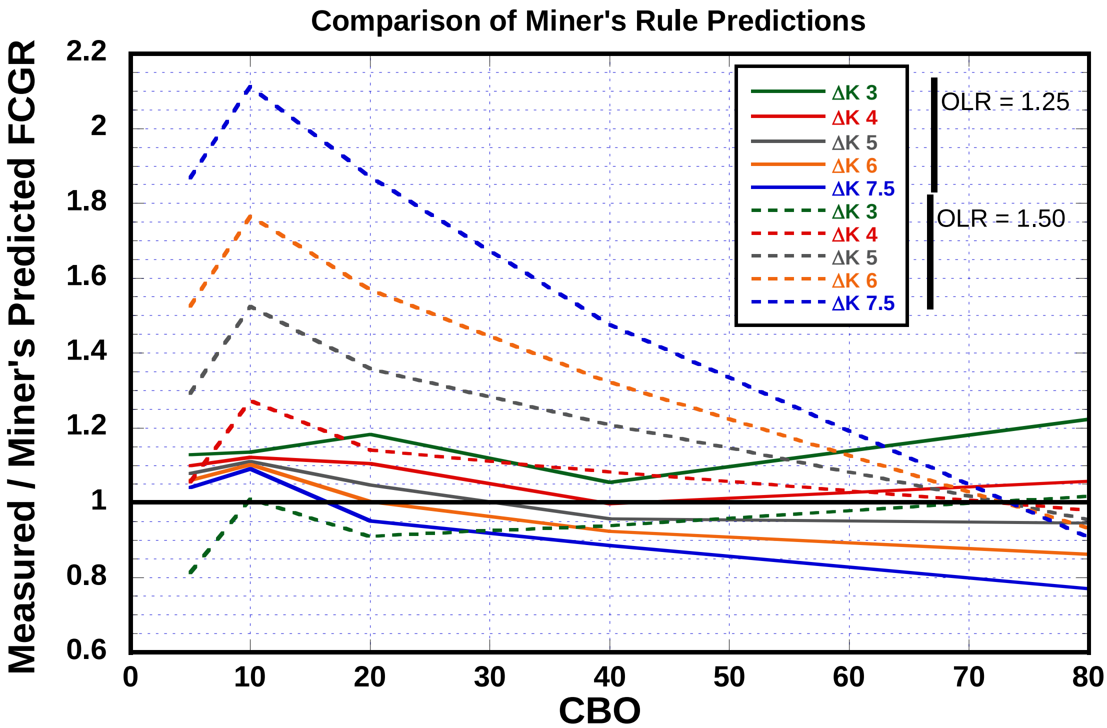

Figure 67: Comparison of Miner's Rule Predictions